Winter 2013

Analysis and Simulation of Kinetic Model for Active Suspensions

Panon Phuworawong
Old Dominion University

ANALYSIS AND SIMULATION OF KINETIC MODEL FOR ACTIVE SUSPENSIONS

by

Panon Phuworawong
B.S. February 2006, Kasetsart University, Thailand
M.S. May 2008, Thammasat University, Thailand

A Dissertation Submitted to the Faculty of
Old Dominion University in Partial Fulfillment of the
Requirements for the Degree of

DOCTOR OF PHILOSOPHY

COMPUTATIONAL AND APPLIED MATHEMATICS

OLD DOMINION UNIVERSITY
December 2013

Approved by:

Ruhai Zhou (Director)

Hideaki Kaneko (Member)

Sookyung Joo (Member)

Fang Q. Hu (Member)

Bala Ramjee (Member)

ABSTRACT

ANALYSIS AND SIMULATION OF KINETIC MODEL FOR ACTIVE SUSPENSIONS

Panon Phuworawong
Old Dominion University, 2013
Director: Dr. Ruhai Zhou

In this research, we study the recently proposed kinetic model for active suspensions, where the active particles are assumed to be rigid rod and are driven in the suspension either by their own biological/chemical forces or external electric/magnetic fields. We first study the stability of the isotropic suspension in quiescent flow. Then we investigate the weak shear perturbation of the isotropic state and study some rheological properties of the suspension by explicit analytic formulas derived directly from the model. For imposed shear, we give some bifurcation diagrams of the stable states in some parametric spaces through numerical simulations. Some rheological properties are also examined. Finally, we study the spatio-temperal structures of suspensions by taking into account the long-range particle interactions with periodic boundary conditions. A Galerkin approach is used to develop numerical method for the kinetic model equations, which projects the number density function onto the subspace of Fourier modes. Extensive numerical simulations are performed in various physical domains with different parameter values. Several complex physical phenomena are observed and carefully studied.

ACKNOWLEDGMENTS

I would like to first express my gratitude and appreciation to my advisor, Dr. Ruhai Zhou, for his consistent support and great advice. He always give me positive reinforcement from the beginning of my study during coursework all the way to this research. His invaluable contributions and suggestions allow me to accomplish my goal at Old Dominion University.

I would like to thank my dissertation committee, Dr. Hideaki Kaneko, Dr. Sookyung Joo, Dr. Fang Q. Hu, and Dr. Bala Ramjee for their precious time, valuable guidance, and willingness to be part of this research endeavor.

I am greatly indebted to my parents, Nakin and Suwannarat Phuworawong, who have been giving me advice and love that carry me to succeed in my study, career, and my future.

I greatly appreciate the supports from my friends who have given encouragements and helped me to get through some difficult times. My appreciations also go to the secretaries of the department for helping me with all paperwork during my time as a graduate student.

I am also grateful for the support of my research by NSF grant DMS-0908409 and funding from both Mathematics and Modeling & Simulation Department at Old Dominion University.

TABLE OF CONTENTS

LIST OF TABLES

LIST OF FIGURES

CHAPTER 1

INTRODUCTION

In the last decade, suspensions of active (self-propelled) particles have attracted much attention and interest due to their relevance in many scientific areas such as pathology [**24**], ecology [**5, 34**], as well as technological and medical application [**25, 26, 36**]. Examples of active suspension include swimming microorganisms, such as bacteria and microalgae, and synthetic nanoparticles that can driven themselves via chemical reactions or external imposed magnetic fields. These swimming mechanisms have the common feature that each self-propelling particle exerts a propulsive force on the surrounding fluid resulting in disturbance flows in the fluid, hydrodynamic interactions, and modifications of the effective rheology of their suspensions.

The are two types of active particle. The particle that swim using its head is called "puller" whereas the particle that swim using its tail is called "pusher". Generally, researchers consider the active particles as self-propelled rods. The swimming direction of each particle is assumed to be aligned with its axis of symmetry. Figure 1 shows the picture of active particle moving in direction $\mathbf{p}$.

Because of their geometry, we can break down the order of the particles into three categories (see Figure 2). First, the isotropic state where all particle are randomly oriented. Second, the polar state where all particles are on average aligned in the same swimming direction. Third, the nematic state where particles are paralleled but with random swimming directions.

Many particle-based models and simulations have been proposed to explain and predict the dynamics of such systems [**16, 19, 32, 39**]. These researches amazingly yield results in qualitative agreement with experimental data. However, because of their expensive computational cost, their simulations become size limited and are difficult to study systematically. To overcome such difficulties, people have found it useful to study active suspension as a complex system then use statistical physics tools such as kinetic and hydrodynamic equations to derive continuum or mesocropic models. Notable works include Giomi et al. [**11, 12, 13**] where they derive macroscopic model for particle concentration and polar/nematic orientational parameter, and Shelley et al. [**17, 30, 31**] where they propose a microscopic model for active

FIGURE 1: A self-propelled rod moving in direction **p**.

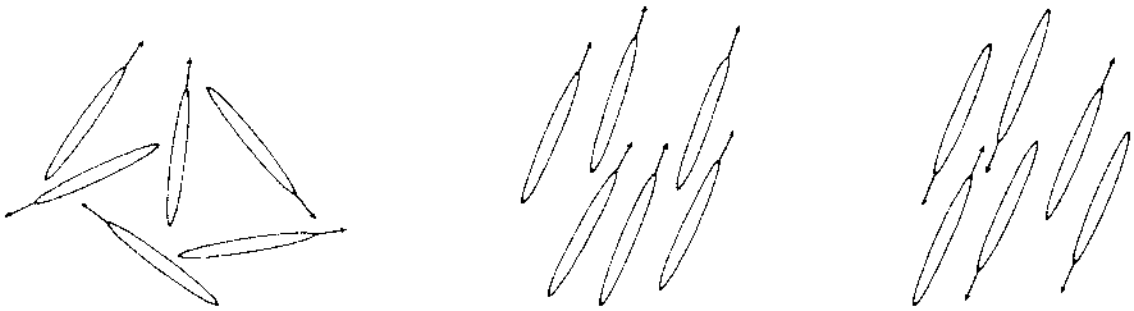

(a) Isotropic state (b) Polar state (c) Nematic state

FIGURE 2: Three ordered phases of rod-like particles.

suspensions and then project the microscopic information onto macroscopic variables to get the concentration, and polar/nematic orientation. These models, however, are valid in the regime of weak particle interactions. For the in-depth discussion of various models, we refer the reader to recent reviews of Marchetti et al. [**22**] and Saintillan et al. [**29**].

This research presents a systematic study of the suspensions of rigid rod-like particles in two-dimensional case in a dilute regime by focusing on the recently proposed kinetic model by M.G. Forest, Q. Wang, R. Zhou [**7**]. The model is an extension of the kinetic model for passive nematic polymers [**4, 8, 43**] and takes into account of what have been neglected from other models such as intermolecular potential and new extra stress contributions to the disturbance flow equation. We begin our discussion in Chapter 2 with the kinetic model of active particles. Using this model in Section 3.1, we discuss the linear stability of isotropic suspensions in the absence of fluid flow. We show in Section 3.2 that the explicit formula for the alignment of particles and rheological properties of suspensions can be derived directly from the kinetic

model in the case of shear perturbed isotropic suspension. In section 3.3, we remove the restriction of the weak shear and continue investigating the bifurcation structure of the model, behavior of the particle, and the effect of swimming mechanism to the rheological properties of suspensions. In Chapter 4, we develop numerical method in 2D physical space and 1D orientational space then study the long-time evolution of instability and pattern formation of inhomogeneous suspensions in both square and rectangle domains. Several simulation results are carefully studied to show the complex spatio-temporal structures of active suspensions.

CHAPTER 2

KINETIC MODEL FOR ACTIVE SUSPENSIONS

In this research, we will utilize the kinetic model proposed recently for dilute and semidilute active suspensions where the concentration is low [7]. Each particle is assumed to be rigid and rod-shaped (see Figure 3) described by its length L, width d, center-of-mass position $\mathbf{x}$ and axis of symmetry $\mathbf{m}$. Here, the force generated by the swimming mechanism of active particle is assumed to be along the direction of $\mathbf{m}$. The kinetic model consists of the Smoluchowski equation,

$$\frac{\partial f}{\partial t} + \nabla \cdot \left(\left(\mathbf{v} + U_0 \left(\bar{\alpha}\mathbf{m} + \sqrt{1-\bar{\alpha}^2}\mathbf{m}^{\perp} \right) \right) f \right) = \nabla \cdot D_s^* \left(\nabla f + f \nabla U \right) + \frac{1}{De} \mathcal{R} \cdot \left(\mathcal{R} f + f \mathcal{R} U \right) - \mathcal{R} \cdot \left(\mathbf{m} \times \dot{\mathbf{m}} f \right), \tag{1}$$

where $f(\mathbf{x}, \mathbf{m}, \mathrm{t})$ denotes the number density function corresponding to the probability that the axis of symmetry of a particle at location $\mathbf{x}$ is aligned with the direction $\mathbf{m}$ at time t, and the Navier-Stokes equations,

$$\begin{aligned} \frac{d\mathbf{v}}{dt} &= \nabla \cdot \left(-p\mathbf{I} + \tau_p + \tau_a \right) - \langle \nabla \mu \rangle, \\ \nabla \cdot \mathbf{v} &= 0. \end{aligned} \tag{2}$$

We refer the reader to [7] for the derivation of the model. One can see from (1) that, in three dimensional case, we need to solve for six dimensional problems arisen from $\mathbf{x} \in \mathbb{R}^3$, $\mathbf{m} \in \mathbb{R}^2$, and $t \in \mathbb{R}$. This problem set is very complicated and requires a lot of computational power. In our study, however, we will restrict our attention to two dimensional periodic systems of dilute suspensions. The particles, are assume to move and rotate only in (x, y) plane with orientation parameterized by an angle $\varphi \in [0, 2\pi)$. Hence, the systems become four-dimensional problems ($\mathbf{x} \in \mathbb{R}^2$, $\mathbf{m} \in \mathbb{R}$, and $t \in \mathbb{R}$). The notations, variables, and parameters in (1) and (2) are described below:

- U_0 is the self-propulsion speed.
- $\mathcal{R}$ is the rotational gradient operator given by

$$\mathcal{R} = \frac{\partial}{\partial \varphi} \vec{k},$$

  where $\vec{k}$ is a unitvector pointing in vertical axis.

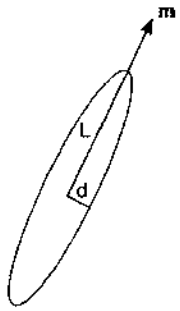

FIGURE 3: Rigid rod-like particle with length L, width d, and direction $\mathbf{m}$.

- $\mathbf{m}$ is the particles orientation with it's perpendicular vector, $\mathbf{m}^{\perp}$. Both are unit vectors and are defined by

$$\mathbf{m} = \begin{bmatrix} \cos\varphi \\ \sin\varphi \end{bmatrix} \text{ and } \mathbf{m}^{\perp} = \begin{bmatrix} -\sin\varphi \\ \cos\varphi \end{bmatrix}.$$

- $\overline{\alpha}$ is a self-propulsion direction parameter. Generally, $\overline{\alpha} = 1$ as we assume that the particle swim along the axis of orientation $\mathbf{m}$.

- De is the Deborah number, or the rotational diffusion coefficient.

- D_s^* is the translational diffusion coefficient.

- U represents the intermolecular potential which is given by

$$(3) \quad U = N_1 \langle 1 \rangle - \gamma \langle \mathbf{m} \rangle \cdot \mathbf{m} - \frac{3N}{2} \langle \mathbf{mm} \rangle : \mathbf{mm}, \ \mathbf{n} = \frac{1}{c} \langle \mathbf{m} \rangle, \ \mathbf{M} = \frac{1}{c} \langle \mathbf{mm} \rangle$$

where N_1, γ, and N are the strength of space inhomogeneity, polarity, and nematic interaction respectively, and c is the characteristic density of the particle. The notation

$$\langle (\cdot) \rangle = \int_0^{2\pi} (\cdot) f(\mathbf{m}, \mathbf{x}, t) \, d\varphi$$

denotes the average over orientational space. Also, note here that the operator $(\cdot)$ and $(:)$ denote tensor contraction.

- $\dot{\mathbf{m}}$ is the Jeffery's orbit describing the rotation of each particle in viscous fluid. The orbit is defined by

$$(4) \qquad \dot{\mathbf{m}} = \Omega \cdot \mathbf{m} + a \left(\mathbf{D} \cdot \mathbf{m} - \mathbf{D} : \mathbf{mmm} \right),$$

where the rate-of-strain tensor, $\mathbf{D}$, and the vorticity tensor, Ω, are defined by

$$\mathbf{D} = \frac{1}{2}\left(\nabla\mathbf{v} + \nabla\mathbf{v}^{\mathrm{T}}\right) \text{ and } \Omega = \frac{1}{2}\left(\nabla\mathbf{v} - \nabla\mathbf{v}^{\mathrm{T}}\right).$$

The parameter a is called geometric particle parameter given by, $a = (r^2 - 1)/(r^2 + 1)$, where r is the particle aspect ratio,$r = L/d$ (see Figure 3). Thus, in the case of long rigid rods, $L >> d$, a is generally close to 1.

- τ_a is the tensor representing the stress generated by the active force of the particle. The active stress tensor is given by

$$\tau_a = G\zeta_a\left(\mathbf{M} - \frac{\langle 1\rangle}{2}\mathbf{I}\right), \tag{5}$$

where G and ζ_a are the anisotropic stress coefficient and the active parameter respectively. Depending on the mechanism for swimming of the self-propelled particle, ζ_a can be either positive or negative: A negative active parameter, $\zeta_a < 0$, indicates that such particle swims using its tail (pusher), whereas a particle that swims using its head (puller) will result in a positive active parameter, $\zeta_a > 0$. Also, note that a zero active parameter, $\zeta_a = 0$, represents a passive particle.

- τ_p is the passive stress, i.e. the stress from the viscous solvent, elasticity of the rod ensemble, and the friction between the active rods and the solvent. The passive stress is given by

$$\begin{aligned}\tau_p = {} & \frac{2}{Re}\mathbf{D} + G\left(\mathbf{M} - \frac{\langle 1\rangle}{2}\mathbf{I} - N\mathbf{M}^2 + \frac{N}{c}\mathbf{M} : \langle\mathbf{mmmm}\rangle\right) \\ & - \frac{\alpha_0 G}{6}\left(2\mathbf{nn} - \frac{1}{c}\left(\langle\mathbf{mmm}\rangle\cdot\mathbf{n} + \mathbf{n}\cdot\langle\mathbf{mmm}\rangle\right)\right) \\ & + \frac{1}{Re_2}\left(\mathbf{D}\cdot\mathbf{M} + \mathbf{M}\cdot\mathbf{D}\right) + \frac{1}{Re_3 c}\langle\mathbf{mmmm}\rangle : \mathbf{D},\end{aligned} \tag{6}$$

where Re is the solvent Reynolds number, Re2 and Re3 are the Reynolds numbers associated with the viscous stress of the particle-solvent interaction, respectively, and α_0 is the polar stress coefficient.

- The body force acting on the fluid results from the interfacial force, $-\langle\nabla\mu\rangle$, which is generated by the chemical potential

$$\mu = \ln f + U. \tag{7}$$

CHAPTER 3

STABILITY AND SCALING BEHAVIOR OF THE DILUTE ACTIVE SUSPENSIONS

In this chapter, we assume that there are no interactions between particles because of the diluteness of the suspensions. This allows us to neglect the spatial dependence of the distribution function, f, i.e. the distribution function is now uniform on entire domain [**28**]. Therefore, (1) reduces to

$$\frac{\partial f}{\partial t} = \frac{1}{De}\mathcal{R}\cdot(\mathcal{R}f + f\mathcal{R}U) - \mathcal{R}\cdot(\mathbf{m}\times\dot{\mathbf{m}})\,f, \tag{8}$$

where f represents $f(\mathbf{m}, t)$. We will use (8) to investigate various properties of the active suspensions with and without imposed shear flows. We also show that, in the special circumstance such as when the suspensions are perturbed by weak shear, many properties of active suspensions can be represented by explicit formulas.

3.1 STABILITY OF ISOTROPIC SUSPENSION

In this section, we consider the stability of the steady isotropic state of the suspensions in the absence of flows. Therefore, (8) further reduces to

$$\begin{aligned}\frac{\partial f}{\partial t} &= \frac{1}{De}\mathcal{R}\cdot(\mathcal{R}f + f\mathcal{R}U)\\ &= \frac{1}{De}\left(\frac{\partial^2 f}{\partial\varphi^2} + \frac{\partial f}{\partial\varphi}\frac{\partial U}{\partial\varphi} + f\frac{\partial^2 U}{\partial\varphi^2}\right),\end{aligned} \tag{9}$$

where U is an integral function of f defined in (3). The normalization condition becomes

$$\int_0^{2\pi} f\,d\varphi = 1. \tag{10}$$

Thus, the steady isotropic state is given by

$$f = \frac{1}{2\pi}. \tag{11}$$

k	Eigenfunction	Eigenvalue
1	$a_1 \sin(\varphi)$	$\frac{\gamma-2c}{2cDe}$
1	$b_1 \cos(\varphi)$	$\frac{\gamma-2c}{2cDe}$
2	$a_2 \sin(2\varphi)$	$\frac{2(N-2c)}{cDe}$
2	$a_2 \cos(2\varphi)$	$\frac{2(N-2c)}{cDe}$
≥ 3	$a_k \sin(k\varphi)$	$\frac{-k^2}{De}$
≥ 3	$b_k \cos(k\varphi)$	$\frac{-k^2}{De}$

TABLE 1: Six categories of the eigenfunctions and their associated eigenvalues of the linearized differential equation.

To study the stability of this state, we linearize the equation by setting

$$f = \frac{1}{2\pi} + \epsilon f_1 \tag{12}$$

and substituting into (9). As a result, we obtain the linearized operator

$$\begin{aligned}\mathcal{L}(f_1) = \frac{f_1''}{De} + \frac{2N\sin(2\varphi)\left(\int_0^{2\pi} f_1 \sin(2\varphi)d\varphi\right)}{\pi cDe} + \frac{2N\cos(2\varphi)\int_0^{2\pi} f_1\cos(2\varphi)d\varphi}{\pi cDe} \\ + \frac{\gamma\sin(\varphi)\left(\int_0^{2\pi} f_1\sin(\varphi)d\varphi\right)}{2\pi cDe} + \frac{\gamma\cos(\varphi)\int_0^{2\pi} f_1\cos(\varphi)d\varphi}{2\pi cDe}.\end{aligned} \tag{13}$$

Because of the orthogonality of the trigonometric function, one can see that the eigenfunctions of the operator $\mathcal{L}$ are scalar multiples of $\sin(k\varphi)$, or $\cos(k\varphi)$, where k is any positive integer. The eigenfunctions and their corresponding eigenvalues are summarized in Table 1. Note that the eigenvalues are always negative for $k \geq 3$. For $k = 1$ and $k = 2$, the eigenvalues are $\frac{\gamma-2c}{2cDe}$ and $\frac{2(N-2c)}{cDe}$ respectively. As a result, the isotropic state is stable for all parameter values, provided $\gamma < 2c$ and $N < 2c$. Since, throughout this research, we fix $c = 1$, our stability region of the isotropic state are $\gamma < 2$ and $N < 2$ as shown in Figure 4.

To confirm the stability condition from our analysis, we also perform the bifurcation analysis numerically using the software AUTO [3]. The general procedure is

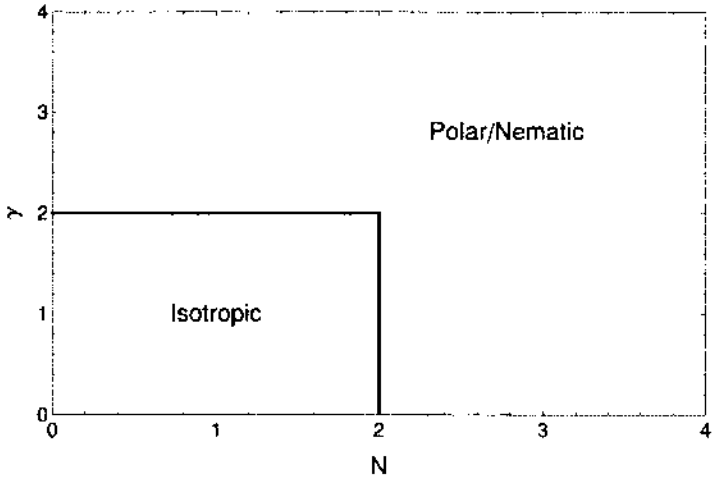

FIGURE 4: Stability region for the strength of polarity, γ, and nematic interaction, N.

to first represent f by the truncated Fourier series

$$f(\mathbf{m},t) \approx b_0(t) + \sum_{k=1}^{K} \left(a_k(t)\sin(k\varphi) + b_k(t)\cos(k\varphi)\right). \tag{14}$$

Then, substitute (14) into (9) to get a system of ordinary differential equations of a_k and b_k as follows (we omit the details of derivation):

$$\begin{aligned}
\frac{\partial b_0}{\partial t} &= 0,\\
\frac{\partial b_1}{\partial t} &= -\frac{1}{De}b_1 + \frac{\pi}{2cDe}\left(2N\left(a_2\left(a_1-a_3\right)+b_2\left(b_1-b_3\right)\right)\right.\\
&\qquad \left.-\gamma\left(a_1a_2+b_1\left(b_2-2b_0\right)\right)\right),\\
\frac{\partial b_2}{\partial t} &= -\frac{4}{De}b_2 - \frac{\pi}{cDe}\left(\left(a_1\left(a_1+a_3\right)+b_1\left(b_3-b_1\right)\right)\right.\\
&\qquad \left.+2N\left(a_2a_4+b_2\left(b_4-2b_0\right)\right)\right),\\
\frac{\partial b_k}{\partial t} &= -\frac{k^2}{De}b_k - \frac{\pi k}{2cDe}\left(\gamma\left(a_1\left(a_{k-1}+a_{k+1}\right)+b_1\left(b_{k+1}-b_{k-1}\right)\right)\right.\\
&\qquad \left.+2N\left(a_2\left(a_{k-2}+a_{k+2}\right)+b_2\left(b_{k+2}-b_{k-2}\right)\right)\right),\\
&\qquad 3\le k\le K,\\
\frac{\partial a_1}{\partial t} &= -\frac{1}{De}a_1 + \frac{\pi}{2cDe}\left(\gamma\left(a_1\left(2b_0+b_2\right)-a_2b_1\right)\right.\\
&\qquad \left.+2N\left(a_2\left(b_1+b_3\right)-\left(a_1+a_3\right)b_2\right)\right),\\
\frac{\partial a_2}{\partial t} &= -\frac{4}{De}a_2 + \frac{\pi}{cDe}\left(\gamma\left(a_2\left(2b_1+b_3\right)-a_3b_1\right)+2N\left(a_2\left(2b_0+b_4\right)-a_4b_2\right)\right),
\end{aligned} \tag{15}$$

Parameter	Value
De	1
c	1
N(when γ is a free parameter)	1
γ (when N is a free parameter)	1

TABLE 2: Parameter values used to produce bifurcation diagram.

$$\frac{\partial a_k}{\partial t} = -\frac{k^2}{De}a_k + \frac{\pi k}{2cDe}\left(\gamma\left(b_1\left(a_{k-1}-a_{k+1}\right)+a_1\left(b_{k+1}+b_{k-1}\right)\right)\right.$$
$$\left.+2N\left(b_2\left(a_{k-2}-a_{k+2}\right)+a_2\left(b_{k-2}+b_{k+2}\right)\right)\right),$$
$$3 \le k \le K,$$

where K is the number of harmonics in (14) and is taken as $K = 20$ in our study. Note that, we define $a_k = 0$, $b_k = 0$ for $k > K$. Next, the numerical bifurcation analysis is perform by supplying (15) to AUTO except b_0 since it is a constant. To characterize the state of the system we employ commonly used measure, which is an order parameter, s, calculated by **[6, 21]**

$$s = \pm\sqrt{\langle\cos(2\varphi)\rangle^2 + \langle\sin(2\varphi)\rangle^2}. \tag{16}$$

We will discuss more about order parameter in the next section. For now, $s = 0$ represents isotropic state of the suspension while $s \neq 0$ indicates that the suspension is in the nematic state. All parameters using in the process are shown in Table 2. Figure 5 shows the bifurcation diagram in the plane of order parameter, s, and the nematic strength, N. The isotropic state is found to be stable up to $N = 2$ as expected. As the nematic strength pass through the pitchfork bifurcation at $N = 2$, the isotropic branch becomes unstable while the stable nematic branches ($s \neq 0$) become the new attractors. As a result, isotropic-to-nematic transition takes place. Similarly, Figure 6 shows stability results by varying polarity potential, γ. As expected, the isotropic state is stable for $\gamma < 2$ and the isotropic-nematic transition occurs at $\gamma = 2$.

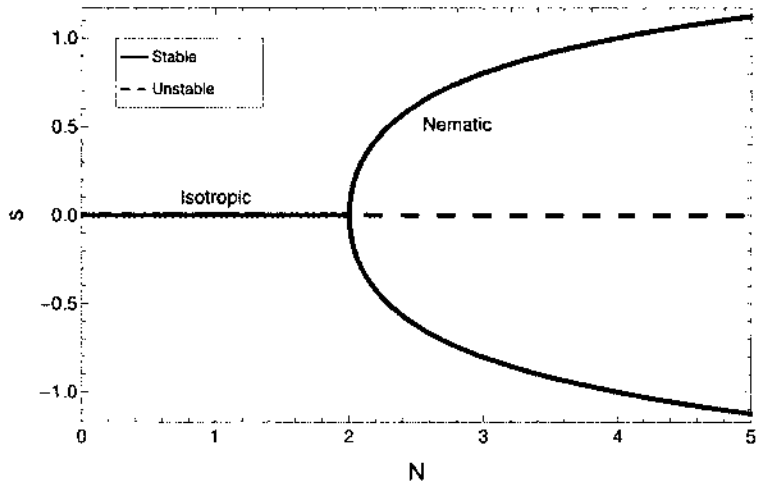

FIGURE 5: Stability of the isotropic and nematic state using the nematic strength, N, as a free parameter. The transition between two state occurs at $N = 2$.

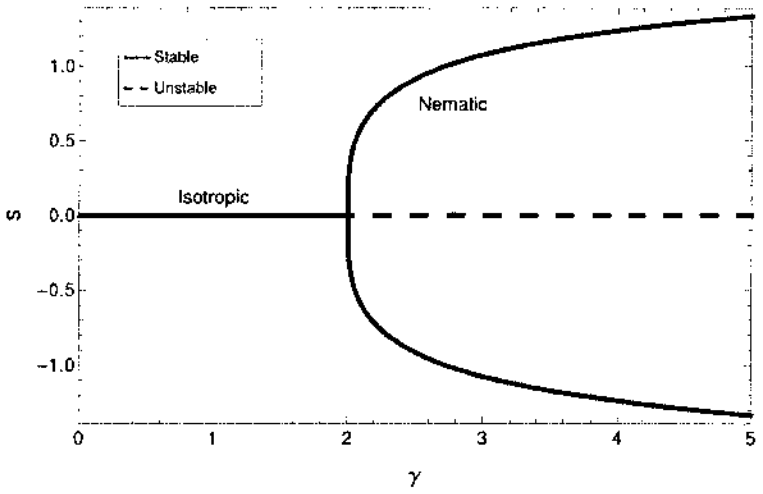

FIGURE 6: Stability of the isotropic and nematic state using the polarity strength, γ, as a free parameter. The transition between two state occurs at $\gamma = 2$.

3.2 ISOTROPIC SUSPENSION WITH WEAK-SHEAR PERTURBATION

Our goal in this section is to show that, in the case of shear perturbed isotropic suspension, the explicit formula for the angle of alignment of the particle and some rheological properties of the fluid can be derived. To see this, we perturb the isotropic state by the weak-shear continuation given, in Cartesian coordinate (x, y), by

$$\mathbf{v} = Pe \begin{bmatrix} y \\ 0 \end{bmatrix}, \tag{17}$$

where Pe is a small Peclet number (non-dimensionalized shear rate). The shear flow is generated by filling the fluid between two parallel plates and then sliding the upper plate to the right while holding the bottom plate. The velocities of intermediate layers of the fluid is assumed to increase linearly in the flow-gradient direction from the bottom to the top (see Figure 7). Note that, in this case, the number density function is given by (8).

From (17), it is straightforward to obtain the rate-of-strain tensor

$$\begin{aligned} \mathbf{D} &= \frac{1}{2}\left(\nabla\mathbf{v} + \nabla\mathbf{v}^{\mathrm{T}}\right) \\ &= \frac{1}{2}\begin{bmatrix} 0 & Pe \\ Pe & 0 \end{bmatrix} \end{aligned} \tag{18}$$

and the vorticity tensor

$$\begin{aligned} \Omega &= \frac{1}{2}\left(\nabla\mathbf{v} - \nabla\mathbf{v}^{\mathrm{T}}\right) \\ &= \frac{1}{2}\begin{bmatrix} 0 & Pe \\ -Pe & 0 \end{bmatrix}. \end{aligned} \tag{19}$$

Hence, the second term of the right-hand side of (8) becomes

$$\begin{aligned} -\mathcal{R}\cdot(\mathbf{m}\times\dot{\mathbf{m}}f) &= -\mathcal{R}\cdot(\mathbf{m}\times(\Omega\cdot\mathbf{m}) + a\mathbf{m}\times(\mathbf{D}\cdot\mathbf{m}))\, f \\ &= \frac{1}{2}\frac{\partial f}{\partial\varphi}\left(Pe - aPe\cos(2\varphi)\right) + af\left(Pe\sin(2\varphi)\right). \end{aligned} \tag{20}$$

We then expand the distribution function, f, in the Peclet number, Pe:

$$f = \frac{1}{2\pi} + Pef_1 + Pe^2 f_2 + Pe^3 f_3 + \ldots \tag{21}$$

Substituting (20) and (21) into the right-hand side of (8) and retaining first and

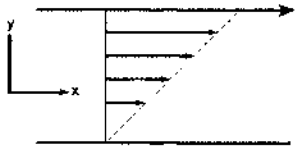

FIGURE 7: Shear flow generated by sliding one plate on top of another.

second order terms yield

$$
\begin{aligned}
&\frac{1}{De}\mathcal{R}\cdot(\mathcal{R}f+f\mathcal{R}U)-\mathcal{R}\cdot(\mathbf{m}\times\dot{\mathbf{m}})f= \\
&\quad Pe\left(\frac{\gamma\cos(\varphi)\int_0^{2\pi}\cos(\varphi)f_1d\varphi}{2\pi cDe}+\frac{2N\cos(2\varphi)\int_0^{2\pi}\cos(2\varphi)f_1d\varphi}{\pi cDe}\right. \\
&\qquad+\frac{\gamma\sin(\varphi)\int_0^{2\pi}f_1\sin(\varphi)d\varphi}{2\pi cDe}+\frac{2N\sin(2\varphi)\int_0^{2\pi}f_1\sin(2\varphi)d\varphi}{\pi cDe} \\
&\qquad\left.+\frac{f_1''}{De}+\frac{a\sin(2\varphi)}{2\pi}\right) \\
&\quad+Pe^2\left(\frac{\gamma\cos(2\varphi)f_1\int_0^{2\pi}\cos(2\varphi)f_1d\varphi}{cDe}+\frac{4N\cos(2\varphi)f_1\int_0^{2\pi}\cos(2\varphi)f_1d\varphi}{cDe}\right. \\
&\qquad+\frac{\gamma\cos(\varphi)\int_0^{2\pi}\cos(\varphi)f_2d\varphi}{2\pi cDe}+\frac{2N\cos(2\varphi)\int_0^{2\pi}\cos(2\varphi)f_2d\varphi}{\pi cDe} \\
&\qquad+\frac{\gamma f_1\sin(\varphi)\int_0^{2\pi}f_1\sin(\varphi)d\varphi}{cDe}+\frac{\gamma\sin(\varphi)\int_0^{2\pi}f_2\sin(\varphi)d\varphi}{2\pi cDe} \\
&\qquad+af_1\sin(2\varphi)+\frac{4Nf_1\sin(2\varphi)\int_0^{2\pi}f_1\sin(2\varphi)d\varphi}{cDe} \\
&\qquad+\frac{2N\sin(2\varphi)\int_0^{2\pi}f_2\sin(2\varphi)d\varphi}{\pi cDe}+\frac{f_1'}{2}-\frac{1}{2}a\cos(2\varphi)f_1' \\
&\qquad-\frac{\gamma\cos(\varphi)f_1'\int_0^{2\pi}f_1\sin(\varphi)d\varphi}{cDe}-\frac{2N\cos(2\varphi)f_1'\int_0^{2\pi}f_1\sin(2\varphi)d\varphi}{cDe} \\
&\qquad+\frac{\gamma\sin(\varphi)f_1'\int_0^{2\pi}\cos(\varphi)f_1d\varphi}{cDe}+\frac{2N\sin(2\varphi)f_1'\int_0^{2\pi}\cos(2\varphi)f_1d\varphi}{cDe} \\
&\qquad\left.+\frac{f_2''}{De}\right)+O\left(Pe^3\right),
\end{aligned}
\tag{22}
$$

where the prime symbol ($'$) indicates the derivative respect to angle, φ.

Consider the first-order terms in (22). For the steady state, we have

$$
\begin{aligned}
&\frac{f_1''}{De}+\frac{1}{2\pi cDe}\left(\gamma\left(\cos(\varphi)\int_0^{2\pi}f_1\cos(\varphi)d\varphi+\sin(\varphi)\int_0^{2\pi}f_1\sin(\varphi)d\varphi\right)\right. \\
&\quad\left.+4N\left(\cos(2\varphi)\int_0^{2\pi}f_1\cos(2\varphi)d\varphi+\sin(2\varphi)\int_0^{2\pi}f_1\sin(2\varphi)d\varphi\right)\right) \\
&\quad+\frac{a\sin(2\varphi)}{2\pi}=0.
\end{aligned}
\tag{23}
$$

Using the orthogonality of the trigonometric functions, the solution for this integral-differential equation is

$$f_1 = \frac{acDe}{4\pi\,(2c-N)}\sin(2\varphi)\,. \tag{24}$$

By substituting (24) into the second order term in (22), we have, after simplification, the steady state equation for f_2:

$$\begin{aligned}\frac{f_2''}{De} + \frac{1}{2\pi cDe}\Bigg(\gamma\Bigg(\cos(\varphi)\int_0^{2\pi} f_2\cos(\varphi)d\varphi + \sin(\varphi)\int_0^{2\pi} f_2\sin(\varphi)d\varphi\Bigg) \\ + 4N\Bigg(\cos(2\varphi)\int_0^{2\pi} f_2\cos(2\varphi)d\varphi + \sin(2\varphi)\int_0^{2\pi} f_2\sin(2\varphi)d\varphi\Bigg)\Bigg) \\ - \frac{a^2c^2De\cos(4\varphi)}{2\pi(2c-N)^2} + \frac{acDe\cos(2\varphi)}{4\pi(2c-N)} = 0.\end{aligned} \tag{25}$$

We again have the integral-differential equation. The solution can be explicitly given by

$$f_2 = \frac{ac^2De^2}{8\pi(2c-N)^2}\cos(2\varphi) - \frac{a^2c^2De^2}{32\pi(2c-N)^2}\cos(4\varphi)\,. \tag{26}$$

From (24) and (26) , the second-order approximation for the number density function in weak shear is

$$\begin{aligned}f \approx \frac{1}{2\pi} + Pe\left(\frac{acDe}{4\pi\,(2c-N)}\sin(2\varphi)\right) \\ + Pe^2\left(\frac{ac^2De^2}{8\pi(2c-N)^2}\cos(2\varphi) - \frac{a^2c^2De^2}{32\pi(2c-N)^2}\cos(4\varphi)\right).\end{aligned} \tag{27}$$

Note that higher order approximation can be done in the same manner. From (27), some closed-form approximations of alignment and rheological properties can be recovered by direct substitution. We first look into details about the alignment properties of the shear-perturbed isotropic state. One convention to measure the orientation is to project f onto the symmetric traceless second-moment tensor, $\mathbf{Q}$ [**10**].

$$\begin{aligned}\mathbf{Q} &= \langle\mathbf{mm}\rangle - \frac{\mathbf{I}}{2} \\ &= \begin{bmatrix} \langle\cos^2\varphi\rangle - \frac{1}{2} & \langle\cos\varphi\sin\varphi\rangle \\ \langle\sin\varphi\cos\varphi\rangle & \langle\sin^2\varphi\rangle - \frac{1}{2}\end{bmatrix} \\ &= Pe\frac{acDe}{8(2c-N)}\begin{bmatrix}0 & 1\\ 1 & 0\end{bmatrix} + Pe^2\frac{ac^2De^2}{16(2c-N)^2}\begin{bmatrix}1 & 0\\ 0 & -1\end{bmatrix}.\end{aligned} \tag{28}$$

The eigenvalues of $\mathbf{Q}$ through $O(Pe^2)$ are

$$\lambda_1 = \frac{acDePe\sqrt{c^2De^2Pe^2 + 4(2c-N)^2}}{16(2c-N)^2}, \tag{29}$$

and

$$\lambda_2 = -\frac{acDePe\sqrt{c^2De^2Pe^2 + 4(2c-N)^2}}{16(2c-N)^2}. \tag{30}$$

Our next task is to get the major director, $\mathbf{n_1}$, and the order parameter s. The major director is a unit vector

$$\mathbf{n_1} = \begin{bmatrix} \cos(\psi) \\ \sin(\psi) \end{bmatrix},$$

which indicates the preferred orientation of the molecules. It is defined to be aligned with the eigenvector, ν_1, associated with the largest eigenvalue, λ_1. The order parameter is a non-negative scalar,

$$s = \lambda_1 - \lambda_2,$$

which indicates the degree of alignment. Clearly, the state in which $s = 0$ implies the isotropic state.

From (28), it is straightforward to obtain

$$\nu_1 = \left(cDePe + \sqrt{c^2De^2Pe^2 + 4(2c-N)^2}\,,\ 2(2c-N)\right).$$

Obviously, the alignment angle, ψ, which is defined as the angle between the major director and the flow direction, can be computed by

$$\psi = \tan^{-1}\left(\frac{2(2c-N)}{cDePe + \sqrt{c^2De^2Pe^2 + 4(2c-N)^2}}\right). \tag{31}$$

Note that the value in the parenthesis is smaller than 1, thus $|\psi| < 45°$. This result suggests that, being perturbed at isotropic state by weak shear, the molecules break their random orientation by shifting primary alignment along the flow direction. Another clue we can see from (31) is that the alignment angle in the weak shear limit, $Pe \to 0$, is 45° given $N < 2c$, or −45° given $N > 2c$, although the latter case is unstable as will be seen in section 3.3. In fact, it is also interesting to see, from

Parameter	Value
a	1
Pe (if not a free parameter)	0.1
c	1
De	2
γ	1
N_1	1

TABLE 3: Parameter values used in comparison between theoretical approximations of alignment properties and numerical results.

the explicit formula, that the alignment angle, ψ, does not depend on geometrical property of particle, a. We now verify if our analysis is consistent with the numerical simulations. Simultaneously, we study more carefully about the alignment angle, order parameter, and other rheological properties.

Figure 8 shows the alignment angle versus weak shear with five different values of nematic strength, N. The molecular and flow parameters chosen are shown in Table 3. The solid line is the predicted angle given by (31) while the dots represent the results from numerical simulations. It is clear from the figure that the alignment angle is a decreasing function of Pe as we expect from the formula. That is, as the shear rate increases, the major director becomes more aligned with the flow direction. For five values of nematic strength, the numerical results confirm our second-order explicit formula as well as the alignment angle of 45° in the weak shear limit. The prediction performs best at low nematic strength but start to fall off as nematic strength increase toward the critical isotropic-nematic transition value, $N = 2$. Form (29) and (30), the order parameter is

$$s = \frac{acDePe\sqrt{c^2De^2Pe^2 + 4(2c - N)^2}}{8(2c - N)^2}. \tag{32}$$

For comparison, we again plot the values from explicit formula (32) together with the numerical results in Figure 9 , which shows the scaling behavior of the degree of alignment versus the nematic strength. The parameters chosen are listed in Table 3. It is clearly seen that our approximation works very well at low nematic strength and weak shear. As the nematic strength increases, the order parameter also increases. So the particles are more likely to align with the flow direction.

Another noteworthy result is the construction of f in (27) does not contain $\cos(\varphi)$,

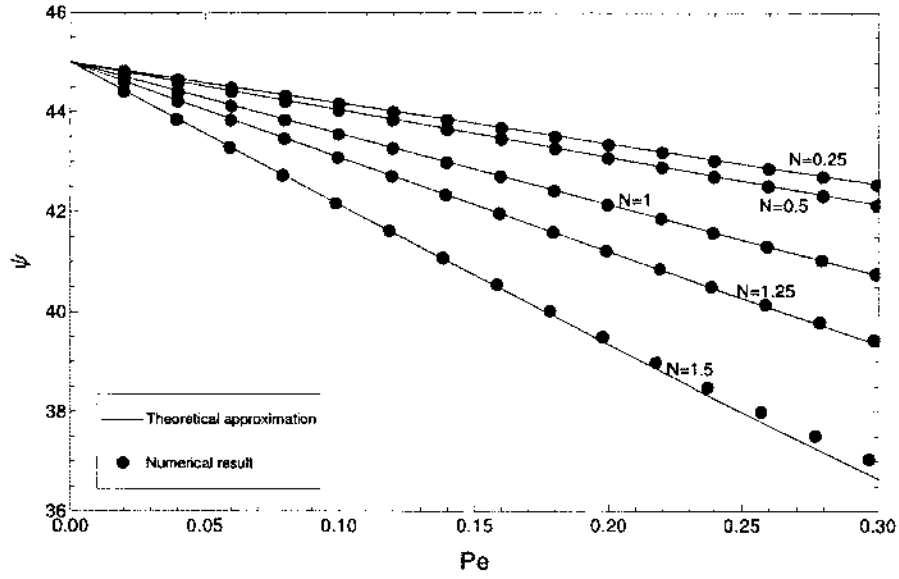

FIGURE 8: Comparison of scaling behavior between explicit formula (solid line) of the alignment angle and numerical results (dots).

$\sin(\varphi)$ or any other $\cos(k\varphi)$, $\sin(k\varphi)$ components with k odd. Now, if we consider the polarization vector (mean director field),

$$\mathbf{p} = \langle \mathbf{m} \rangle = \begin{bmatrix} \langle \cos(\varphi) \rangle \\ \langle \sin(\varphi) \rangle \end{bmatrix}, \tag{33}$$

we will have $\mathbf{p} = 0$. That is, there is no polarity. We now derive closure approximation for rheological properties of the shear-perturbed suspension, which are the viscosity (apparent stress), σ, and the normal stress difference, $\mathcal{N}_1$. The viscosity determines a fluid's resistance to flow whereas the normal stress difference generates a force pushing the plate apart or pulling them together. These two rheological properties are very useful in polymer characterization.

The viscosity, σ, and the normal stress difference, $\mathcal{N}_1$, are given by

$$\sigma = \tau_{12}/Pe \text{ and } \mathcal{N}_1 = \tau_{11} - \tau_{22},$$

where $\tau = \tau_p + \tau_a$ is the stress tensor. At this point we refer the reader to (5) and (6) for the equation of stress tensor, τ. From (27), we notice that, apart from molecular and flow parameters, only b_0 ,a_2 , b_2, and b_4 have non-zero values.

Therefore,

$$\sigma = \frac{\tau_{12}}{Pe} = \frac{\pi a_2 G(\zeta_a + 1)}{2cPe} + \frac{\pi b_0}{cRe_2} + \frac{\pi(2b_0 - b_4)}{8cRe_3} + \frac{1}{Re} - \frac{\pi^2 a_2 (2b_0 + b_4) GN}{8c^2 Pe} \tag{34}$$

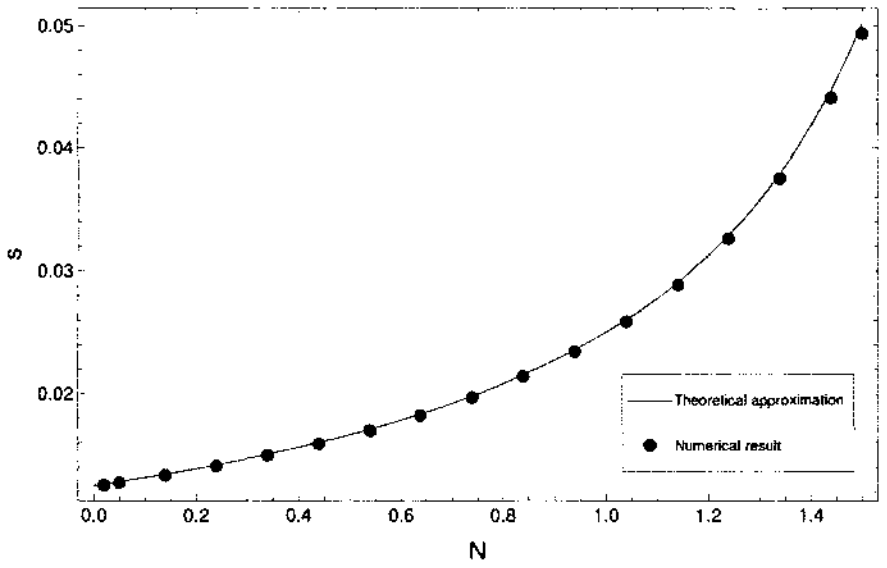

FIGURE 9: The comparison between theoretical approximations (solid line) of the degree of alignment, s, and the numerical results (dots).

and

$$\mathcal{N}_1 = \tau_{11} - \tau_{22} = \frac{\pi b_2 G\left(\zeta_a + 1\right)}{c} - \frac{\pi^2 b_2 G N\left(2b_0 - b_4\right)}{4c^2}. \tag{35}$$

Hence, we finally have

$$\sigma = \frac{aDeG\left(4c\zeta_a + 4c - N\right)}{32c(2c-N)} + \frac{1}{2cRe_2} + \frac{1}{8cRe_3} + \frac{1}{Re} + \left(\frac{a^3 cDe^3 GN}{1024(2c-N)^3} + \frac{a^2 cDe^2}{256Re_3(2c-N)^2}\right) Pe^2 \tag{36}$$

and

$$\mathcal{N}_1 = \frac{aDe^2G\left(4c\zeta_a + 4c - N\right)}{32(2c-N)^2} Pe^2 - \frac{a^3c^2De^4GN}{1024(2c-N)^4} Pe^4. \tag{37}$$

In Figure 10, the viscosity is plotted as a function of nematic strength, N, for suspensions of pullers ($\zeta_a > 0$), pushers ($\zeta_a < 0$), and passive particles ($\zeta_a = 0$). All parameters chosen are shown in Table 4. Regardless of the fact that the formula will blow up as the nematic strength increases toward the region of isotropic-nematic transition ($N \to 2$) the scaling behaviors of all suspensions from our approximation are consistent with numerical values given sufficiently low nematic strength. As nematic strength increases, the viscosity of the suspension with puller-type particles

Parameter	Value
a	1
De	1
G	2
c	1
γ	1
N_1	1
Re	15
Re_2	15
Re_3	15
α_0	1

TABLE 4: Parameter values used in comparison between theoretical approximations of rheological properties and numerical results.

also increase while the reverse effect happens for suspension with pusher-type particles. This effect is alleviated for suspension with passive particles as increasing in nematic strength has minimal effect to viscosity. The positive effect of pusher and negative effect of puller to the viscosity of active suspensions in weak flows are also suggested in other models [**15, 28**]. This phenomenon is also supported by experimental results from Sokolov and Aranson [**35**] in which they concluded that the combined action of swimming bacteria (pushers) can reduce the viscosity of a liquid by up to a factor of seven. The experiment in the case of puller particles is also reported by Rafaï et al. [**27**] where they observed a significant increase in viscosity as a result of the swimming activity of microalgae (pullers).

Similar results can be observed in Figure **11**, where the first normal stress difference, $\mathcal{N}_1$, is plot against nematic strength, N, except that the differences in the effect of active particle is more apparent as N approach 2. It is interesting to see that, when the effect of nematic strength are negligible ($N = 0$) all suspensions feature nearly equivalent normal stress difference. The nearly zero values of $\mathcal{N}_1$ in a weak shear for all type of suspensions are expected since the formula for normal stress difference is of order $O(Pe^2)$.

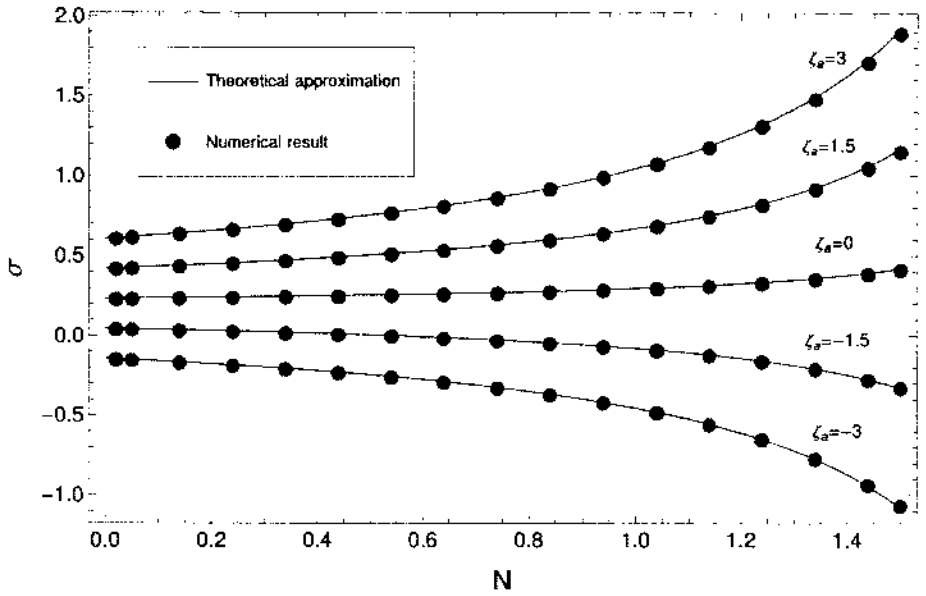

FIGURE 10: The comparison between theoretical approximations (solid line) of the viscosity, σ, and the numerical results (dots). The active parameter, ζ_a, vary from -3 to 3.

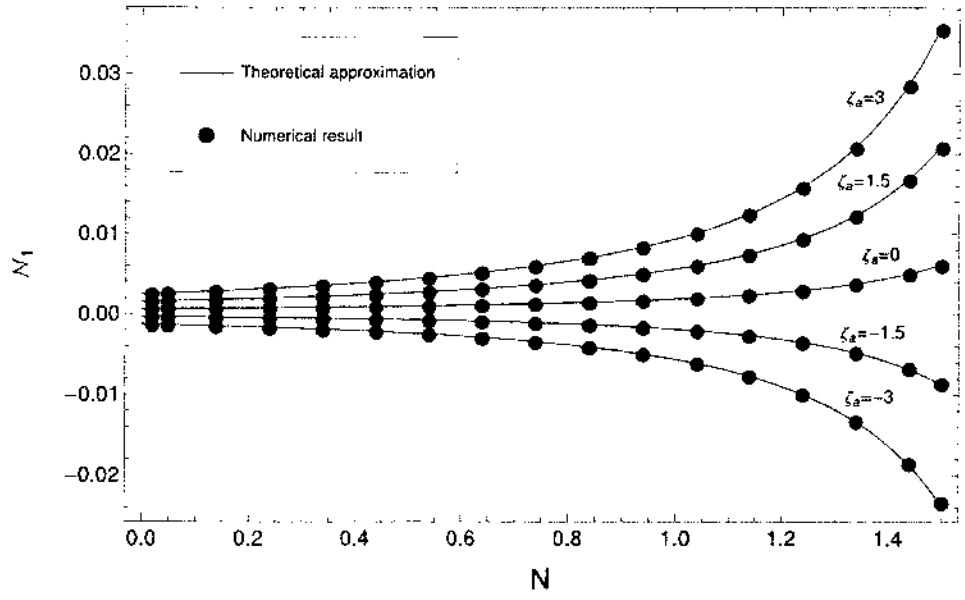

FIGURE 11: The comparison between theoretical approximations (solid line) of the normalized first normal stress difference, $\mathcal{N}_1$, and the numerical results (dots). The active parameter, ζ_a, vary from -3 to 3.

3.3 DILUTE ACTIVE SUSPENSION IN THE IMPOSED SHEAR FLOWS

From the analysis of the suspension in weak shear, we continue our investigation on monodomain suspension with general shear flow. The density function is still described by (8). But, the shear flow is now not necessary weak, i.e. Pe is not necessarily small. As previously done in section 3.1, we fist derive the differential equation for the Fourier modes by substituting (14) into (8). We now obtain

$$
\begin{aligned}
\frac{\partial b_0}{\partial t} =& 0, \\
\frac{\partial b_1}{\partial t} =& -\frac{1}{De} b_1 + \frac{\pi}{2cDe} \left(2N \left(a_2 \left(a_1 - a_3\right) + b_2 \left(b_1 - b_3\right)\right)\right. \\
& \left. -\gamma \left(a_1 a_2 + b_1 \left(b_2 - 2b_0\right)\right)\right) + \frac{Pe}{4} \left(\left(a+2\right)a_1 - a a_3\right), \\
\frac{\partial b_2}{\partial t} =& -\frac{4}{De} b_2 - \frac{\pi}{cDe} \left(\left(a_1 \left(a_1 + a_3\right) + b_1 \left(b_3 - b_1\right)\right)\right. \\
& \left. +2N \left(a_2 a_4 + b_2 \left(b_4 - 2b_0\right)\right)\right) + \frac{Pe}{2} \left(2a_2 - a a_4\right), \\
\frac{\partial b_k}{\partial t} =& -\frac{k^2}{De} b_k - \frac{\pi k}{2cDe} \left(\gamma \left(a_1 \left(a_{k-1} + a_{k+1}\right) + b_1 \left(b_{k+1} - b_{k-1}\right)\right)\right. \\
& \left. +2N \left(a_2 \left(a_{k-2} + a_{k+2}\right) + b_2 \left(b_{k+2} - b_{k-2}\right)\right)\right) \\
& - \frac{kPe}{4} \left(a \left(a_{k-2} + a_{k+2}\right) - 2a_k\right), 3 \leq k \leq K, \qquad (38) \\
\frac{\partial a_1}{\partial t} =& -\frac{1}{De} a_1 + \frac{\pi}{2cDe} \left(\gamma \left(a_1 \left(2b_0 + b_2\right) - a_2 b_1\right)\right. \\
& \left. +2N \left(a_2 \left(b_1 + b_3\right) - \left(a_1 + a_3\right) b_2\right)\right) + \frac{Pe}{4} \left(\left(a-2\right)b_1 + a b_3\right), \\
\frac{\partial a_2}{\partial t} =& -\frac{4}{De} a_2 + \frac{\pi}{cDe} \left(\gamma \left(a_2 \left(2b_1 + b_3\right) - a_3 b_1\right) + 2N \left(a_2 \left(2b_0 + b_4\right) - a_4 b_2\right)\right) \\
& + \frac{Pe}{2} \left(2a \left(b_0 + b_4\right) - 2b_2\right), \\
\frac{\partial a_k}{\partial t} =& -\frac{k^2}{De} a_k + \frac{\pi k}{2cDe} \left(\gamma \left(b_1 \left(a_{k-1} - a_{k+1}\right) + a_1 \left(b_{k+1} + b_{k-1}\right)\right)\right. \\
& \left. +2N \left(b_2 \left(a_{k-2} - a_{k+2}\right) + a_2 \left(b_{k-2} + b_{k+2}\right)\right)\right) \\
& + \frac{1}{4} k \mathrm{Pe} \left(a \left(b_{k-2} + b_{k+2}\right) - 2b_k\right), 3 \leq k \leq K.
\end{aligned}
$$

Again, we define $a_k = 0$, $b_k = 0$ for $k > K$ and the number of harmonics is chosen to be $K = 20$. One can see that b_0 is still a constant in this case and will be excluded from our concern.

All figures in this section illustrate results obtained by considering the shear rate as a free parameter. Each figure consists of two graphs- one showing the degree of

Parameter	Value
a	1
De	5
c	1
α_0	1

TABLE 5: Parameter values used in shear sweep analysis.

alignment s, and the other showing the angle of alignment ψ. Both s and ψ are calculated by the definition mentioned in previous section. Note that, in the case of periodic solution, we represent s and ψ as follows:

$$s = \pi\sqrt{\overline{a_2}^2 + \overline{b_2}^2},\ \psi = \tan^{-1}\left(\frac{\overline{a_2}}{\overline{b_2} + \sqrt{\overline{a_2}^2 + \overline{b_2}^2}}\right), \tag{39}$$

where

$$\overline{(.)} = \frac{1}{T}\int_0^T (.)\, dt, \tag{40}$$

and T is the period. Different bifurcation diagrams result from different values of nematic strength, N, and polarity strength, γ. Other parameters using throughout this section are shown in Table 5.

We find that, for all nematic and polarity strength below the isotropic-nematic transition values ($N < 2$ and $\gamma < 2$), only one stable stationary solution branch appears. Figure 12 shows the solution diagram for $N = 1$ and $\gamma = 1$. In Figure 12a, increasing in the flow strength results in increasing in the degree of alignment. In fact, as one might expect, this behavior always happen in all cases (see Figure 12,13,15,19). In Figure 12b, the angle of alignment, ψ, is plotted as a function of shear rate, Pe. As we already discussed in previous section, the alignment angle tends to 45° for vanishing shear rate. The decreasing function shown in the figure implies that the stronger flows (high Pe) induce the particles to align with the flows direction ($\psi = 0$). In fact, flow-aligning always occurs at strong flow (high Pe) regardless of the nematic and polarity strength (see Figure 12,13,15,19).

Figure 13 presents the bifurcation diagram for larger nematic strength, $N = 4$ and $\gamma = 1$. We can see that both periodic and steady solutions, which are represented by thick and ordinary solid line respectively, arise in this setup. The periodic solutions emerge from Hopf bifurcation labeled as **HB**, at $Pe \approx 2.36$. This is also where the

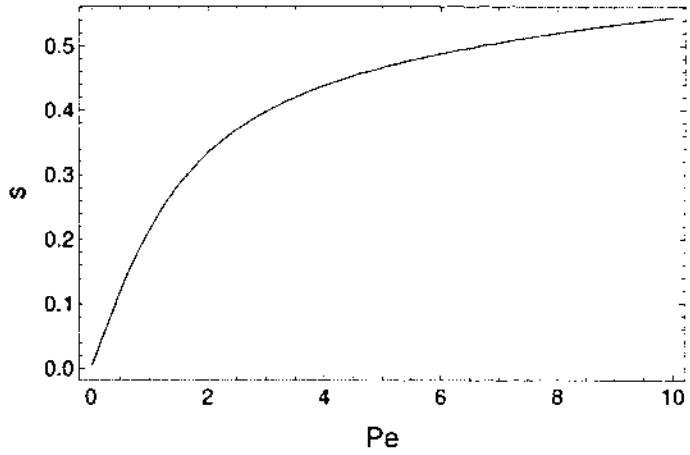

(a) Order parameter, s, versus shear rate, Pe.

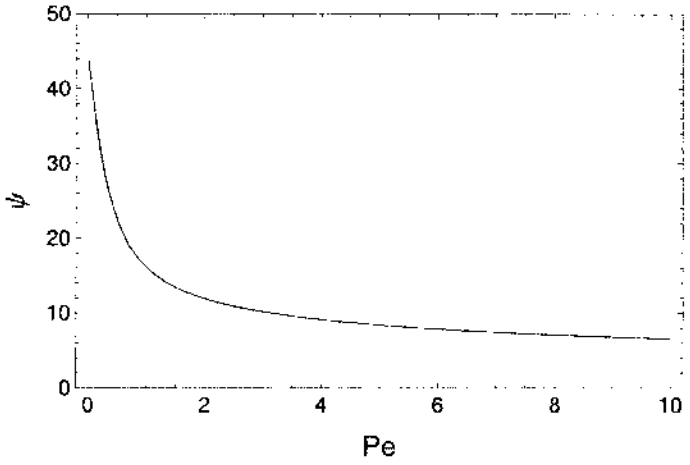

(b) Alignment angle, ψ, versus shear rate, Pe.

FIGURE 12: Bifurcation diagram for $N = 1$ and $\gamma = 1$. Other parameters are shown in Table 5.

transition between wagging/tumbling (periodic solution) and flow-aligning (steady solution) take places. For $Pe < 2.36$, unlike the previous case, the steady branch is now unstable while the periodic branch is always stable. This implies that in the weak shear limit the particles exhibit oscillatory responses instead of steady alignment of $-45°$ indicated by closed-form formula (31). For $Pe > 2.3$ the particles appear to be steady aligned, with orientation closer to the flow direction ($\psi = 0$) as indicated by steady branch. Figure 14 shows the diagram of flow-aligning and wagging/tumbling regimes in the (N, Pe) plane. The two states are separated by a solid line which represents Hopf bifurcation line. We clearly see from the figure that,

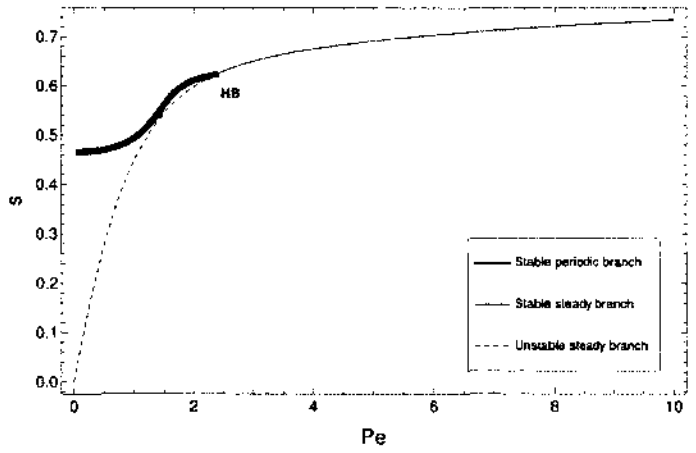

(a) Order parameter, s, versus shear rate, Pe.

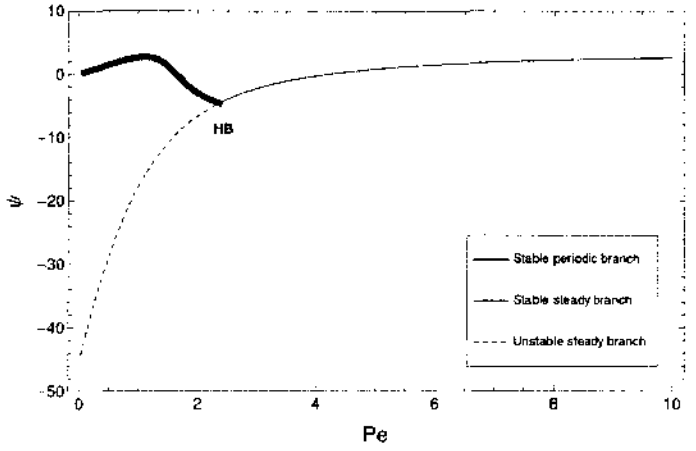

(b) Alignment angle, ψ, versus shear rate, Pe.

FIGURE 13: Bifurcation diagram for $N = 4$ and $\gamma = 1$. Other parameters are shown in Table 5.

for the suspensions with low nematic strength, N, any oscillatory responses from exerted shear flow are impossible. The figure also suggests that, even the particle is in the wagging/tumbling state, the flow-aligning always occurs given strong enough shear flows (high Pe).

Similar diagrams are observed in Figure 15. Here, parameters chosen are low nematic strength, $N = 1$, and high strength of polarity, $\gamma = 4$. In this case, the transition between wagging/tumbling and flow-aligning state occurs at $Pe \approx 1.84$, which is marked by **HB**. Figure 15b reveals that the oscillatory response still occurs in the weak shear limit even with $N < 2$. This suggest that the closed-form formula

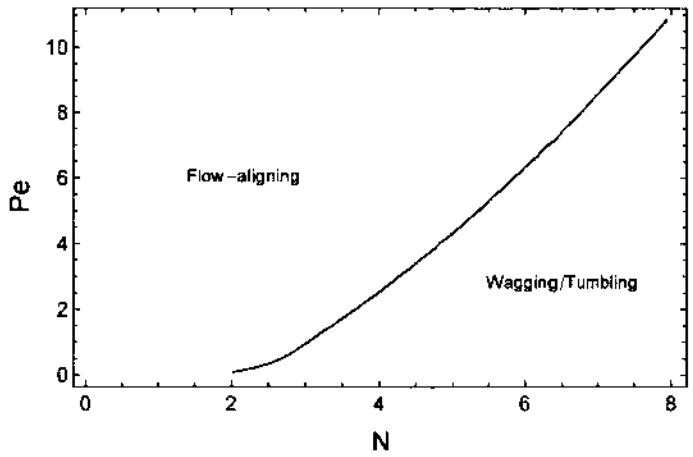

FIGURE 14: Critical flow strength, Pe, below which an oscillation response (wagging/tumbling) occurs, as a function of nematic strength, N. The solid line is the Hopf bifurcation line.

(31) is valid only in the range of $N < 2$ and $\gamma < 2$. Figure 16 shows the range of shear rates and polarity strengths for which the particles exhibit oscillatory, or steady, response. Here, we take the opportunity to show some examples of wagging and tumbling state of the particles. If we choose $\gamma = 4$ and $Pe = 1$, the active particle will be in the tumbling state as seen in Figure 17. The top-left and the bottom-left figure show the periodic fluctuation (with the period ≈ 9.6) of the degree of alignment, s, and the polarity magnitude, $|\mathbf{p}|$, respectively as time evolves. The top-right figure presents the angle of nematic orientation, ψ, as a function of time. The angle oscillates between $-90°$ and $90°$, which indicates the tumbling behavior of the particle. The similar periodic pattern can be observed in bottom-right figure presenting the polarity angle, ϕ, as a function of time. The wagging state can be discovered by choosing $\gamma = 8$ and $Pe = 6$. Figure 18 shows similar (with higher frequency) periodic behavior of s, $|\mathbf{p}|$, and ϕ to those in Figure 17, except for ψ that oscillates between $0.6°$ and $16°$, which clearly indicates that nematic orientation of the particle is in the wagging state.

Another interesting stability result is shown in Figure 19 for $N = 5$ and $\gamma = 9$. In this setup, the first Hopf bifurcation, **HB1**, and the second Hopf bifurcation, **HB2**, appear at $Pe \approx 4.12$ and $Pe \approx 7.70$, respectively. The first periodic branch associated with **HB1** has no physical effect to the particles since it is unstable. The second periodic branch emerging from **HB2**, however, consists of stable and

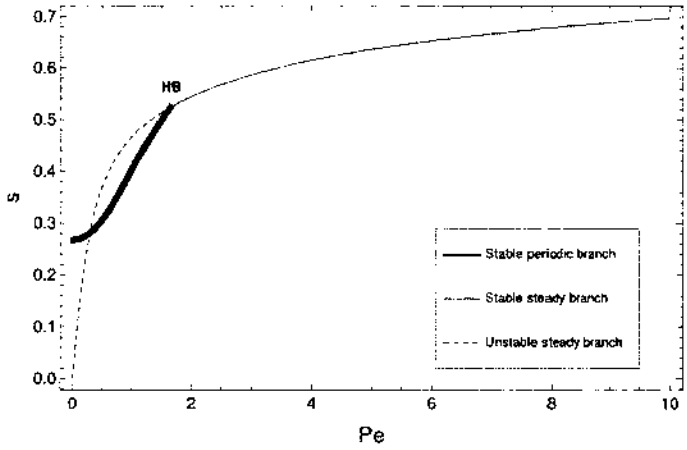

(a) Order parameter, s, versus shear rate, Pe.

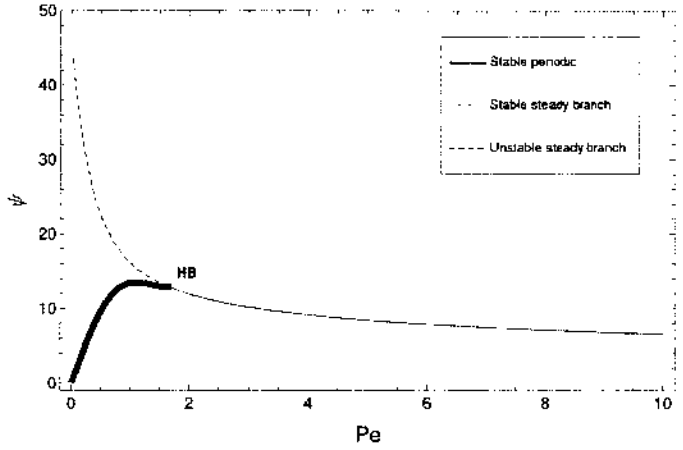

(b) Alignment angle, ψ, versus shear rate, Pe.

FIGURE 15: Bifurcation diagram for $N = 1$ and $\gamma = 4$. Other parameters are shown in Table 5.

unstable periodic solution with the turning point at $Pe \approx 8.20$ marked by the limit point bifurcation, **LP**. Consider the shear rate in the regime around **HB2** and **LP** ($7.70 < Pe < 8.20$). This is a bistable region, where both steady flow-aligning and wagging/tumbling state coexist, and both are stable. If the wagging/tumbling states first arise, the transition from wagging/tumbling state to flow-aligning occurs when $Pe > 8.20$. Conversely, the transition from flow-aligning to wagging/tumbling state take places when $Pe < 7.70$.

Some interesting rheological properties of spatially homogeneous suspension in shear flow are also investigated. For all results presented below, the nematic and the

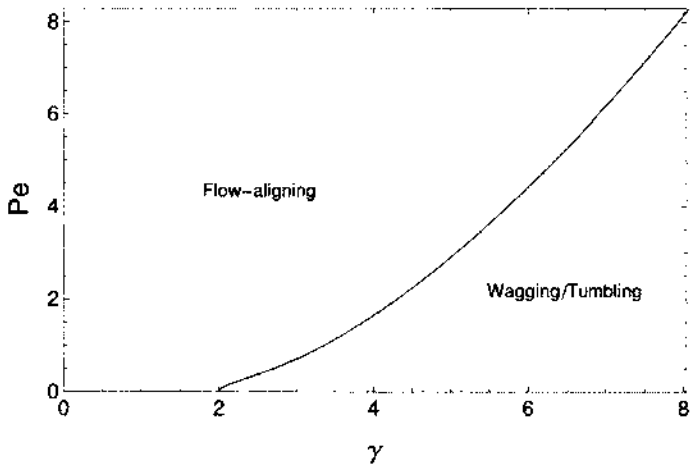

FIGURE 16: Critical flow strength, Pe, below which an oscillation response (wagging/tumbling) occurs, as a function of polarity strength, γ. The solid line is the Hopf bifurcation line.

polarity strength are chosen to be $N = 1$ and $\gamma = 1$, respectively. Other parameters chosen are shown in Table 5. The viscosity, σ is plotted against Peclet number, Pe in Figure 20. Both suspension of puller, $\zeta_a > 0$, and suspension of passive particle, $\zeta_a = 0$, exhibit shear thinning behavior, whereas suspension of pusher, $\zeta_a < 0$, shows shear thickening. It can be seen that the effect of swimming mechanism is strongest in weak flows and vanishes in strong flows (high Pe). An enchantments of σ in puller-type suspensions, and the opposite in pusher-type suspensions, in weak flows (low Pe), have been mentioned in previous section. This phenomenon is shown more clearly in Figure 21 showing the range of active parameter, ζ_a, and shear rate, Pe, for which $\sigma < 0$, or $\sigma > 0$. The critical line in the figure confirms that negative viscosity will occur in weak flows of strongly active pusher suspension. Figure 22 shows first normal stress difference coefficient, $\mathcal{N}_1/Pe$, as a function of shear rate, Pe, for pullers, pushers, and passive particles. The effect of swimming mechanism increases as the shear rate increases and is strongest at $Pe \approx 0.5$. After that, similar to the case of viscosity, the effect of activity degenerate to nearly zero in strong flows. The normal stress difference coefficient of all particles exhibit both increasing and decreasing function depending on shear rate. A suspension of pullers and passive particles behaves as increasing function for $\mathcal{N}_1 < 0.5$ then operates as decreasing function for $\mathcal{N}_1 > 0.5$. The behaviors in the case of suspension of pusher are reversed. The negative first normal stress difference coefficient occuring in suspensions of pushers

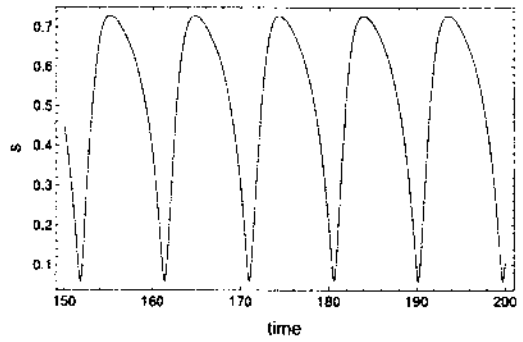

(a) Order parameter, s, versus time.

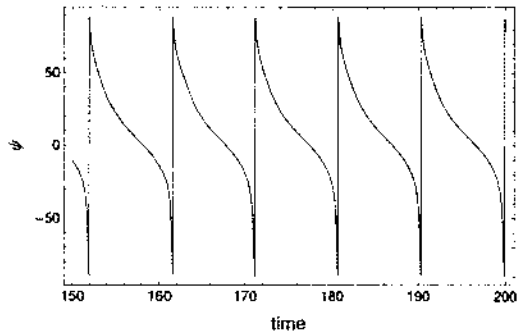

(b) Alignment angle, ψ, versus time.

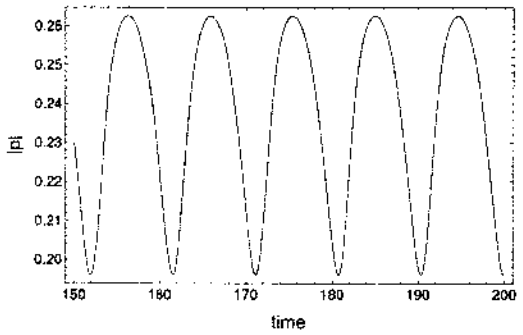

(c) Magnitude of polarization direction, $|\mathbf{p}|$, versus time.

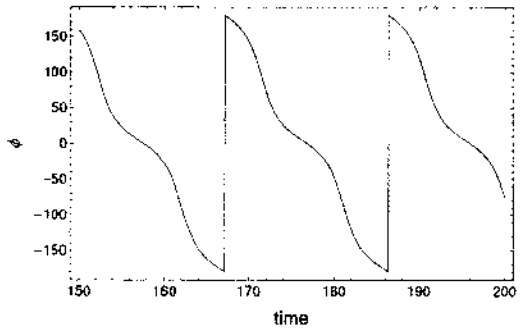

(d) Angle of polarization direction, ϕ, versus time.

FIGURE 17: Time evolution of the order parameter, s, the alignment angle ,ψ, the polarity magnitude ,$|\mathbf{p}|$, and the polarity angle ,ϕ, during the tumbling state ($\gamma = 4, Pe = 1$).

is illustrated more clearly in Figure 23. One can clearly see from the figure that the negative normal stress difference almost always occur in weak flow. However, changing in sign will eventually take place at strong flow.

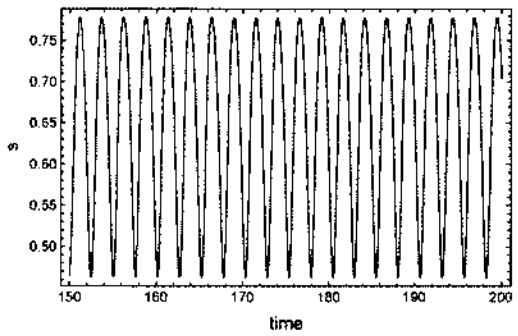

(a) Order parameter, s, versus time.

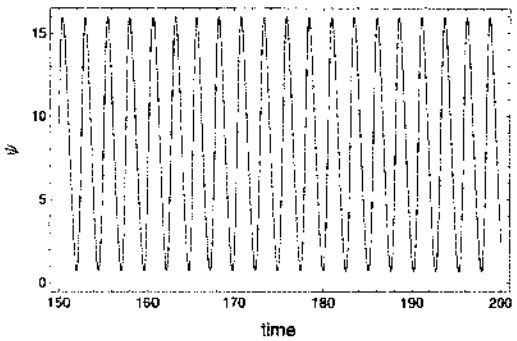

(b) Alignment angle, ψ, versus time.

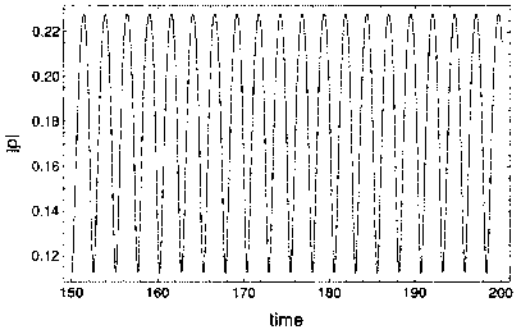

(c) Magnitude of polarization direction, $|\mathbf{p}|$, versus time.

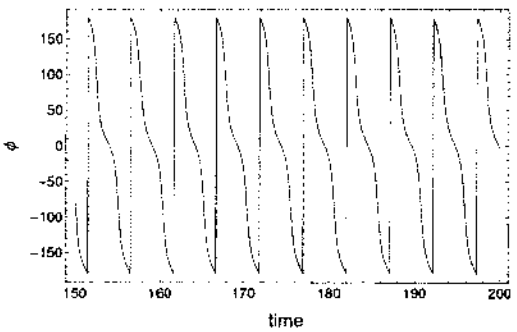

(d) Angle of polarization direction, ϕ, versus time.

FIGURE 18: Time evolution of the order parameter, s, the alignment angle ,ψ, the polarity magnitude ,$|\mathbf{p}|$, and the polarity angle ,ϕ, during the wagging state ($\gamma = 8, Pe = 6$).

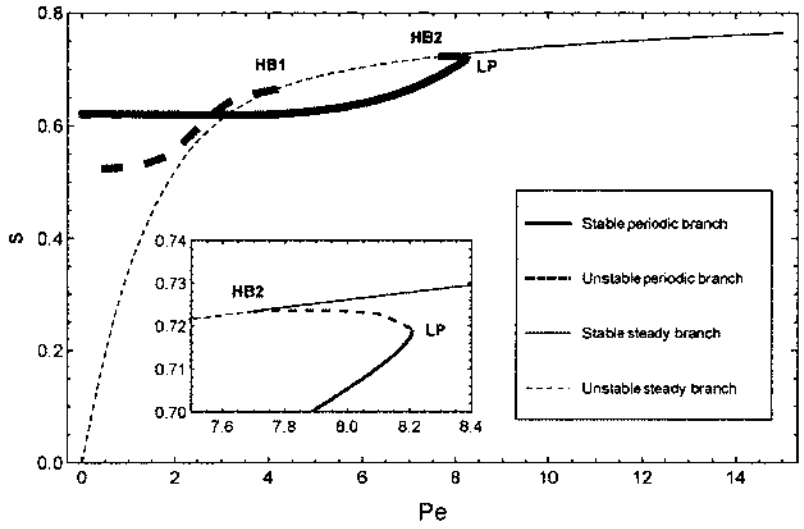

(a) Order parameter, s, versus shear rate, Pe. The inset shows details of a portion of Pe values.

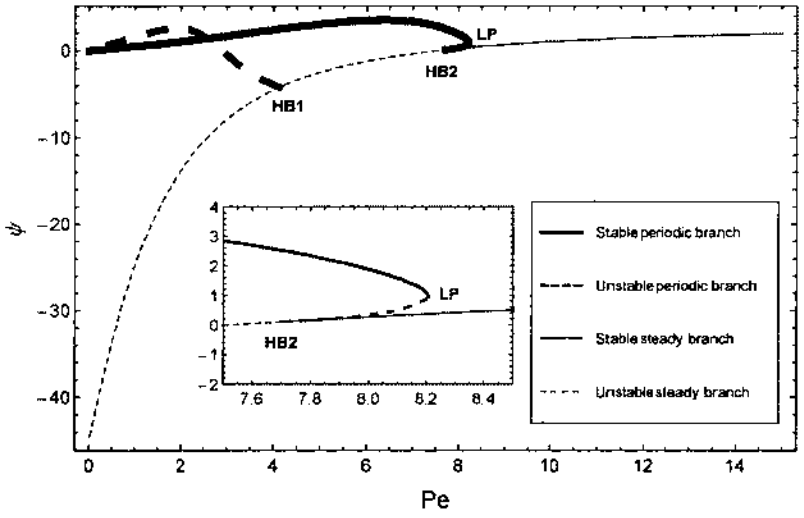

(b) Alignment angle, ψ, versus shear rate, Pe. The inset shows details of a portion of Pe values.

FIGURE 19: Bifurcation diagram for $N = 5$ and $\gamma = 9$. Other parameters are shown in Table 5.

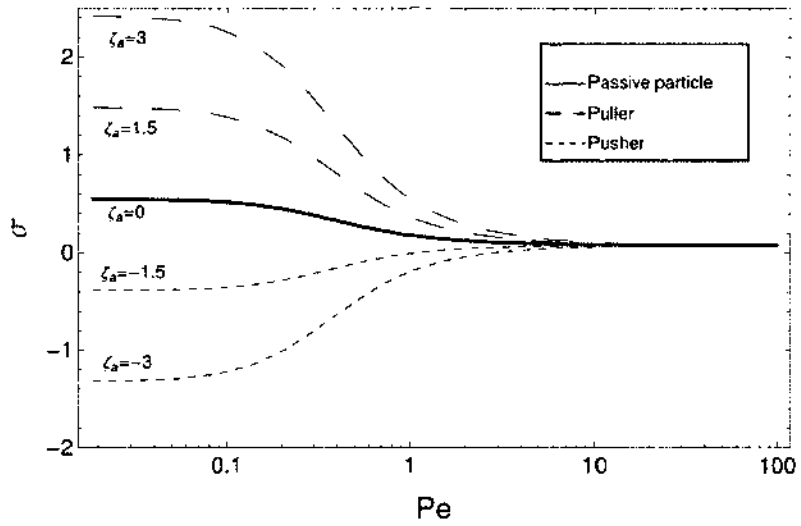

FIGURE 20: Viscosity σ versus shear rate Pe in dilute suspension, $N = 1$, and low strength of polarity, $\gamma = 1$. Other parameters are shown in Table 5. The various curves corresponds to different values of the active parameters, ζ_a.

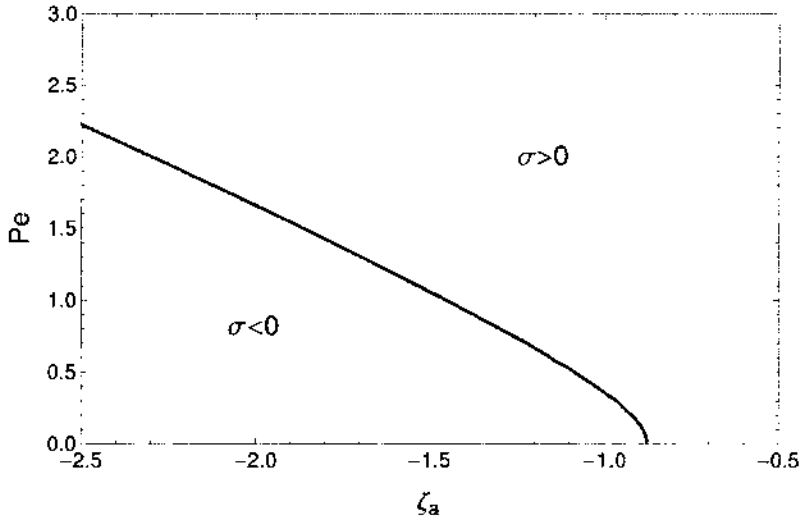

FIGURE 21: Region of active parameter ζ_a and the Peclet number Pe for which $\sigma < 0$, or $\sigma > 0$.

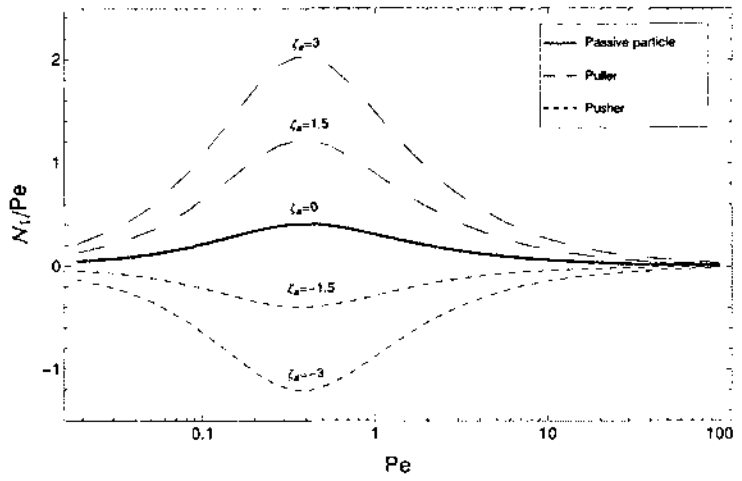

FIGURE 22: Normal stress difference coefficient $\mathcal{N}_1/Pe$ versus shear rate Pe in dilute suspension, $N = 1$, and low strength of polarity, $\gamma = 1$. Other parameters are shown in Table 5. The various curves corresponds to different values of the active parameters, ζ_a.

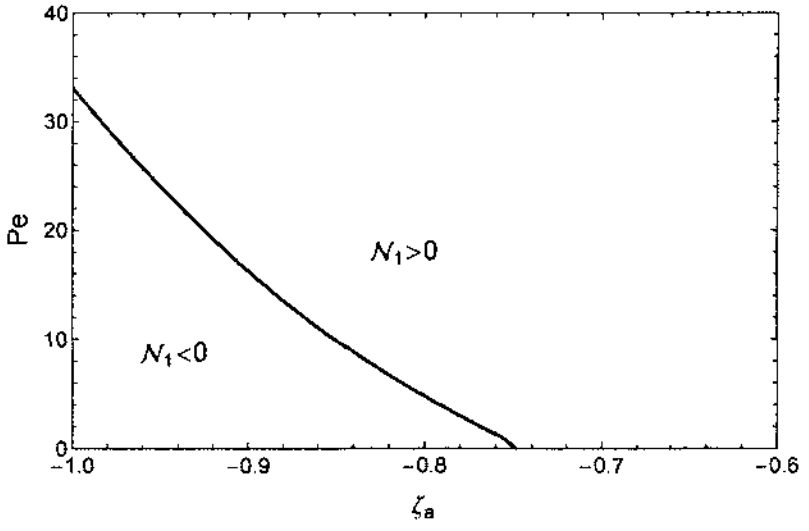

FIGURE 23: The range of active parameter ζ_a and the Peclet number Pe for which $\mathcal{N}_1 < 0$, or $\mathcal{N}_1 > 0$.

CHAPTER 4

SPATIO-TEMPORAL STRUCTURES OF ACTIVE SUSPENSIONS

In this chapter, we drop the relaxation of the previous chapter, i.e. the interactions between particles are now taken into account. Therefore, the equation for the distribution function, f, given by (1) is fully utilized without the homogeneous assumption of the physical domain. The procedures in this chapter are as follows. First, we derive a system of partial differential equations for the Fourier modes of f from (1). Then, this system together with the Navier-Stokes equation in (2) are solved numerically. After that, we study various behaviors and structures of the active suspensions systematically by projecting the microscopic information onto macroscopic variables such as the local concentration, the polarization direction, the nematic orientation, and the degree of alignment.

4.1 GALERKIN PROCEDURE FOR THE SMOLUCHOWSKI EQUATION

Recall that the system in three dimensional case is a complex 6 dimensional problem. Due to the extensive computational cost and the complex physical phenomena, it is almost impossible to solve it directly numerically. Here we make the assumption that, all particles are on the flow-flow gradient (x-y) plane. This reduces the system to a 4 dimensional problem (2D in space, 1D in orientation, and 1D in time). As a result, we can approximate the distribution function by truncated Fourier series

$$f(\mathbf{x},\mathbf{m},t) \approx b_0(\mathbf{x},t) + \sum_{k=1}^{K} \left(a_k(\mathbf{x},t)\sin(k\varphi) + b_k(\mathbf{x},t)\cos(k\varphi)\right). \tag{41}$$

Our ultimate goal in this section is to obtain a set of partial differential equations of the Fourier coefficients by substituting (41) into (1). It is more convenient if we consider substitution term by term.

Firstly, it is easy to see that

$$\mathcal{R}\cdot\mathcal{R}f = -\sum_{k=0}^{K} \left(k^2 a_k \sin(k\varphi) + k^2 b_k \cos(k\varphi)\right) \tag{42}$$

and

$$\nabla^2 f = \sum_{k=0}^{K} \left(\nabla^2 a_k \sin(k\varphi) + \nabla^2 b_k \cos(k\varphi) \right). \tag{43}$$

Consider the convection term, we have

$$\begin{aligned} \nabla \cdot \left(\left(\mathbf{v} + U_0 \left(\bar{\alpha}\mathbf{m} + \sqrt{1-\bar{\alpha}^2}\mathbf{m}^{\perp} \right) \right) f \right) &= \mathbf{v} \cdot (\nabla f) + U_0 \bar{\alpha} (\mathbf{m} \cdot \nabla f) \\ &\quad + U_0 \sqrt{1-\bar{\alpha}^2} \left(\mathbf{m}^{\perp} \cdot \nabla f \right). \end{aligned} \tag{44}$$

Substituting (41) into the right-had side of (44) gives

$$\mathbf{v} \cdot (\nabla f) = \mathbf{v} \cdot \nabla b_0 + \sum_{k=1}^{K} \left(\mathbf{v} \cdot \nabla a_k \sin(k\varphi) + \mathbf{v} \cdot \nabla b_k \cos(k\varphi) \right) \tag{45}$$

and

$$\begin{aligned} & U_0 \bar{\alpha} (\mathbf{m} \cdot \nabla f) + U_0 \sqrt{1-\bar{\alpha}^2} \left(\mathbf{m}^{\perp} \cdot \nabla f \right) = \\ & \left(U_0 \bar{\alpha} \frac{\partial b_0}{\partial y} - U_0 \sqrt{1-\bar{\alpha}^2} \frac{\partial b_0}{\partial x} \right) \sin(\varphi) + \left(U_0 \bar{\alpha} \frac{\partial b_0}{\partial x} + U_0 \sqrt{1-\bar{\alpha}^2} \frac{\partial b_0}{\partial y} \right) \cos(\varphi) \\ & + \sum_{k=1}^{K} \Bigg\{ \left(\frac{U_0 \bar{\alpha}}{2} \left(\frac{\partial a_k}{\partial x} - \frac{\partial b_k}{\partial y} \right) + \frac{U_0 \sqrt{1-\bar{\alpha}^2}}{2} \left(\frac{\partial a_k}{\partial y} + \frac{\partial b_k}{\partial x} \right) \right) \sin((k-1)\varphi) \\ & \quad + \left(\frac{U_0 \bar{\alpha}}{2} \left(\frac{\partial a_k}{\partial x} + \frac{\partial b_k}{\partial y} \right) + \frac{U_0 \sqrt{1-\bar{\alpha}^2}}{2} \left(\frac{\partial a_k}{\partial y} - \frac{\partial b_k}{\partial x} \right) \right) \sin((k+1)\varphi) \\ & \quad + \left(\frac{U_0 \bar{\alpha}}{2} \left(\frac{\partial a_k}{\partial y} + \frac{\partial b_k}{\partial x} \right) + \frac{U_0 \sqrt{1-\bar{\alpha}^2}}{2} \left(\frac{\partial b_k}{\partial y} - \frac{\partial a_k}{\partial x} \right) \right) \cos((k-1)\varphi) \\ & \quad + \left(\frac{U_0 \bar{\alpha}}{2} \left(\frac{\partial b_k}{\partial x} - \frac{\partial a_k}{\partial y} \right) + \frac{U_0 \sqrt{1-\bar{\alpha}^2}}{2} \left(\frac{\partial b_k}{\partial y} + \frac{\partial a_k}{\partial x} \right) \right) \cos((k+1)\varphi) \Bigg\}. \end{aligned} \tag{46}$$

Given definition of $\mathbf{m}$ and $\langle(\cdot)\rangle$, we have

$$\langle \mathbf{m} \rangle = \begin{bmatrix} \langle \cos\varphi \rangle \\ \langle \sin\varphi \rangle \end{bmatrix} = \begin{bmatrix} b_1 \pi \\ a_1 \pi \end{bmatrix} \tag{47}$$

and

$$\langle \mathbf{mm} \rangle = \begin{bmatrix} \langle \cos^2\varphi \rangle & \langle \cos\varphi \sin\varphi \rangle \\ \langle \sin\varphi \cos\varphi \rangle & \langle \sin^2\varphi \rangle \end{bmatrix} = \begin{bmatrix} b_0\pi + \frac{b_2\pi}{2} & \frac{a_2\pi}{2} \\ \frac{a_2\pi}{2} & b_0\pi - \frac{b_2\pi}{2} \end{bmatrix}. \tag{48}$$

Substituting (47) and (48) into (3) leads to

$$U = \left(N_1 - \frac{N}{c} \right) 2\pi b_0 - \frac{\gamma\pi}{c} \left(b_1 \cos(\varphi) + a_1 \sin(\varphi) \right) \tag{49}$$

$$- \frac{N\pi}{c} \left(b_2 \cos(2\varphi) + a_2 \sin(2\varphi) \right).$$

By substituting (41) and (49) into the translational diffusion term, we have

$$\begin{aligned}
D_s^* \nabla \cdot (f \nabla U) = & - \frac{D_s^* N\pi}{c} \nabla \cdot (b_0 \nabla a_2) \sin(2\varphi) - \frac{D_s^* \gamma\pi}{c} \nabla \cdot (b_0 \nabla a_1) \sin(\varphi) \\
& + \frac{2 D_s^* (N_1 c - N) \pi}{c} \nabla \cdot (b_0 \nabla b_0) \\
& - \frac{D_s^* N\pi}{c} \nabla \cdot (b_0 \nabla b_2) \cos(2\varphi) - \frac{D_s^* \gamma\pi}{c} \nabla \cdot (b_0 \nabla b_1) \cos(\varphi) \\
& + \sum_{k=1}^{K} \left\{ \frac{2 D_s^* (N_1 c - N) \pi}{c} \nabla \cdot (a_k \nabla b_0) \sin(k\varphi) \right. \\
& + \frac{D_s^* N\pi}{2c} \left(\nabla \cdot (b_k \nabla a_2) - \nabla \cdot (a_k \nabla b_2) \right) \sin((k-2)\varphi) \\
& + \frac{D_s^* \gamma\pi}{2c} \left(\nabla \cdot (b_k \nabla a_1) - \nabla \cdot (a_k \nabla b_1) \right) \sin((k-1)\varphi) \\
& - \frac{D_s^* \gamma\pi}{2c} \left(\nabla \cdot (b_k \nabla a_1) + \nabla \cdot (a_k \nabla b_1) \right) \sin((k+1)\varphi) \\
& - \frac{D_s^* N\pi}{2c} \left(\nabla \cdot (b_k \nabla a_2) + \nabla \cdot (a_k \nabla b_2) \right) \sin((k+2)\varphi) \\
& + \frac{2 D_s^* (N_1 c - N) \pi}{c} \nabla \cdot (b_k \nabla b_0) \cos(k\varphi) \\
& - \frac{D_s^* N\pi}{2c} \left(\nabla \cdot (b_k \nabla b_2) + \nabla \cdot (a_k \nabla a_2) \right) \cos((k-2)\varphi) \\
& - \frac{D_s^* \gamma\pi}{2c} \left(\nabla \cdot (b_k \nabla b_1) + \nabla \cdot (a_k \nabla a_1) \right) \cos((k-1)\varphi) \\
& + \frac{D_s^* \gamma\pi}{2c} \left(\nabla \cdot (a_k \nabla a_1) - \nabla \cdot (b_k \nabla b_1) \right) \cos((k+1)\varphi) \\
& \left. + \frac{D_s^* N\pi}{2c} \left(\nabla \cdot (a_k \nabla a_2) - \nabla \cdot (b_k \nabla b_2) \right) \cos((k+2)\varphi) \right\}.
\end{aligned} \tag{50}$$

Substituting (41) into the rotational diffusion term, yields

$$\begin{aligned}
\frac{1}{De} R \cdot (fRU) = & \frac{1}{De} \frac{\partial f}{\partial \varphi} \left(\frac{\gamma\pi}{c} \left(b_1 \sin(\varphi) - a_1 \cos(\varphi) \right) \right. \\
& \left. + \frac{2N\pi}{c} \left(b_2 \sin(2\varphi) - a_2 \cos(2\varphi) \right) \right) \\
& + \frac{1}{De} f \left(\frac{\gamma\pi}{c} \left(b_1 \cos(\varphi) + a_1 \sin(\varphi) \right) \right. \\
& \left. + \frac{4N\pi}{c} \left(b_2 \cos(2\varphi) + a_2 \sin(2\varphi) \right) \right) \\
= & \frac{4N\pi}{cDe} b_0 a_2 \sin(2\varphi) + \frac{\gamma\pi}{cDe} b_0 a_1 \sin(\varphi)
\end{aligned} \tag{51}$$

$$
\begin{aligned}
&+\frac{4N\pi}{cDe}b_0b_2\cos(2\varphi)+\frac{\gamma\pi}{cDe}b_0b_1\cos(\varphi)\\
&+\sum_{k=1}^{K}\left\{\frac{(k-2)N\pi}{cDe}(b_ka_2-a_kb_2)\sin((k-2)\varphi)\right.\\
&+\frac{(k-1)\gamma\pi}{2cDe}(b_ka_1-a_kb_1)\sin((k-1)\varphi)\\
&+\frac{(k+1)\gamma\pi}{2cDe}(a_kb_1+b_ka_1)\sin((k+1)\varphi)\\
&+\frac{(k+2)N\pi}{cDe}(a_kb_2+b_ka_2)\sin((k+2)\varphi)\\
&-\frac{(k-2)N\pi}{cDe}(a_ka_2+b_kb_2)\cos((k-2)\varphi)\\
&-\frac{(k-1)\gamma\pi}{2cDe}(a_ka_1+b_kb_1)\cos((k-1)\varphi)\\
&+\frac{(k+1)\gamma\pi}{2cDe}(b_kb_1-a_ka_1)\cos((k+1)\varphi)\\
&\left.+\frac{(k+2)N\pi}{cDe}(b_kb_2-a_ka_2)\cos((k+2)\varphi)\right\}.
\end{aligned}
$$

In the same manner, the last term of the Smoluchowski equation can be written as

$$
\begin{aligned}
(52)\qquad -\mathcal{R}\cdot(\mathbf{m}\times\dot{\mathbf{m}}f) &= -\mathcal{R}\cdot(\mathbf{m}\times(\Omega\cdot\mathbf{m})+a\mathbf{m}\times(\mathbf{D}\cdot\mathbf{m}))f\\
&=\frac{1}{2}\frac{\partial f}{\partial\varphi}(\omega_{12}-ad_{12}\cos(2\varphi)+ad_{11}\sin(2\varphi))\\
&\quad+af(d_{11}\cos(2\varphi)+d_{12}\sin(2\varphi))\\
&=ab_0d_{12}\sin(2\varphi)+ab_0d_{11}\cos(2\varphi)\\
&\quad+\sum_{k=1}^{K}\left\{-\frac{k}{2}b_k\omega_{12}\sin(k\varphi)\right.\\
&\quad+\frac{a(k-2)}{4}(b_kd_{12}-a_kd_{11})\sin((k-2)\varphi)\\
&\quad+\frac{a(k+2)}{4}(b_kd_{12}+a_kd_{11})\sin((k+2)\varphi)\\
&\quad+\frac{k}{2}a_k\omega_{12}\cos(k\varphi)\\
&\quad-\frac{a(k-2)}{4}(b_kd_{11}+a_kd_{12})\cos((k-2)\varphi)\\
&\quad\left.+\frac{a(k+2)}{4}(b_kd_{11}-a_kd_{12})\cos((k+2)\varphi)\right\},
\end{aligned}
$$

where, given $\mathbf{v}=(v_x,v_y)$,

$$
(53)\qquad d_{11}=2\frac{\partial v_x}{\partial x}\text{ and }d_{12}=\frac{\partial v_x}{\partial y}+\frac{\partial v_y}{\partial x}
$$

are the components of the rate-of-strain tensor

$$\mathbf{D} = \frac{1}{2}\begin{bmatrix} d_{11} & d_{12} \\ d_{12} & -d_{11} \end{bmatrix},$$

and

$$\omega_{12} = \frac{\partial v_x}{\partial y} - \frac{\partial v_y}{\partial x} \tag{54}$$

is the component of vorticity tensor

$$\Omega = \frac{1}{2}\begin{bmatrix} 0 & \omega_{12} \\ -\omega_{12} & 0 \end{bmatrix}.$$

The final procedure is straightforward. We substitute (42), (43), (45), (46), (50), (51), and (52) into (1). Subsequently, we collect and equate like modes to get a set of partial differential equations of the Fourier coefficients as follows:

$$\frac{\partial b_0}{\partial t} = D_s^* \nabla^2 b_0 - (F_2 + G_1 + H_0), \tag{55}$$

$$\frac{\partial b_1}{\partial t} = D_s^* \nabla^2 b_1 - \frac{1}{De} b_1 - (F_3 + F_1 + G_2 + G_0 + H_1 + I_0), \tag{56}$$

$$\frac{\partial b_2}{\partial t} = D_s^* \nabla^2 b_2 - \frac{4}{De} b_2 - (F_4 + F_0 + G_3 + H_2 + I_1 + J_0), \tag{57}$$

$$\frac{\partial b_k}{\partial t} = D_s^* \nabla^2 b_k - \frac{k^2}{De} b_k - (F_{k+2} + G_{k+1} + H_k + I_{k-1} + J_{k-2}), \quad 3 \le k \le K, \tag{58}$$

$$\frac{\partial a_1}{\partial t} = D_s^* \nabla^2 a_1 - \frac{1}{De} a_1 - (A_3 - A_1 + B_2 - B_0 + C_1 + D_0), \tag{59}$$

$$\frac{\partial a_2}{\partial t} = D_s^* \nabla^2 a_2 - \frac{4}{De} a_2 - (A_4 - A_0 + B_3 + C_2 + D_1 + E_0), \tag{60}$$

$$\frac{\partial a_k}{\partial t} = D_s^* \nabla^2 a_k - \frac{k^2}{De} a_k - (A_{k+2} + B_{k+1} + C_k + D_{k-1} + E_{k-2}), \quad 3 \le k \le K, \tag{61}$$

where

$$A_k = \frac{D_s^* N\pi}{2c} (\nabla \cdot (a_k \nabla b_2) - \nabla \cdot (b_k \nabla a_2)) - \frac{(k-2)N\pi}{cDe} (b_k a_2 - a_k b_2) \tag{62}$$

$$- \frac{a\,(k-2)}{4}\left(b_k\left(\frac{\partial v_x}{\partial y}+\frac{\partial v_y}{\partial x}\right)-2a_k\frac{\partial v_x}{\partial x}\right),$$

(63) $$B_k = \frac{U_0\overline{\alpha}}{2}\frac{\partial a_k}{\partial x}+\frac{U_0\sqrt{1-\overline{\alpha}^2}}{2}\frac{\partial a_k}{\partial y}-\frac{U_0\overline{\alpha}}{2}\frac{\partial b_k}{\partial y}+\frac{U_0\sqrt{1-\overline{\alpha}^2}}{2}\frac{\partial b_k}{\partial x}$$
$$+\frac{D_s^*\gamma\pi}{2c}\left(\nabla\cdot(a_k\nabla b_1)-\nabla\cdot(b_k\nabla a_1)\right)+\frac{(k-1)\gamma\pi}{2cDe}\left(a_kb_1-b_ka_1\right),$$

(64) $$C_k = \mathbf{v}\cdot\nabla a_k-\frac{2D_s^*\left(N_1c-N\right)\pi}{c}\nabla\cdot(a_k\nabla b_0)+\frac{k}{2}b_k\left(\frac{\partial v_x}{\partial y}-\frac{\partial v_y}{\partial x}\right),$$

(65) $$D_k = \frac{U_0\overline{\alpha}}{2}\frac{\partial a_k}{\partial x}+\frac{U_0\sqrt{1-\overline{\alpha}^2}}{2}\frac{\partial a_k}{\partial y}+\frac{U_0\overline{\alpha}}{2}\frac{\partial b_k}{\partial y}-\frac{U_0\sqrt{1-\overline{\alpha}^2}}{2}\frac{\partial b_k}{\partial x}$$
$$+\frac{D_s^*\gamma\pi}{2c}\left(\nabla\cdot(b_k\nabla a_1)+\nabla\cdot(a_k\nabla b_1)\right)-\frac{(k+1)\gamma\pi}{2cDe}\left(a_kb_1+b_ka_1\right),$$

(66) $$E_k = \frac{D_s^*N\pi}{2c}\left(\nabla\cdot(b_k\nabla a_2)+\nabla\cdot(a_k\nabla b_2)\right)-\frac{(k+2)N\pi}{cDe}\left(a_kb_2+b_ka_2\right)$$
$$-\frac{a\,(k+2)}{4}\left(b_k\left(\frac{\partial v_x}{\partial y}+\frac{\partial v_y}{\partial x}\right)+2a_k\frac{\partial v_x}{\partial x}\right),$$

(67) $$F_k = \frac{D_s^*N\pi}{2c}\left(\nabla\cdot(b_k\nabla b_2)+\nabla\cdot(a_k\nabla a_2)\right)+\frac{(k-2)N\pi}{cDe}\left(a_ka_2+b_kb_2\right)$$
$$+\frac{a\,(k-2)}{4}\left(2b_k\frac{\partial v_x}{\partial x}+a_k\left(\frac{\partial v_x}{\partial y}+\frac{\partial v_y}{\partial x}\right)\right),$$

(68) $$G_k = \frac{U_0\overline{\alpha}}{2}\frac{\partial a_k}{\partial y}-\frac{U_0\sqrt{1-\overline{\alpha}^2}}{2}\frac{\partial a_k}{\partial x}+\frac{U_0\overline{\alpha}}{2}\frac{\partial b_k}{\partial x}+\frac{U_0\sqrt{1-\overline{\alpha}^2}}{2}\frac{\partial b_k}{\partial y}$$
$$+\frac{D_s^*\gamma\pi}{2c}\left(\nabla\cdot(b_k\nabla b_1)+\nabla\cdot(a_k\nabla a_1)\right)+\frac{(k-1)\gamma\pi}{2cDe}\left(a_ka_1+b_kb_1\right),$$

(69) $$H_k = \mathbf{v}\cdot\nabla b_k-\frac{2D_s^*\left(N_1c-N\right)\pi}{c}\nabla\cdot(b_k\nabla b_0)-\frac{k}{2}a_k\left(\frac{\partial v_x}{\partial y}-\frac{\partial v_y}{\partial x}\right),$$

(70) $$I_k = \frac{U_0\overline{\alpha}}{2}\frac{\partial b_k}{\partial x}+\frac{U_0\sqrt{1-\overline{\alpha}^2}}{2}\frac{\partial b_k}{\partial y}-\frac{U_0\overline{\alpha}}{2}\frac{\partial a_k}{\partial y}+\frac{U_0\sqrt{1-\overline{\alpha}^2}}{2}\frac{\partial a_k}{\partial x}$$
$$-\frac{D_s^*\gamma\pi}{2c}\left(\nabla\cdot(a_k\nabla a_1)-\nabla\cdot(b_k\nabla b_1)\right)-\frac{(k+1)\gamma\pi}{2cDe}\left(b_kb_1-a_ka_1\right),$$

and

(71) $$J_k = \frac{D_s^*N\pi}{2c}\left(\nabla\cdot(b_k\nabla b_2)-\nabla\cdot(a_k\nabla a_2)\right)-\frac{(k+2)N\pi}{cDe}\left(b_kb_2-a_ka_2\right)$$
$$-\frac{a\,(k+2)}{4}\left(2b_k\frac{\partial v_x}{\partial x}-a_k\left(\frac{\partial v_x}{\partial y}+\frac{\partial v_y}{\partial x}\right)\right).$$

In this instance, $A_k = B_k = C_k = D_k = E_k = F_k = G_k = H_k = I_k = J_k = 0$ if $k > K$.

Solving Navier-Stokes equation involve calculating the stress from active force, passive stress, and the interfacial force contributed by chemical potential. We first turn our attention to the stress tensors. The stress tensor from active force, τ_a is easily obtained by substituting (48) into (5).

$$\tau_a = \frac{\pi G \zeta_a}{2c} \begin{bmatrix} b_2 - 2b_0(c-1) & a_2 \\ a_2 & 2b_0(c-1) + b_2 \end{bmatrix}. \tag{72}$$

To compute the passive stress tensor, τ_p, we need to perform the contraction of the third-moment and the fourth-moment tensors

$$\begin{aligned} \langle \mathbf{mmm} \rangle \cdot \mathbf{n} &= \langle m_i m_j m_k \rangle \frac{\langle m_k \rangle}{c} \\ &= \frac{b_1 \pi^2}{4c} \begin{bmatrix} 3b_1 + b_3 & a_1 + a_3 \\ a_1 + a_3 & b_1 - b_3 \end{bmatrix} + \frac{a_1 \pi^2}{4c} \begin{bmatrix} a_1 + a_3 & b_1 - b_3 \\ b_1 - b_3 & 3a_1 - a_3 \end{bmatrix} \\ &= \frac{\pi^2}{4c} \begin{bmatrix} a_1^2 + a_3 a_1 + b_1 (3b_1 + b_3) & a_3 b_1 + a_1 (2b_1 - b_3) \\ a_3 b_1 + a_1 (2b_1 - b_3) & 3a_1^2 - a_3 a_1 + b_1 (b_1 - b_3) \end{bmatrix}, \end{aligned} \tag{73}$$

$$\begin{aligned} \langle \mathbf{mmmm} \rangle : \mathbf{D} &= \langle m_i m_j m_k m_l \rangle d_{kl} \\ &= \frac{d_{11}\pi}{16} \begin{bmatrix} 6b_0 + 4b_2 + b_4 & 2a_2 + a_4 \\ 2a_2 + a_4 & 2b_0 - b_4 \end{bmatrix} + \frac{d_{12}\pi}{8} \begin{bmatrix} 2a_2 + a_4 & 2b_0 - b_4 \\ 2b_0 - b_4 & 2a_2 - a_4 \end{bmatrix} \\ &\quad + \frac{d_{11}\pi}{16} \begin{bmatrix} b_4 - 2b_0 & a_4 - 2a_2 \\ a_4 - 2a_2 & 4b_2 - 6b_0 - b_4 \end{bmatrix} \\ &= \frac{\pi}{8} \begin{bmatrix} x_{11} & x_{12} \\ x_{12} & x_{22} \end{bmatrix}, \end{aligned} \tag{74}$$

where

$$\begin{aligned} x_{11} &= (2a_2 + a_4) d_{12} + (2b_0 + 2b_2 + b_4) d_{11}, \\ x_{12} &= a_4 d_{11} + (2b_0 - b_4) d_{12}, \end{aligned}$$

and

$$x_{22} = (a_4 - 2a_2) d_{12} + (2b_0 - 2b_2 + b_4) d_{11}.$$

Similarly,

$$\mathbf{M}:\langle \mathbf{mmmm}\rangle = \frac{\langle m_i m_j\rangle}{c}\langle m_i m_j m_k m_l\rangle = \frac{\pi^2}{8c}\begin{bmatrix} y_{11} & y_{12} \\ y_{12} & y_{22}\end{bmatrix}, \tag{75}$$

where

$$y_{11} = 2a_2^2 + a_4a_2 + 8b_0^2 + 2b_2^2 + 6b_0b_2 + b_2b_4,$$
$$y_{12} = a_4b_2 + a_2\left(6b_0 - b_4\right),$$

and

$$y_{22} = 2a_2^2 - a_4a_2 + 8b_0^2 + 2b_2^2 - 6b_0b_2 - b_2b_4.$$

With above results and (6), we now have

$$\tau_p = \begin{bmatrix} z_{11} & z_{12} \\ z_{12} & z_{22}\end{bmatrix}, \tag{76}$$

where

$$\begin{aligned} z_{11} =& \frac{\pi^2 G\left(2\alpha_0\left(a_1^2 + a_3a_1 + b_1\left(b_3 - b_1\right)\right) + 3a_2a_4N - 6b_0b_2N + 3b_2b_4N\right)}{24c^2} \\ &+ \frac{\pi\left(a_2d_{12} + \left(2b_0 + b_2\right)d_{11}\right)}{2cRe_2} + \frac{\pi\left(\left(2a_2 + a_4\right)d_{12} + \left(2b_0 + 2b_2 + b_4\right)d_{11}\right)}{8cRe_3} \\ &+ \frac{\pi\left(2b_0 + b_2\right)G}{2c} - \pi b_0G + \frac{d_{11}}{Re}, \\ z_{12} =& \frac{\pi\left(a_4d_{11} + \left(2b_0 - b_4\right)d_{12}\right)}{8cRe_3} + \frac{\pi b_0d_{12}}{cRe_2} + \frac{d_{12}}{Re} + \frac{\pi a_2G}{2c} \\ &- \frac{\pi^2G\left(2\alpha_0\left(a_1\left(2b_1 + b_3\right) - a_3b_1\right) - 3a_4b_2N + 3a_2\left(2b_0 + b_4\right)N\right)}{24c^2}, \end{aligned}$$

and

$$\begin{aligned} z_{22} =& \frac{\pi\left(a_2d_{12} + \left(b_2 - 2b_0\right)d_{11}\right)}{2cRe} - \frac{\pi\left(\left(a_4 - 2a_2\right)d_{12} + \left(2b_0 - 2b_2 + b_4\right)d_{11}\right)}{8cRe} \\ &- \frac{\pi^2G\left(2\alpha_0\left(a_1^2 + a_3a_1 + b_1\left(b_3 - b_1\right)\right) + 3a_2a_4n + 3b_2\left(b_4 - 2b_0\right)N\right)}{24c^2} \\ &+ \frac{\pi\left(2b_0 - b_2\right)G}{2c} - \pi b_0G - \frac{d_{11}}{Re}. \end{aligned}$$

Note to the reader here that d_{11} and d_{12} are already defined in (53).

We now consider the calculation of interfacial force term, $\langle \nabla \mu \rangle$. From (7) and (49), we have

$$
\begin{aligned}
(77) \qquad \langle \nabla \mu \rangle &= \int_0^{2\pi} f \nabla \mu \, d\varphi \\
&= \int_0^{2\pi} (\nabla f + f \nabla U) \, d\varphi \\
&= 2\pi \nabla b_0 + \langle \nabla U \rangle \\
&= \left(N_1 - \frac{N}{c} \right) 4\pi^2 b_0 \nabla b_0 - \frac{\gamma}{c} \pi^2 \left(b_1 \nabla b_1 + a_1 \nabla a_1 \right) \\
&\quad - \frac{N}{c} \pi^2 \left(b_2 \nabla b_2 + a_2 \nabla a_2 \right).
\end{aligned}
$$

4.2 SPATIAL DISCRETIZATION OF SMOLUCHOWSKI EQUATION

Consider the spatial domain for $x \in [0, X], y \in [0, Y]$. We subdivide the interval $[0, X]$ and $[0, Y]$ into N_x and N_y panels such that $0 \leq i \leq N_x, 0 \leq j \leq N_y$, and denote the length of the panels in x and y direction by h_x and h_y respectively. We approximate first partial derivative, second partial derivative, and mixed partial derivative, by using standard second-order finite difference method as follows:

$$
\left(\frac{\partial f}{\partial x} \right)_{i,j} = \frac{f_{i+1,j} - f_{i-1,j}}{2h_x},
$$

$$
\left(\frac{\partial f}{\partial x} \right)_{i,j} = \frac{f_{i+1,j} - f_{i-1,j}}{2h_y},
$$

$$
\left(\frac{\partial^2 f}{\partial x^2} \right)_{i,j} = \frac{f_{i+1,j} - 2f_{i,j} + f_{i-1,j}}{h_x^2},
$$

$$
\left(\frac{\partial^2 f}{\partial y^2} \right)_{i,j} = \frac{f_{i,j+1} - 2f_{i,j} + f_{i,j-1}}{h_y^2},
$$

$$
\left(\frac{\partial^2 f}{\partial x \partial y} \right)_{i,j} = \frac{f_{i+1,j+1} - f_{i+1,j-1} - f_{i-1,j+1} + f_{i-1,j-1}}{4h_x h_y}.
$$

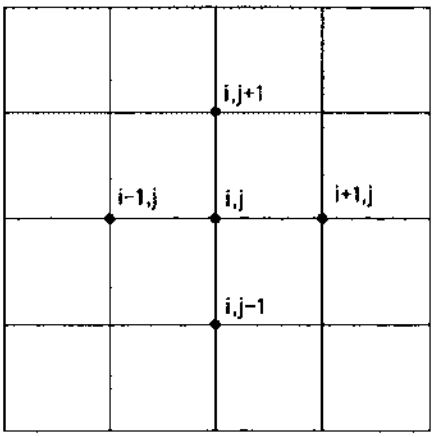

FIGURE 24: The spatial domain of number density function, $f(\mathbf{x}, \mathbf{m}, t)$

Also,

$$
\begin{aligned}
(\nabla \cdot (a \nabla b))_{i,j} &= \left(\frac{\partial}{\partial x} \left(a \frac{\partial b}{\partial x} \right) \right)_{i,j} + \left(\frac{\partial}{\partial y} \left(a \frac{\partial b}{\partial y} \right) \right)_{i,j} \\
&= \frac{\left(a \frac{\partial b}{\partial x} \right)_{i+\frac{1}{2},j} - \left(a \frac{\partial b}{\partial x} \right)_{i-\frac{1}{2},j}}{h_x} + \frac{\left(a \frac{\partial b}{\partial y} \right)_{i,j+\frac{1}{2}} - \left(a \frac{\partial b}{\partial y} \right)_{i,j-\frac{1}{2}}}{h_y} \\
&= \frac{1}{2h_x^2} \left((a_{i,j} + a_{i+1,j}) (b_{i+1,j} - b_{i,j}) - (a_{i-1,j} + a_{i,j}) (b_{i,j} - b_{i-1,j}) \right) \\
&\quad + \frac{1}{2h_y^2} \left((a_{i,j} + a_{i,j+1}) (b_{i,j+1} - b_{i,j}) - (a_{i,j-1} + a_{i,j}) (b_{i,j} - b_{i,j-1}) \right).
\end{aligned}
$$

4.3 TIME INTEGRATION OF SMOLUCHOWSKI EQUATION

Let n be the time step and recall that i, j are spatial indexes on the grid, we discretize the numerical values of $f(\mathbf{x}, \mathbf{m}, t)$ and $U(\mathbf{x}, \mathbf{m}, t)$ into n-th time step as $f_{i,j}^n(\mathbf{m})$ and $U_{i,j}^n(\mathbf{m})$ respectively. Hence, one can construct a linearly semi-implicit scheme

$$
\begin{aligned}
\frac{f_{i,j}^{n+1}(\mathbf{m}) - f_{i,j}^n(\mathbf{m})}{\Delta t} &= -\nabla \cdot \left(\left(\mathbf{v}^n + U_0 \left(\overline{\alpha} \mathbf{m} + \sqrt{1 - \overline{\alpha}^2} \mathbf{m}^{\perp} \right) \right) f_{i,j}^n(\mathbf{m}) \right) \\
&\quad + \nabla \cdot D_s^* \left(\nabla f_{i,j}^{n+1}(\mathbf{m}) + f_{i,j}^n(\mathbf{m}) \nabla U_{i,j}^n(\mathbf{m}) \right) \\
&\quad + \frac{1}{De} \mathcal{R} \cdot \left(\mathcal{R} f_{i,j}^{n+1}(\mathbf{m}) + f_{i,j}^n(\mathbf{m}) \mathcal{R} U_{i,j}^n(\mathbf{m}) \right)
\end{aligned} \tag{78}
$$

$$- \mathcal{R} \cdot \left(\mathbf{m} \times \dot{\mathbf{m}} f_{i,j}^{n} \left(\mathbf{m} \right) \right).$$

Omitting the spatial indexes, the scheme can be rewritten as

$$\begin{aligned} \left(\mathbf{I} - D_s^* \Delta t \nabla^2 - \frac{\Delta t}{De} \mathcal{R} \cdot \mathcal{R} \right) f^{n+1} = & - \Delta t \nabla \cdot \left(\left(\mathbf{v}^n + U_0 \left(\overline{\alpha} \mathbf{m} + \sqrt{1 - \overline{\alpha}^2} \mathbf{m}^{\perp} \right) \right) f^n \right) \\ & + D_s^* \Delta t \nabla \cdot \left(f^n \nabla U^n \right) + \frac{\Delta t}{De} \mathcal{R} \cdot \left(f^n \mathcal{R} U^n \right) \\ & - \mathcal{R} \cdot \left(\mathbf{m} \times \dot{\mathbf{m}} f^n \right) + f^n. \end{aligned} \tag{79}$$

Hence, the linearly semi-implicit equation can be written as a system of the inhomogeneous Helmholtz equations in the Fourier space, which are given by

$$\left(\nabla^2 - \frac{1}{D_s^* \Delta t} \mathbf{I} \right) b_0^{n+1} = - \frac{b_0^n}{D_s^* \Delta t} + \frac{1}{D_s^*} \left(F_2^n + G_1^n + H_0^n \right), \tag{80}$$

$$\left(\nabla^2 - \frac{De + \Delta t}{De D_s^* \Delta t} \mathbf{I} \right) b_1^{n+1} = - \frac{b_1^n}{D_s^* \Delta t} + \frac{1}{D_s^*} \left(F_3^n + F_1^n + G_2^n + G_0^n + H_1^n + I_0^n \right), \tag{81}$$

$$\left(\nabla^2 - \frac{De + 4\Delta t}{De D_s^* \Delta t} \mathbf{I} \right) b_2^{n+1} = - \frac{b_2^n}{D_s^* \Delta t} + \frac{1}{D_s^*} \left(F_4^n + F_0^n + G_3^n + H_2^n + I_1^n + J_0^n \right), \tag{82}$$

$$\left(\nabla^2 - \frac{De + k^2 \Delta t}{De D_s^* \Delta t} \mathbf{I} \right) b_k^{n+1} = - \frac{b_k^n}{D_s^* \Delta t} + \frac{1}{D_s^*} \left(F_{k+2}^n + G_{k+1}^n + H_k^n + I_{k-1}^n + J_{k-2}^n \right), \quad 3 \leq k \leq K, \tag{83}$$

$$\left(\nabla^2 - \frac{De + \Delta t}{De D_s^* \Delta t} \mathbf{I} \right) a_1^{n+1} = - \frac{a_1^n}{D_s^* \Delta t} + \frac{1}{D_s^*} \left(A_3^n - A_1^n + B_2^n - B_0^n + C_1^n + D_0^n \right), \tag{84}$$

$$\left(\nabla^2 - \frac{De + 4\Delta t}{De D_s^* \Delta t} \mathbf{I} \right) a_2^{n+1} = - \frac{a_2^n}{D_s^* \Delta t} + \frac{1}{D_s^*} \left(A_4^n - A_0^n + B_3^n + C_2^n + D_1^n + E_0^n \right), \tag{85}$$

$$\left(\nabla^2 - \frac{De + k^2 \Delta t}{De D_s^* \Delta t} \mathbf{I} \right) a_k^{n+1} = - \frac{a_k^n}{D_s^* \Delta t} + \frac{1}{D_s^*} \left(A_{k+2}^n + B_{k+1}^n + C_k^n + D_{k-1}^n + E_{k-2}^n \right), \quad 3 \leq k \leq K. \tag{86}$$

4.4 SPATIAL DISCRETIZATION OF NAVIER-STOKES EQUATIONS

The problem with standard grid when solving Navier-Stokes equations is that we could get artificial pressure oscillations. This oscillation problem is generally described in textbooks (e.g. [**20, 41**]) about numerical solution of differential equation.

To avoid such problem, we use a staggered grid, in which the different variables are not located at the same grid points. In 2D, the staggered grid we shall use has three subgrids, one for the pressure p, one for the horizontal velocity u and one for the vertical velocity v. As a result, the location of the discrete value of u, v and p are shifted by half a grid in the direction relative to the other subgrid as shown in Figure 25.

We now look at the Navier-Stokes equation in (2). Let $\tilde{\tau}_p = \tau_p - \frac{2}{Re}\mathbf{D}$. Then, we have

$$\begin{aligned}\frac{d\mathbf{v}}{dt} =& \nabla \cdot (-p\mathbf{I} + \tau_p + \tau_a) - \langle \nabla \mu \rangle \\ =& -\nabla \cdot p\mathbf{I} + \nabla \cdot \left(\frac{2}{Re}\mathbf{D} + \tilde{\tau}_p + \tau_a \right) - \langle \nabla \mu \rangle \\ =& -\nabla p + \frac{1}{Re}\Delta \mathbf{v} + \nabla \cdot (\tilde{\tau}_p + \tau_a) - \langle \nabla \mu \rangle .\end{aligned}$$

Thus, the Navier-Stokes equation that we need to solve is

$$\frac{\partial \mathbf{v}}{\partial t} + \mathbf{v} \cdot \nabla \mathbf{v} = -\nabla p + \frac{1}{Re}\Delta \mathbf{v} + \nabla \cdot (\tilde{\tau}_p + \tau_a) - \langle \nabla \mu \rangle . \tag{87}$$

Notice that spatial discretization of the convective term does not fit into the staggered grid scheme if we use the standard central differences to approximate the derivatives. This is because p, u, and v are not in the same location. Therefore it is convenience to rewrite the expression as [**14**]

$$u\frac{\partial u}{\partial x} + v\frac{\partial u}{\partial y} = \frac{\partial (u^2)}{\partial x} + \frac{\partial (uv)}{\partial y} \tag{88}$$

and

$$u\frac{\partial v}{\partial x} + v\frac{\partial v}{\partial y} = \frac{\partial (v^2)}{\partial y} + \frac{\partial (uv)}{\partial x}. \tag{89}$$

The discretizations are given by the following expressions [**14**]. For u at the midpoint of the right edge of cell (i, j), we use

$$\frac{\partial (u^2)}{\partial x} = \frac{1}{h_x}\left(\left(\frac{u_{i,j} + u_{i+1,j}}{2} \right)^2 - \left(\frac{u_{i-1,j} - u_{i,j}}{2} \right)^2 \right)$$

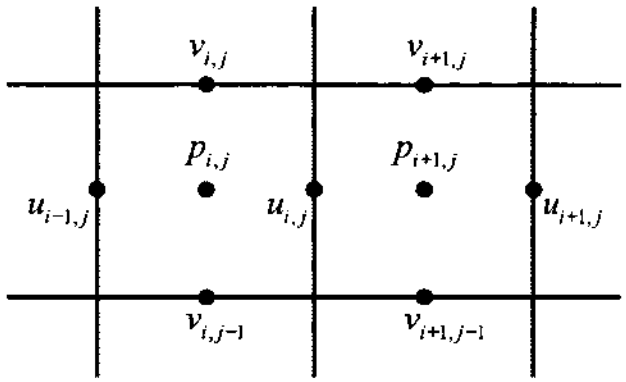

FIGURE 25: Staggered grid.

$$
\begin{aligned}
&+\gamma_s \frac{1}{h_x}\left(\frac{|u_{i,j}+u_{i+1,j}|}{2}\frac{(u_{i,j}-u_{i+1,j})}{2}-\frac{|u_{i-1,j}+u_{i,j}|}{2}\frac{(u_{i-1,j}-u_{i,j})}{2}\right),\\
\frac{\partial(uv)}{\partial y}=&\frac{1}{h_y}\left(\frac{(v_{i,j}+v_{i+1,j})}{2}\frac{(u_{i,j}+u_{i,j+1})}{2}-\frac{(v_{i,j-1}+v_{i+1,j-1})}{2}\frac{(u_{i,j-1}+u_{i,j})}{2}\right)\\
&+\gamma_s \frac{1}{h_y}\left(\frac{|v_{i,j}+v_{i+1,j}|}{2}\frac{(u_{i,j}-u_{i,j+1})}{2}-\frac{|v_{i,j-1}+v_{i+1,j-1}|}{2}\frac{(u_{i,j-1}+u_{i,j})}{2}\right),\\
\frac{\partial^2 u}{\partial x^2}=&\frac{u_{i+1,j}-2u_{i,j}+u_{i-1,j}}{h_x^2},\qquad \frac{\partial^2 u}{\partial y^2}=\frac{u_{i,j+1}-2u_{i,j}+u_{i,j-1}}{h_y^2},\\
\frac{\partial p}{\partial x}=&\frac{p_{i+1,j}-p_{i,j}}{h_x}.
\end{aligned}
$$

For v at the mid point of the upper edge of cell (i,j), we use

$$
\begin{aligned}
\frac{\partial(uv)}{\partial x}=&\frac{1}{h_x}\left(\frac{(u_{i,j}+u_{i,j+1})}{2}\frac{(v_{i,j}+u_{i+1,j})}{2}-\frac{(u_{i-1,j}+u_{i-1,j+1})}{2}\frac{(v_{i-1,j}+v_{i,j})}{2}\right)\\
&+\gamma_s \frac{1}{h_x}\left(\frac{|u_{i,j}+u_{i,j+1}|}{2}\frac{(v_{i,j}-v_{i+1,j})}{2}-\frac{|u_{i-1,j}+u_{i-1,j+1}|}{2}\frac{(v_{i-1,j}+v_{i,j})}{2}\right),\\
\frac{\partial(v^2)}{\partial y}=&\frac{1}{h_y}\left(\left(\frac{v_{i,j}+v_{i,j+1}}{2}\right)^2-\left(\frac{v_{i,j-1}-v_{i,j}}{2}\right)^2\right)\\
&+\gamma_s \frac{1}{h_x}\left(\frac{|v_{i,j}+v_{i,j+1}|}{2}\frac{(v_{i,j}-v_{i,j+1})}{2}-\frac{|v_{i,j-1}+v_{i,j}|}{2}\frac{(v_{i,j-1}-v_{i,j})}{2}\right),\\
\frac{\partial^2 v}{\partial x^2}=&\frac{v_{i+1,j}-2v_{i,j}+v_{i-1,j}}{h_x^2},\qquad \frac{\partial^2 v}{\partial y^2}=\frac{v_{i,j+1}-2v_{i,j}+v_{i,j-1}}{h_y^2},\\
\frac{\partial p}{\partial y}=&\frac{p_{i,j+1}-p_{i,j}}{h_y}.
\end{aligned}
$$

Notice that there are the stability terms introduced in the numerical scheme with the stability parameter γ_s. According to the paper by Hirt et al. [18], the stability

parameter for the discretization of the convective terms is chosen such that

$$1.1 \max_{i,j} \left(\left| \frac{u_{i,j}\Delta t}{\Delta x} \right|, \left| \frac{v_{i,j}\Delta t}{\Delta y} \right| \right) \leq \gamma_s < 1 \tag{90}$$

is satisfied.

4.5 TIME INTEGRATION OF NAVIER-STOKES EQUATIONS

To ensure that the divergence of the velocity vanishes in every time step, we use the projection method [1] for numerical treatment of the Navier-Stokes equations. In the projection method, we start calculation by solving the intermediate velocity, $\mathbf{v}^*$, by

$$\frac{\mathbf{v}^* - \mathbf{v}^n}{\Delta t} + \mathbf{v}^n \cdot \nabla \mathbf{v}^n = \frac{1}{Re} \Delta \mathbf{v}^n + \nabla \cdot (\tilde{\tau_e} + \tau_a) - \langle \nabla \mu \rangle \,. \tag{91}$$

Next, we solve the pressure Poisson equation

$$\Delta p^{n+1} = \frac{\nabla \cdot \mathbf{v}^*}{\Delta t}. \tag{92}$$

Finally, the velocity is calculated by

$$\mathbf{v}^{n+1} = \mathbf{v}^* - \Delta t \nabla p^{n+1}. \tag{93}$$

The time step size Δt is chosen such that the condition by Tome and McKee [**38**] and the Courant-Friedrichs-Lewy (CFL) condition [**2**] are satisfied. Hence, an adaptive time step size control is given by

$$\Delta t \leq 0.9 \min \left(\frac{Re}{2} \left(\frac{1}{\Delta x^2} + \frac{1}{\Delta y^2} \right)^{-1}, \frac{\Delta x}{|u_{\max}|}, \frac{\Delta y}{|v_{\max}|} \right), \tag{94}$$

where $|u_{\max}|$ and $|v_{\max}|$ are the maximal absulute values of the horizontal and vertical velocity occurring on the grid.

4.6 SIMULATION RESULTS

In this section, we investigate long-time evolution of instability and pattern formation of inhomogeneous suspensions. Here, initially perturbed isotropic suspension is given by

$$f(\mathbf{x}, \mathbf{m}, t) = \frac{1}{2\pi} + \sum_{k=1}^{K} (\varepsilon_k(x, y) \cos(k\varphi) + \delta_k(x, y) \sin(k\varphi)), \tag{95}$$

where $\varepsilon_k(x,y)$ and $\delta_k(x,y)$ are small random coefficient chosen in the interval $[-0.001, 0.001]$. The boundary conditions of all configurations of the suspensions are assumed to be periodic. More reasonable boundary condition will be considered in the the future work.

The simulations for pullers ($\zeta_a > 0$) and passive particles ($\zeta_a = 0$) were performed but did not show any instability (i.e. the flows $\mathbf{v}$ quickly dissipate and the system converges back to uniform isotropic state, $f = \frac{1}{2\pi}$, after perturbation). This is consistent with the results in [**12, 30, 31**]. Therefore, all results shown in this section are only for the suspension of pusher ($\zeta_a < 0$). The numerical algorithm is implemented in C++, with the help from FORTRAN module [**37**] for solving Helmholtz equations. Note that, during the simulation, we truncate Fourier approximation in (41) at $K = 20$, which corresponds to 41 partial differential equations, since increasing K shows little improvement. All numerical simulations are conducted on the Zorka system at Old Dominion University with 40 compute nodes (two dual core 2.99 GHz Intel Xeon, 8GB RAM).

The simulations are extensively conducted in square and rectangle domains by varying various parameters, mainly the nematic strength, N, the Deborah number, De, the transnational diffusion coefficient, D_s^*, and the active parameter, ζ_a. We find that not every pusher, $\zeta_a < 0$, gives the interesting results. For small values of $|\zeta_a|$, the perturbed system relaxes to uniform isotropic state, just like the case of pullers or passive particles. The existence of threshold of ζ_a is also reported in other literature [**11, 12**]. We present various spatio-temperal structures observed from the simulations in the view of velocity field, $\mathbf{v}$, local concentration, $\mathcal{C} = \langle 1 \rangle = 2\pi b_0$, mean director field (polarization direction describing polar state), $\mathbf{p} = \langle \mathbf{m} \rangle$, nematic orientation (major director describing nematic state), $\mathbf{n_1}$, and degree of alignment, s, as described in previous sections. While in the nematic state, the major director, $\mathbf{n_1}$, is a head-tail symmetric vector since $\mathbf{n_1}$ and $-\mathbf{n_1}$ carry the same angle of orientation. However, $\mathbf{p}$ is still a true vector since the polar state does not posses this symmetry.

4.6.1 SQUARE DOMAIN

We first perform various numerical simulations in a square domain. Below are the four major patterns that we discover.

Parameter	Value
N	1
a	1
De	15
$N1$	3
$U0$	1
D_s^*	0.02
γ	1
c	1
G	1
α_0	1
Re	10
Re_2	10
Re_3	10
ζ_a	-4
$\overline{\alpha}$	1

TABLE 6: Parameter values used to obtain numerical results in Figure 26.

Periodic state

For a majority of numerical simulations we performed in unit square domain, time-periodic structures of suspensions are observed. An example can be obtained by conducting the simulation using the parameters listed in Table 6. Figure 26 presents snapshots, at long times, of the velocity field superimposed to the density plot of the local concentration, C, (left column) polarization direction, $\mathbf{p}$, superimposed to the density plot of its magnitude, $|\mathbf{p}|$, (middle column) and nematic orientation superimposed to the density plot of the degree of alignment, s, (right column). The color bar displayed at the bottom of each column corresponds to the gauge of, from left to right columns, C, $|\mathbf{p}|$, and s. We can see in all figures of the velocity field and polarization direction that there are four quadrants in the domain with two circles and two hyperbolic points. At the circles, the local concentration takes the minimum value (see the figure in the left column, second row) and the degree of alignment is weak (see the figure in the right column, second row), while at the hyperbolic points, the concentration takes the maximum value and the degree of alignment is strong. Yet, the polarity field is weak at both circles and hyperbolic points, it is at its peak value in the middle of the transition from one circle to another (see the figure in the middle column, second row). Now, we discuss various features of the periodic structure of the suspension.

First, the reversal of velocity and polarization director: We can easily see flows and polarity reversal by looking at Figure 26 and comparing the direction of flows (left column) and polarity (middle column) at different times. Some detailed examples of these phenomena are presented in Figure 27 showing the cross-sectional data by the plot, at two different times, of the polarization angle, ϕ, as a function of y with fixed $x = \frac{1}{2}$ (left figure), and the cross-sectional data by the plot, at two different times, of the polarization angle, ϕ, as a function of x with fixed $y = \frac{1}{2}$ (right figure). The solid and dashed line represent the polarity angle at time $t = 198.6$ and $t = 199.8$, respectively. Both figures clearly show the switching between upward and downward of the polarity angle. In Figure 27 (left), at $t = 198.6$, the the polarization direction points downward ($-180° < \phi < 0°$) while at $t = 199.8$ the polarity points upward ($0° < \phi < 180°$). The switching between left ($90° < \phi < 180°$ or $-180° < \phi < -90°$) and right ($-90° < \phi < 90°$) direction is also shown in Figure 27 (right).

Second, the 90° rotations of nematic orientation in nearby monodomains, thus causing defects. Figure 29 presents the contour plots of the angle of nematic orientation, ψ, at two different times. One can easily see that both contour planes are characterized by two regimes with distinct nematic orientation angle $\psi \approx 45°$ and $\psi \approx -45°$, respectively. These two regimes keep switching back and forth though times resulted in the rotation of 90° of the major director. This defect structure can also be seen from the order parameter s. At the boundary between any two regimes with orthogonal nematic orientations, the order parameter is nearly zero (see Figure 28).

Third, the fluctuations of scalar quantities such as the local concentration, the magnitude of polarity, and the degree of alignment: Figure 30 shows the three dimensional plot of the local concentration, $\mathcal{C}$, at different times resulting in grouping and breaking up of the molecules as time evolves. The time-periodicity has been confirmed in Figure 33, which shows the time evolution, with the period ≈ 2.2, of the magnitude of different spatial Fourier modes of the local concentration field given by

$$F_{k,\ell} = \frac{1}{MN} \sum_{m=0}^{M-1} \sum_{n=0}^{N-1} \mathcal{C}_{m,n} e^{-j2\pi\left(k\frac{m}{M} + \ell\frac{n}{N}\right)}. \tag{96}$$

Here, we can see that the spectrum of Fourier decomposition is completely dominated by low-wavenumber modes since high-wavenumber modes appear to decay to zero at long times. The periodic behaviors can also be seen in Figure 31 showing the

complete velocity orbit. The figure is obtained by, as time evolves, collecting the velocity at particular spatial location ($(x, y) = \left(\frac{1}{2}, \frac{1}{2}\right)$), then plot the phase portrait by showing the horizontal, v_x, and vertical, v_y, components of the velocity on the plane.

One can see in the left and the middle column of Figure 26 that the velocity and the polarization direction seem to be correlated. This is described more precisely in Figure 32 , showing the spatially averaged correlation between particle polarity and fluid velocity fields along the simulation time. We represent the macroscopic correlation by $\langle \cos \theta (\mathbf{v}, \mathbf{p}) \rangle$, where $\theta (\mathbf{v}, \mathbf{p})$ is the angle between the velocity and polarization direction. It is clearly seen in the figure that most of the time in the period, the polarity director positively correlates with the flow (indicated by the value 1 of the cosine angle between these two fields). The negative correlation (indicated by the value -1 of the cosine angle) occurs when the flow is weak and the polar director goes against the flow direction.

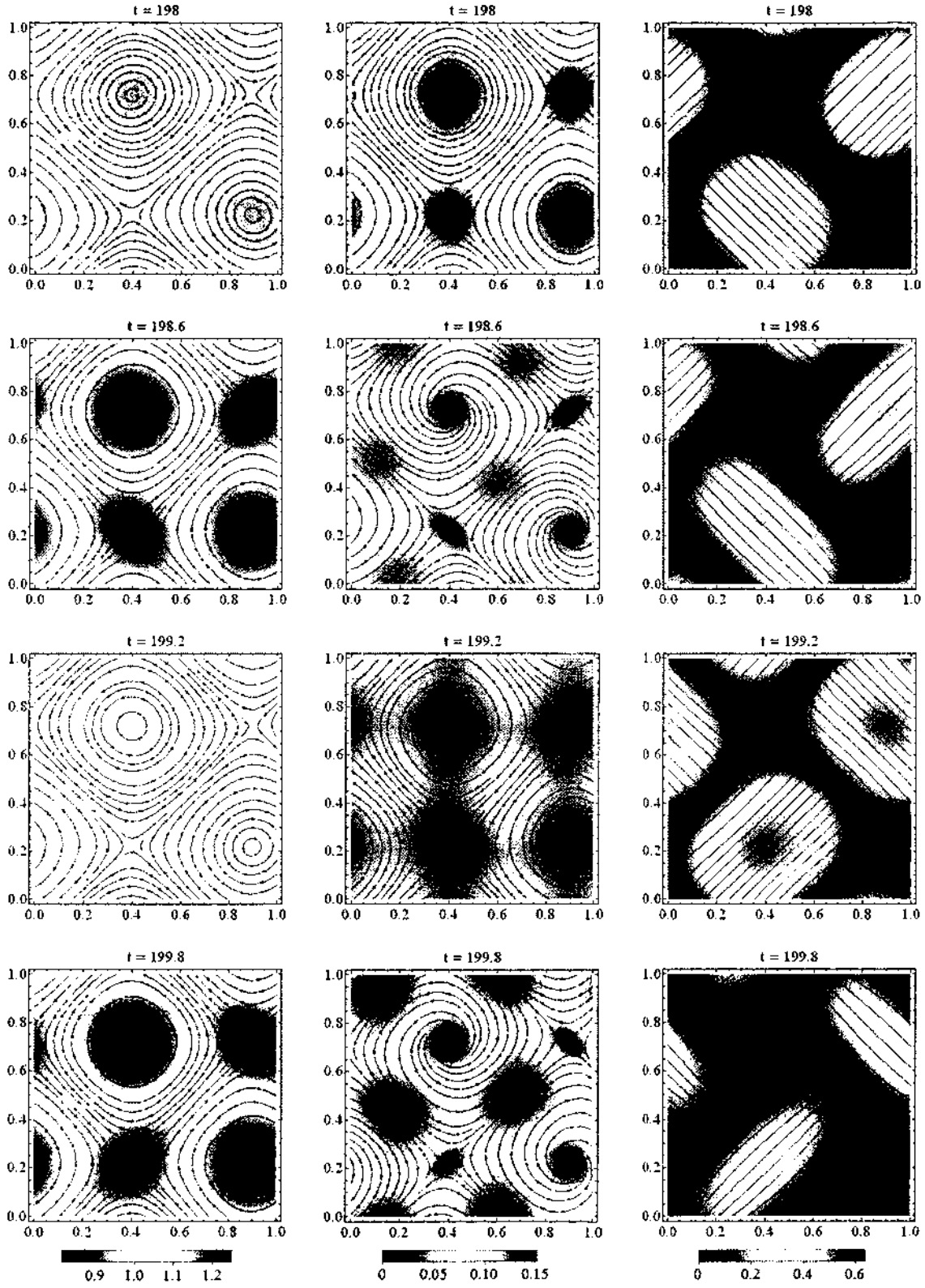

FIGURE 26: Snapshots, at long times, of (left column) the velocity filed $\mathbf{v}$ superimposed to local concentration, $\mathcal{C}$, (middle column) the mean director field, $\mathbf{p}$, superimposed to the density plot of $|\mathbf{p}|$, and (right column) the nematic orientation superimposed to the density plot of the degree of alignment, s.

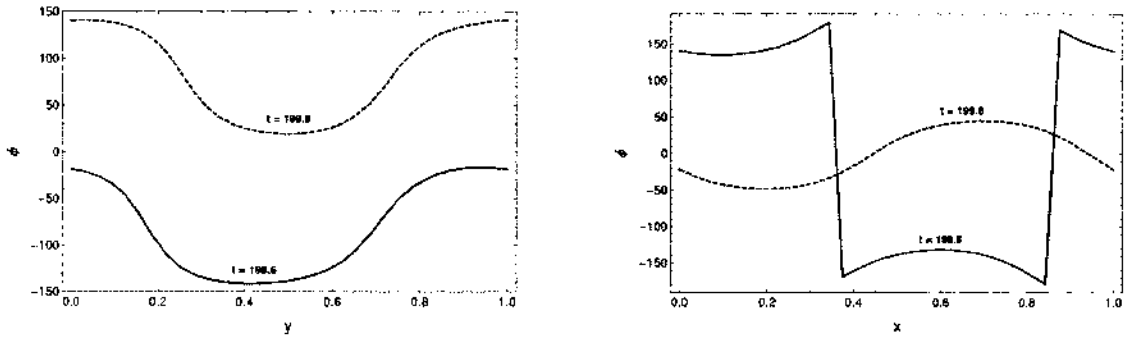

FIGURE 27: The cross-sectional data, at two different times, of the polarization angle, ϕ, as a function of y where $x = \frac{1}{2}$ (left), and the cross-sectional data, at two different times, of the polarization angle, ϕ, as a function of x where $y = \frac{1}{2}$ (right). The solid and dashed lines represent two different times.

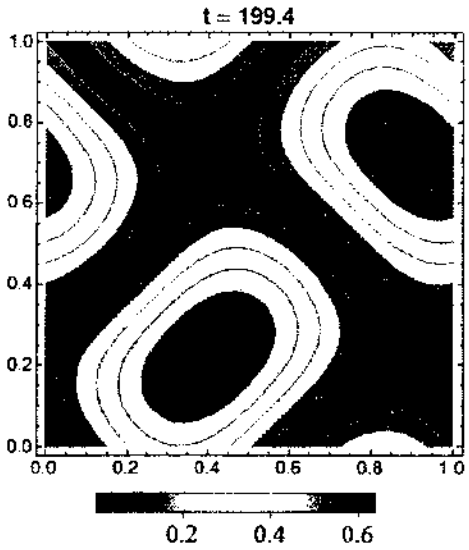

FIGURE 28: The contour plot of the degree of alignment, s, at $t = 199.4$. The blue area, $s \approx 0$, represents defect structure.

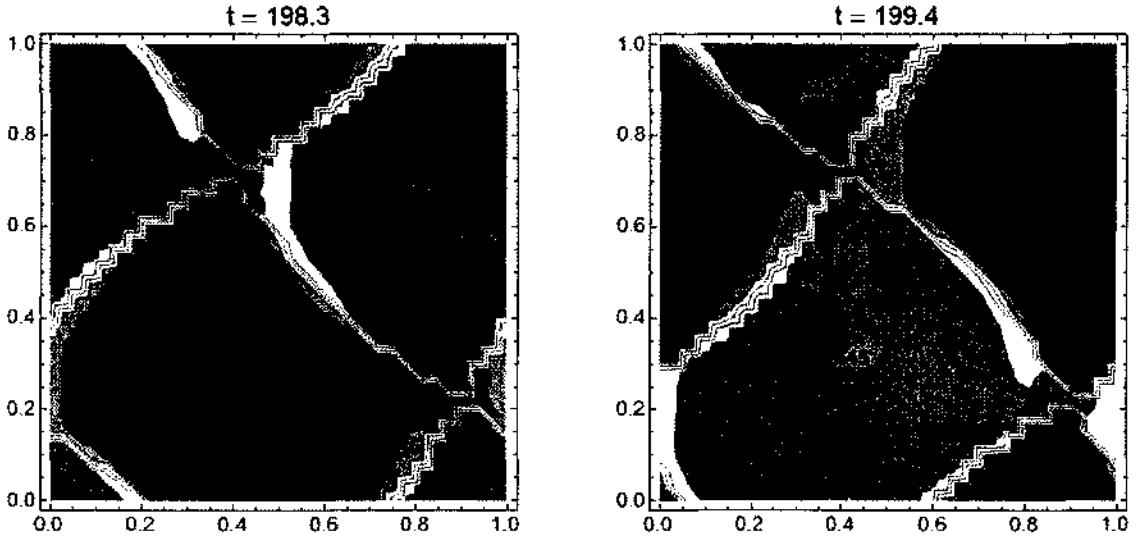

FIGURE 29: The contour plot of nematic orientation angle, ψ, in Figure 26, at two different times in the period.

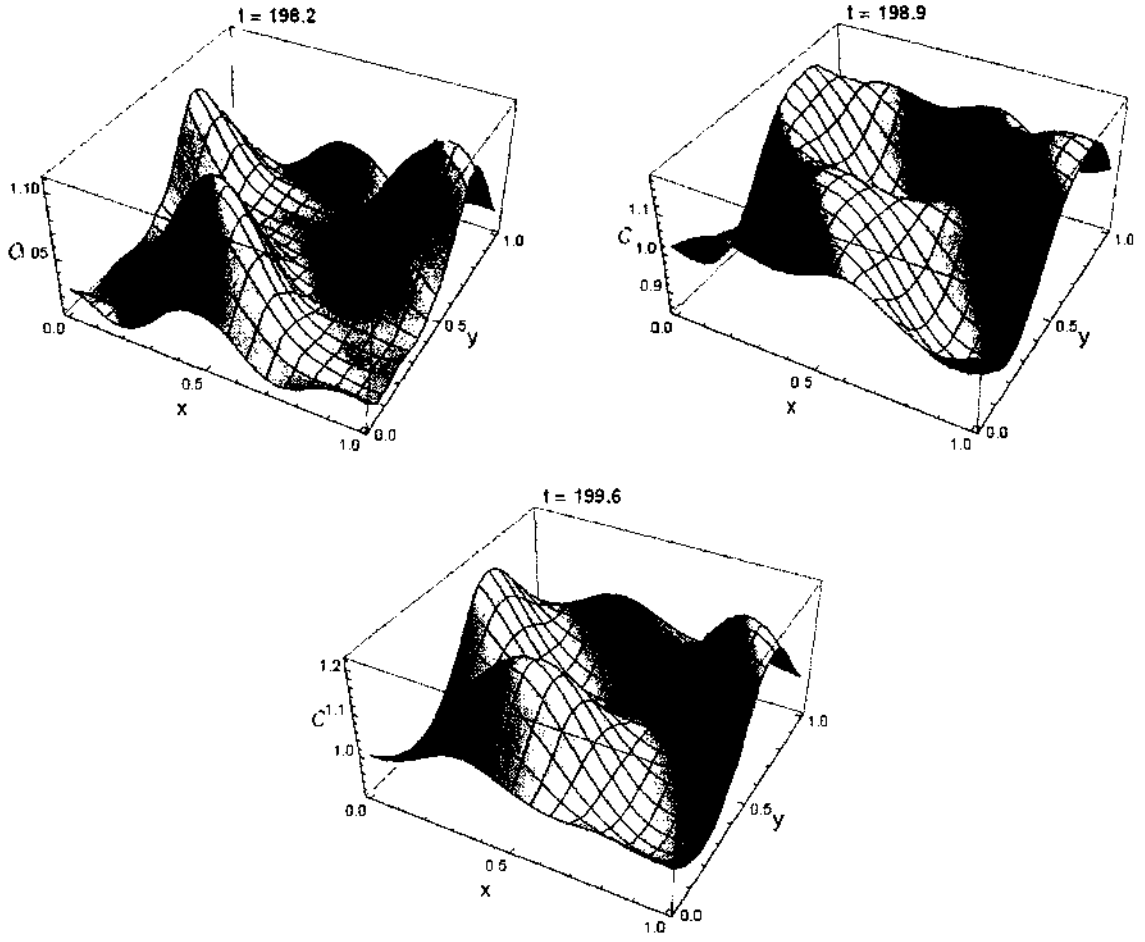

FIGURE 30: The three dimensional plot showing the fluctuation of the local concentration in, C, Figure 26, at different times.

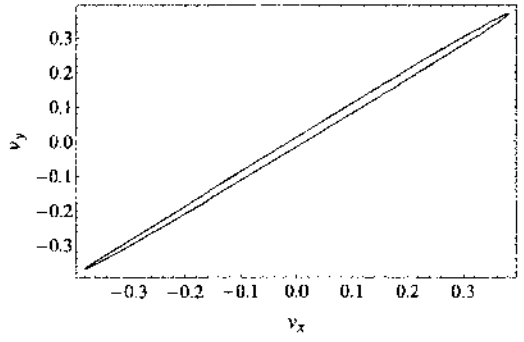

FIGURE 31: The velocity orbit at location $(x, y) = \left(\frac{1}{2}, \frac{1}{2}\right)$.

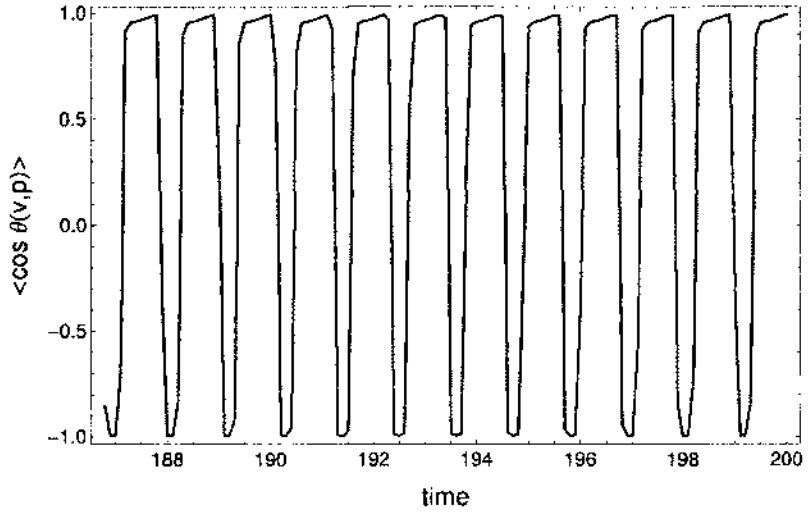

FIGURE 32: Spatially averaged correlation between the velocity , $\mathbf{v}$, and polarization direction, $\mathbf{p}$.

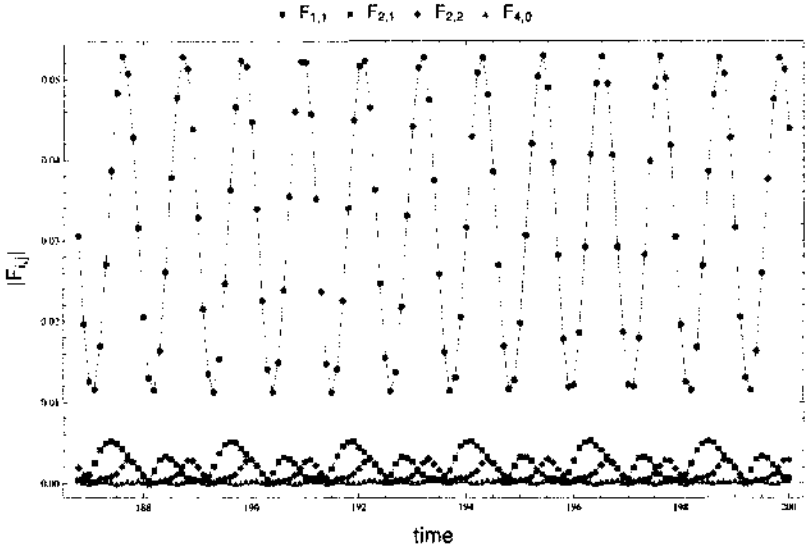

FIGURE 33: Time evolution of the magnitude of various spatial Fourier modes of the local concentration field, C.

Steady state

Figure 34 shows the results based on the assumption that the effect of swimming activity of pusher is high, i.e. we further increase the magnitude of ζ_a to 15. All parameters chosen for this simulation are shown in Table 7. In this case, the simulation converges to a steady attractor which is clearly illustrated by Figure 35 showing the time evolution of horizontal and vertical components of the velocity at specific point $(x, y) = (\frac{1}{2}, \frac{1}{2})$, and Figure 36 showing time series of the magnitude of some spatial Fourier modes. We again observe that the low-wavenumber modes still dominate the spectrum of Fourier decomposition. Figure 34 shows the final steady state of velocity, local concentration, polarity, and nematic patterns in the same manner as that of the row in Figure 26. It is revealed that, at steady state, the velocity field possesses two-dimensional structure similar to previous case which consists of two circles and two hyperbolic points. The local concentration is high at the hyperbolic points and also at the transition region between two circles. However, we clearly see in Figure 34 that there is a strong correlation between the velocity and the nematic orientation. This is different from previous case in which velocity and polarity are strongly correlated. Figure 37 represents the macroscopic correlations between the velocity field, $\mathbf{v}$, polarization direction, $\mathbf{p}$, and nematic orientation, $\mathbf{n_1}$. While the velocity-nematic orientation correlation is strongly positive as expected, we surprisingly observe the negative correlation (≈ -0.15) between velocity and polarization direction, i.e., on average, the particle does not swim with the flow. This phenomenon is emphasized by Figure 38 showing the contour plot of the velocity-polarity correlation of entire domain. It can be seen in the figure that the local correlations are mostly zero or negative. This result is , however, counter intuitive since the polarity should be positively correlated with the fluid flow. Whether this feature is caused by high swimming activity of the particles ($\zeta_a = -15$) will be investigated in future study.

Parameter	Value
N	1
a	1
De	50
$N1$	3
$U0$	1
D_s^*	0.5
γ	1
c	1
G	1
α_0	1
Re	10
Re_2	10
Re_3	10
ζ_a	-15
$\bar{\alpha}$	1

TABLE 7: Parameter values used to obtain the results in Figure 34.

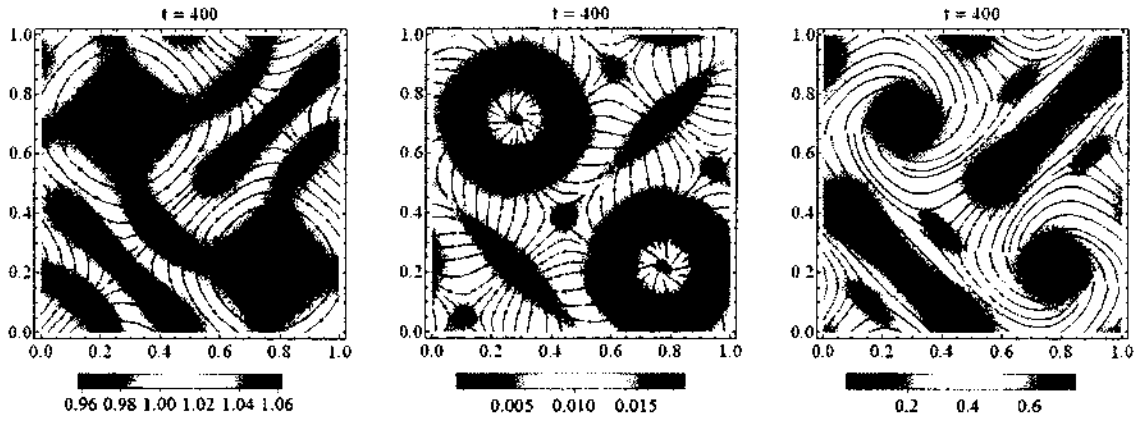

FIGURE 34: Final steady state of the numerical simulation. Left: the velocity filed $\mathbf{v}$ superimposed to the density plot of local concentration, C. Middle: the mean director field, $\mathbf{p}$, superimposed to the density plot of $|\mathbf{p}|$. Right: the nematic orientation superimposed to the density plot of the degree of alignment, s.

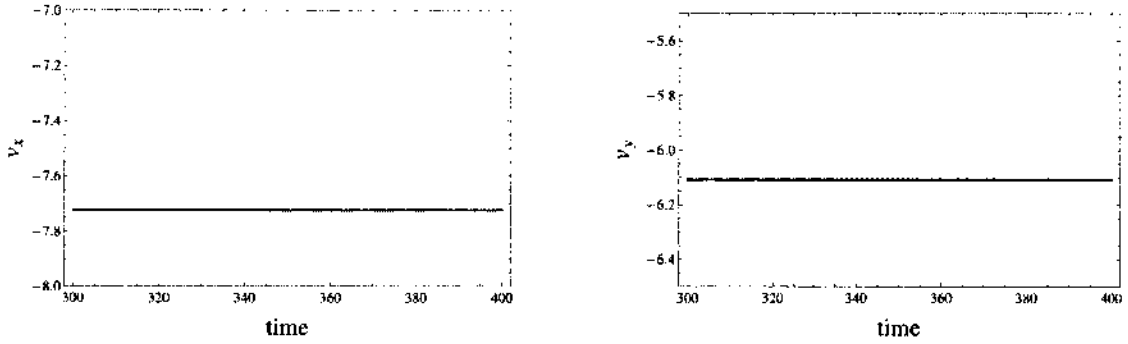

FIGURE 35: Horizontal,v_x, and vertical, v_y, components of the velocity as a function of time at the location $(x, y) = (\frac{1}{2}, \frac{1}{2})$.

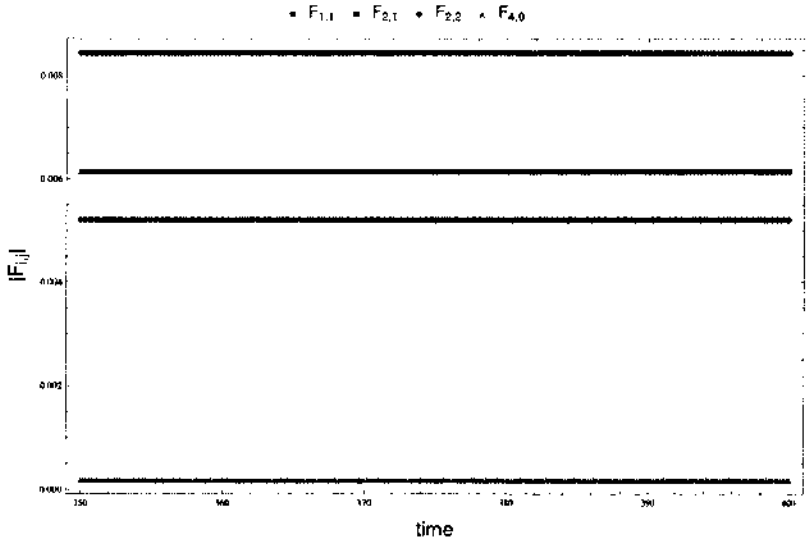

FIGURE 36: Time evolution of the magnitude of various spatial Fourier modes of the local concentration field, $\mathcal{C}$.

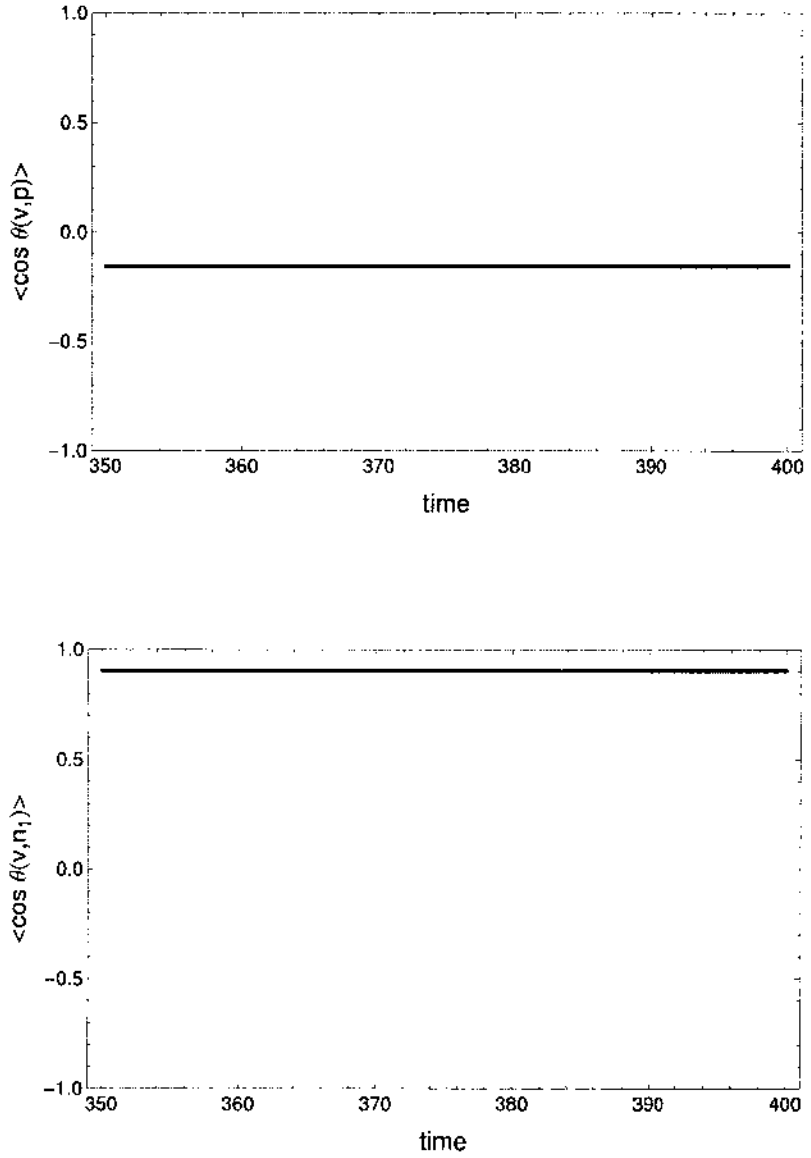

FIGURE 37: The correlations between the velocity field, $\mathbf{v}$, polarization direction, $\mathbf{p}$, and nematic orientation, $\mathbf{n_1}$. Top: Spatially averaged correlation between the velocity and polarization direction. Bottom: Spatially averaged correlation between the velocity and nematic orientation.

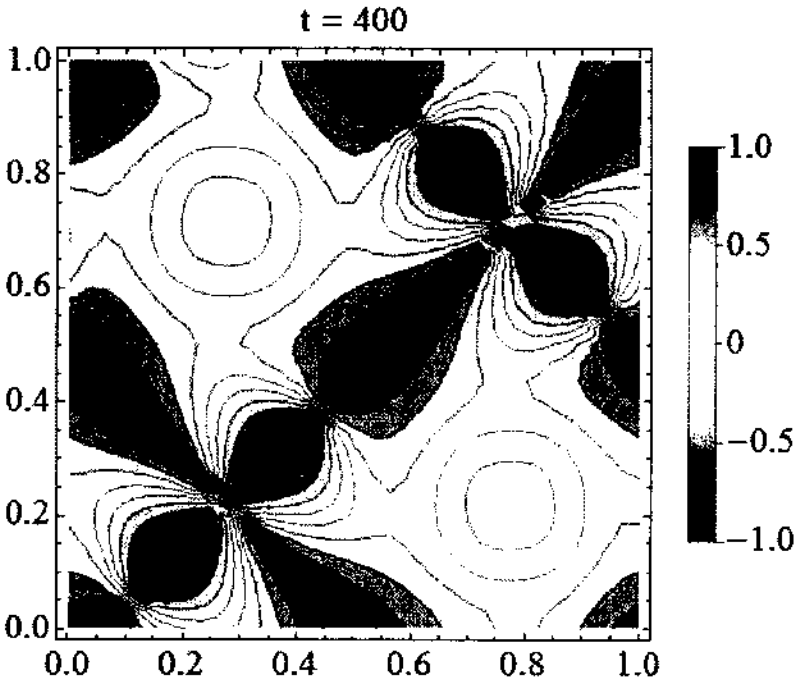

FIGURE 38: The contour plot of the correlation between the velocity field, $\mathbf{v}$, and the polarization direction, $\mathbf{p}$.

Parameter	Value
N	1
a	1
De	15
$N1$	3
$U0$	1
D_s^*	0.04
γ	1
c	1
G	1
α_0	1
Re	10
Re_2	10
Re_3	10
ζ_a	-7
$\overline{\alpha}$	1

TABLE 8: Parameter values used to obtain the suspension structures in Figure 41-43.

Irregular state with intermittent quasiperiodic patterns

Another interesting result of the simulation of inhomogeneous suspension in a unit square domain is that the system undergoes a transition of an irregular regime which consists of different quasiperiodic fluctuations in different time intervals. We illustrate this phenomenon by the simulation using parameter values in Table 8. Figure 39 shows the plot of horizontal and vertical components of the velocity as a function of time. It can be seen that we have four different quasiperiordic regions characterized by time interval $200 < t < 255$, $255 < t < 290$, $290 < t < 350$, and $350 < t < 400$, respectively. We then confirm the quasiperiordic fluctuation for each time interval by spectrum analysis. For example, on the left of Figure 40 is the example of the plot of magnitude of the Fourier modes against corresponding frequencies of v_x at $x = y = \frac{1}{2}$ in the time interval $350 < t < 400$ while similar plot for v_y is shown on the right. As one might anticipate, both v_x and v_y signals have many dominant long-wave frequency components.

We investigate the configurations of active suspension during each time interval and find that they posses the similar patterns. Here, we present only the results for $350 < t < 400$. Since the interesting features of all configurations appear at different times, we decide to present each of them separately rather than combine them as previously done. Figure 41 shows snapshots of long-time behavior of fluid velocity , $\mathbf{v}$,

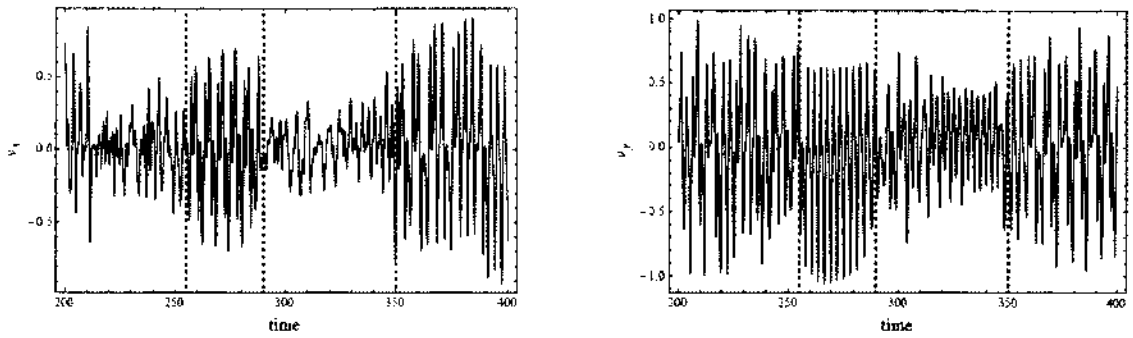

FIGURE 39: The plot of velocity as a function of time during quasiperiodic state at the center of simulation domain, $x = y = \frac{1}{2}$, separated by four quasiperiodic region. Left: the plot of the horizontal component,v_x. Right: the plot of the vertical component, v_y.

superimposed to the density plot of the local concentration, $\mathcal{C}$. We observe flow reversal and position switching between spinning vertices, where the local concentration is low, and saddle points, where the local concentration is high. Figure 42 presents the stream plot, at four different times, of polarization direction , $\mathbf{p}$, superimposed to the density plot of $|\mathbf{p}|$. One can see that the regions of polarization direction are typically in the form of vertical (top left) and horizontal (bottom left) banded structures. As these bands get denser, they become unstable and fold themselves into spiral patterns (right column). After that, they break up and reconstruct as new bands in the perpendicular direction to the previous ones. The behavior of namatic alignment can be seen in Figure 43 showing snapshots of nematic orientation, $\mathbf{n_1}$, superimposed to the density plot of the degree of alignment, s. The namatic alignment exhibits the switching between horizontal and vertical layers. These dynamics underlay the irregular periodicity of the spatial Fourier modes of the local concentration (Figure 44). Similar to the case of perfect periodic pattern, the macroscopic correlation between fluid velocity and polarity is mostly positive as shown in Figure 45. As one might anticipated, the correlation plunges into the negative region for a short time at the flow reversal where the velocity is low. The quasiperiodic pattern of active suspension is also reported in [**30**].

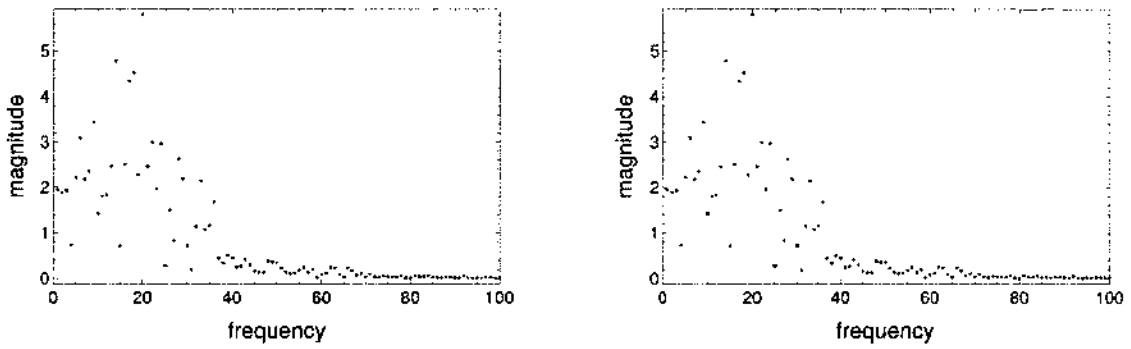

FIGURE 40: The magnitude of discrete Fourier transform spectrum of the time series of horizontal component ,v_x (left), and vertical component, v_y (right), of the velocity at the center of simulation domain $(x, y) = (\frac{1}{2}, \frac{1}{2})$ during the time interval $350 < t < 400$.

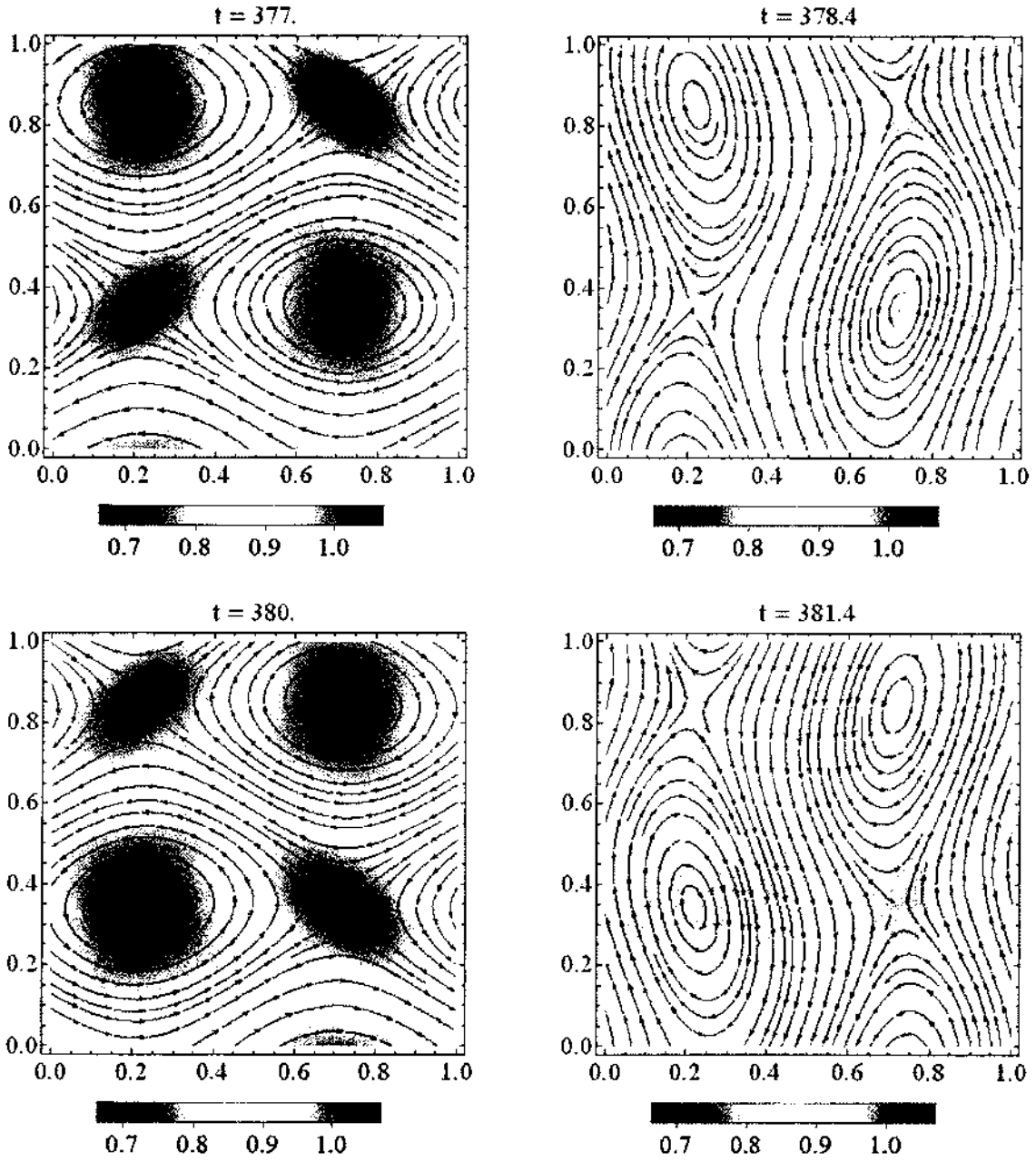

FIGURE 41: Snapshots of long time behavior of fluid velocity , $\mathbf{v}$, superimposed to the density pot of the local concentration, $\mathcal{C}$.

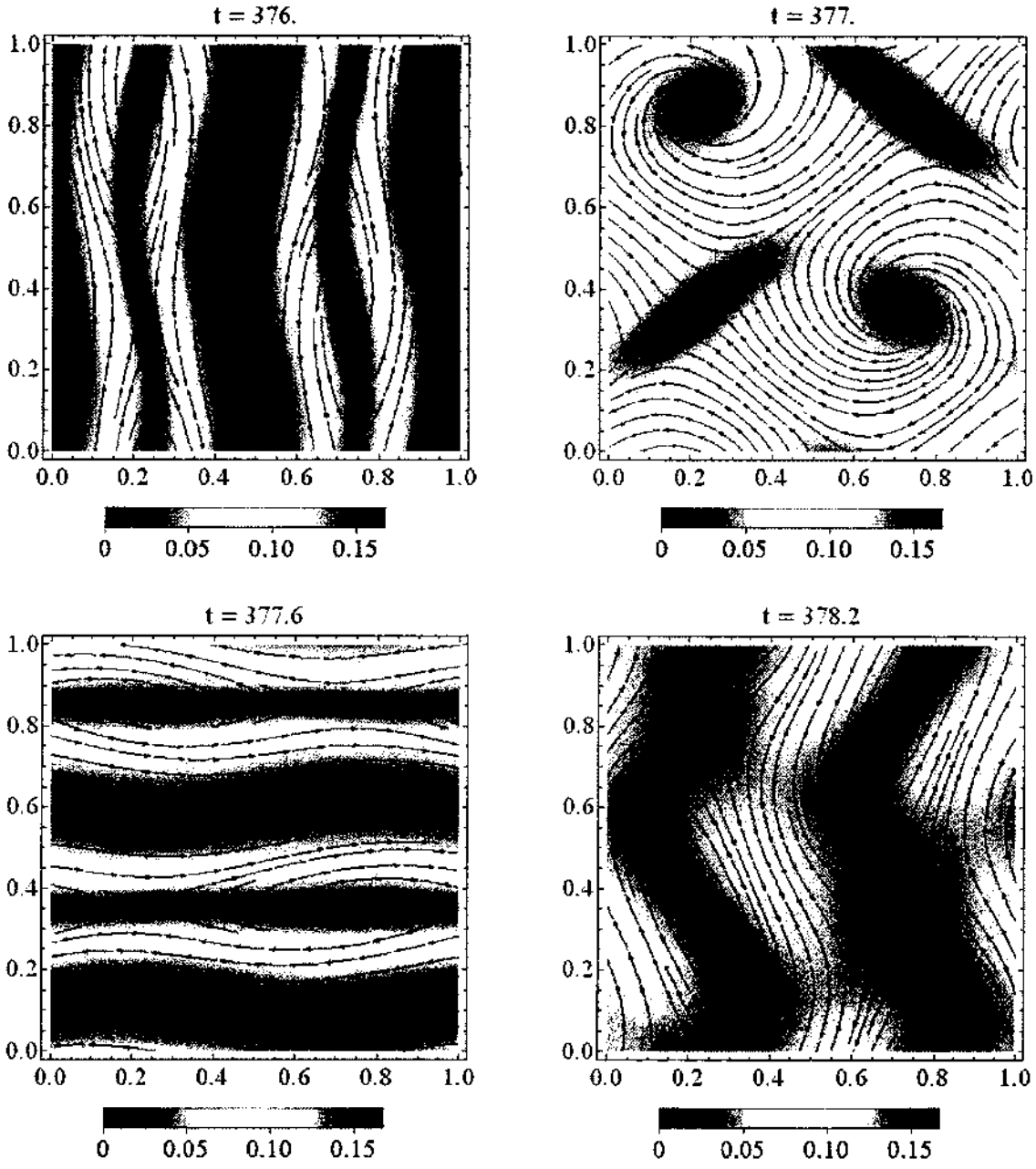

FIGURE 42: Snapshots of long time behavior of polarization direction , $\mathbf{p}$, superimposed to the density plot of $|\mathbf{p}|$.

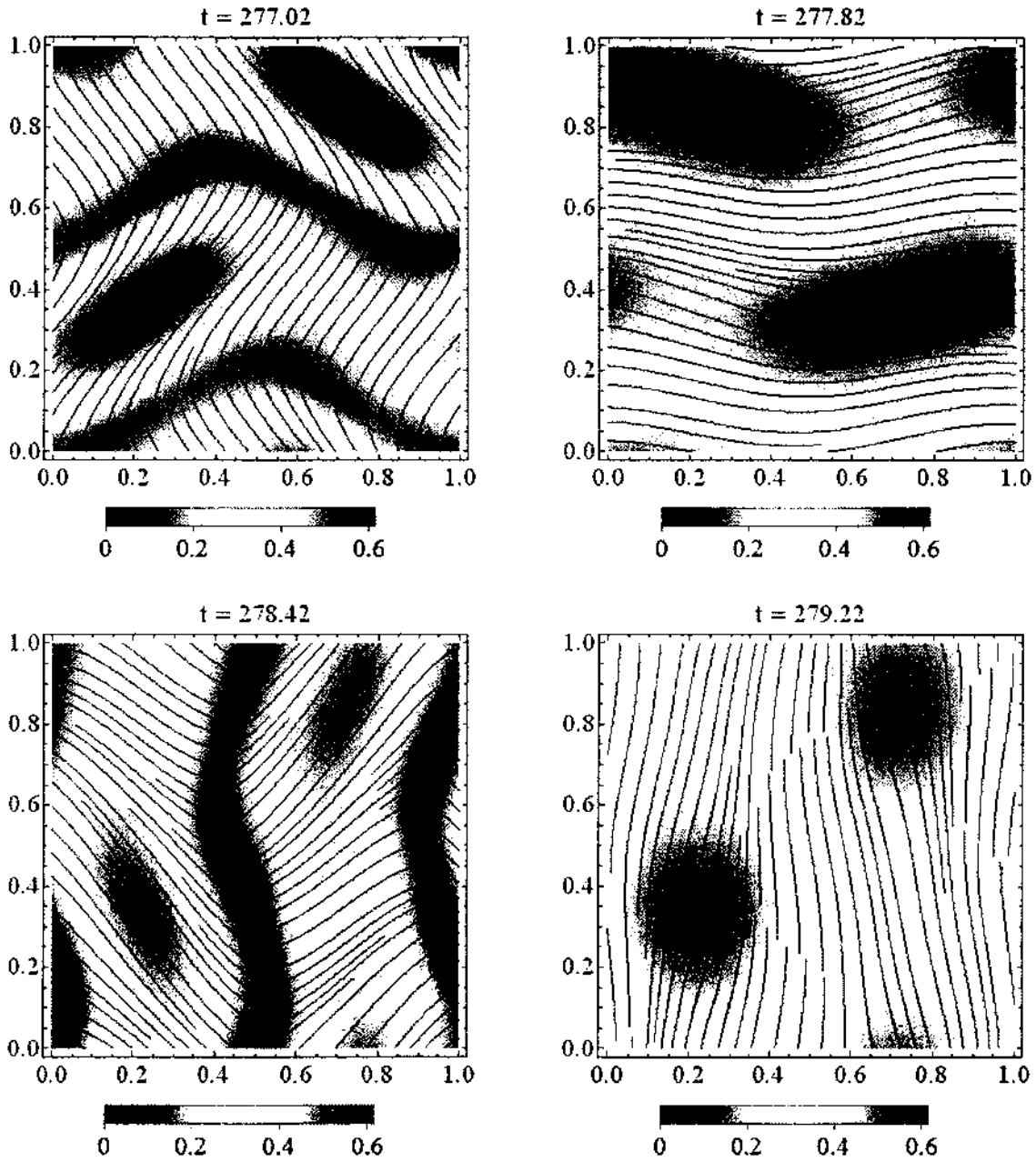

FIGURE 43: Snapshots of long time behavior of nematic orientation , $\mathbf{n}_1$, superimposed to the density plot of the degree of alignment, s.

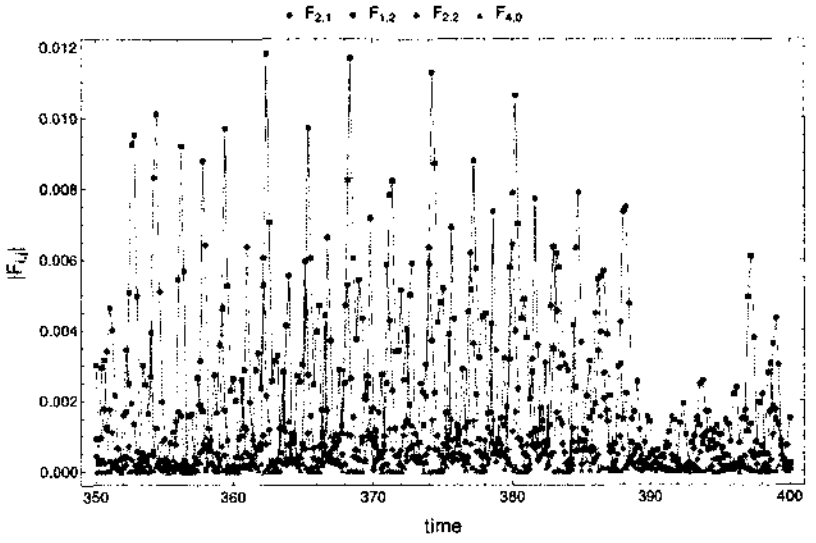

FIGURE 44: Time evolution of the magnitude of various spatial Fourier modes of the local concentration field, $\mathcal{C}$.

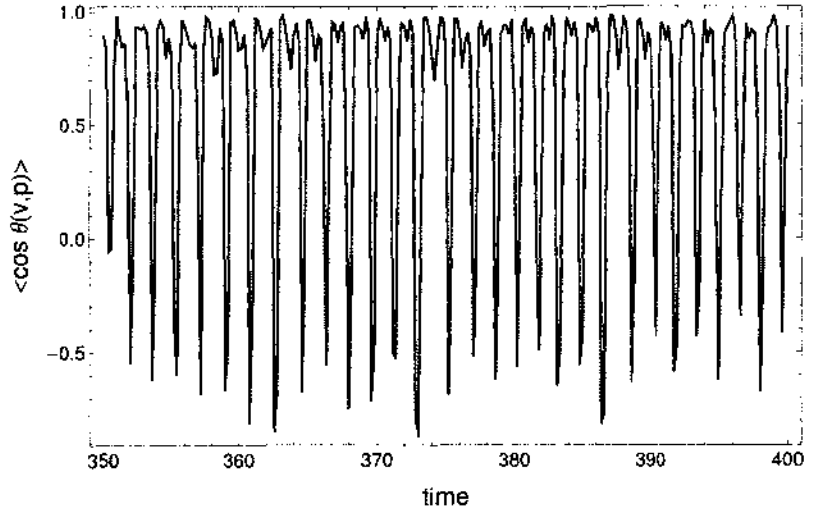

FIGURE 45: Spatially averaged correlation between the velocity , $\mathbf{v}$, and polarization direction, $\mathbf{p}$.

Irregular oscillatory state

We also discover additional unstable pattern which occurs during the simulation in 4x4 square domain (see Figure 46) using the parameters shown in Table 9. As it can be seen in velocity field (left column) and polarization direction (middle column), the center of spinning vortices, the saddle points, and the dense regions of local concentration (high C) appear to travel in random directions. Likewise, the nematic orientation (right column) now continuously shift in unpredictable fashion with the defect line changing location and direction irregularly. We remark that the patterns of the defect are consistent with the recent experiment of active microtubule liquid crystals by Sanchez and coworkers [**33**], which they observe the nematic director configuration around disclination defects of charge $1/2$ and $-1/2$ (see Figure 47 for the schematic illustrations). Figure 48 shows one snapshot of nematic director field at time $t = 380$ in which the topological defect with $1/2$ disclination occurs in box B, and, at the same time, the defect with $-1/2$ disclination occurs in box A.

The uncommon oscillations are illustrated more clearly in Figure 49 showing the time evolution of various spatial Fourier modes of the local concentration, and Figure 50 presenting the velocity as a function of time at the center of simulation domain $x = y = 2$. Both figures clearly suggest that the configurations of active suspension in this case exhibit slower fluctuation than those in the unit square domain resulting in smoother flows, i.e. no abrupt change of the velocity or polarity direction. Interestingly, the polarity and the fluid velocity are positively correlated at all times as shown in Figure 51. The irregular oscillation patterns of active suspensions are also reported in other studies [**12, 42**].

Parameter	Value
N	1
a	1
De	15
$N1$	3
$U0$	1
D_s^*	0.05
γ	1
c	1
G	1
α_0	1
Re	10
Re_2	10
Re_3	10
ζ_a	-2.5
$\overline{\alpha}$	1

TABLE 9: Parameter values used to obtain the results in Figure 46.

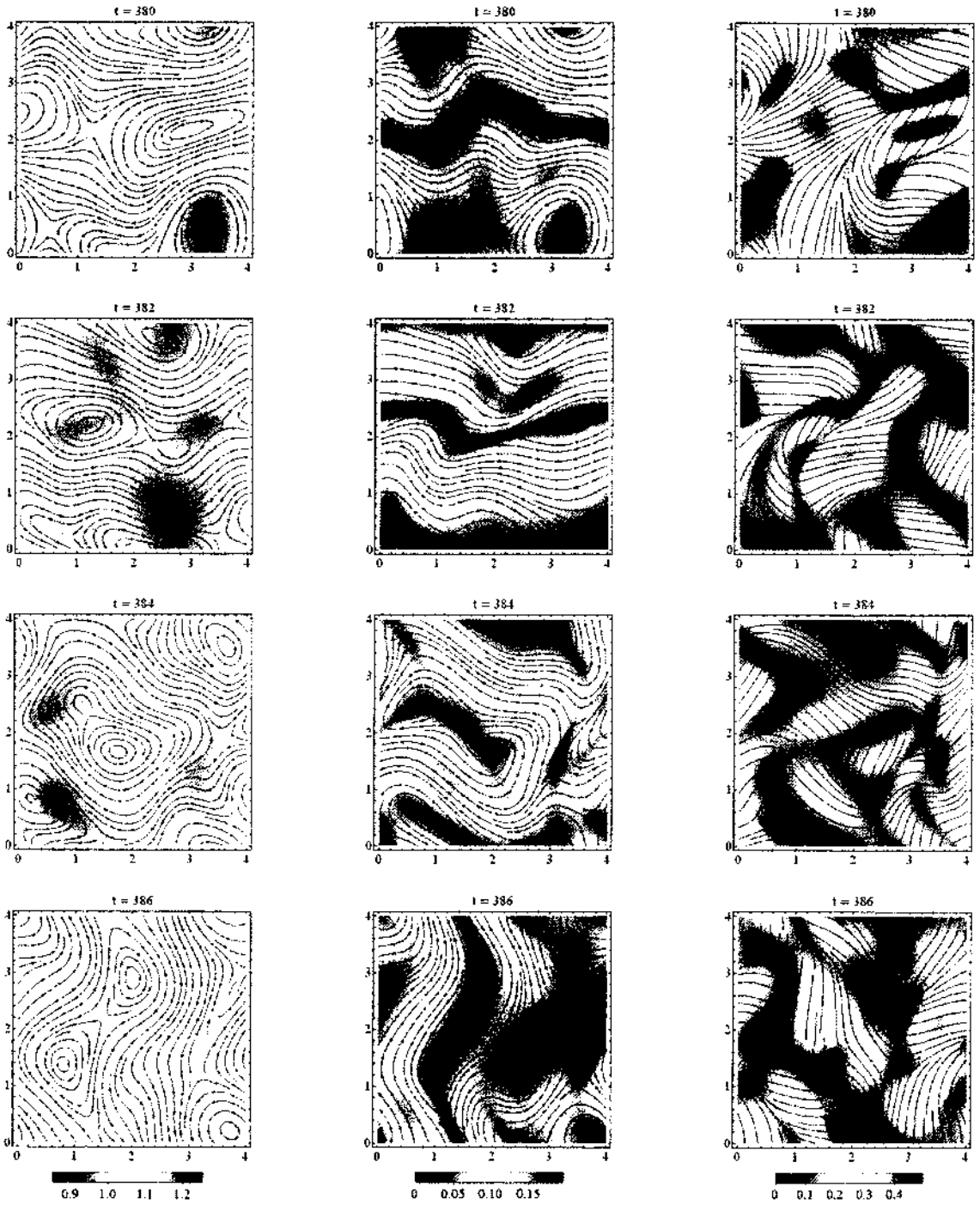

FIGURE 46: Irregular oscillation during the simulation in 4x4 domain. Left column: the velocity filed, $\mathbf{v}$, superimposed to local concentration, $\mathcal{C}$. Middle column: the mean director field, $\mathbf{p}$, superimposed to the density plot of $|\mathbf{p}|$. Right column: the nematic orientation superimposed to the density plot of the degree of alignment, s.

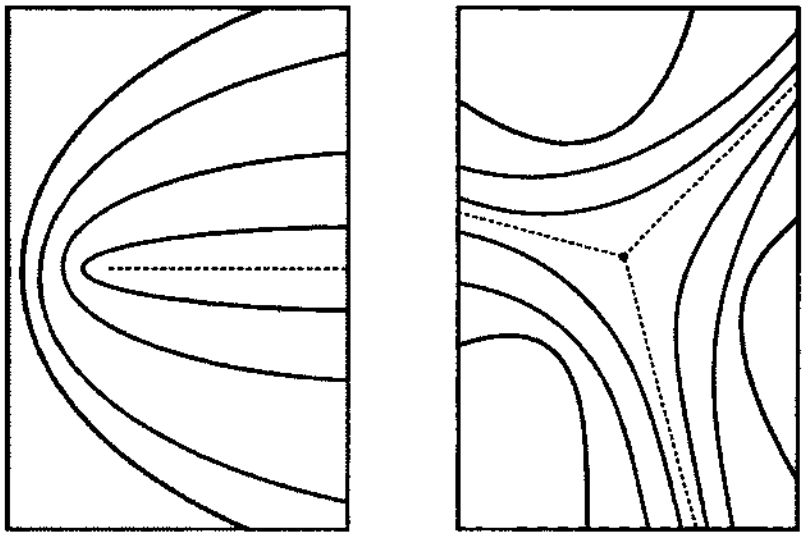

FIGURE 47: Schematic illustrations of the nematic director configuration around disclination defects of charge $1/2$ (left) and $-1/2$ (right).

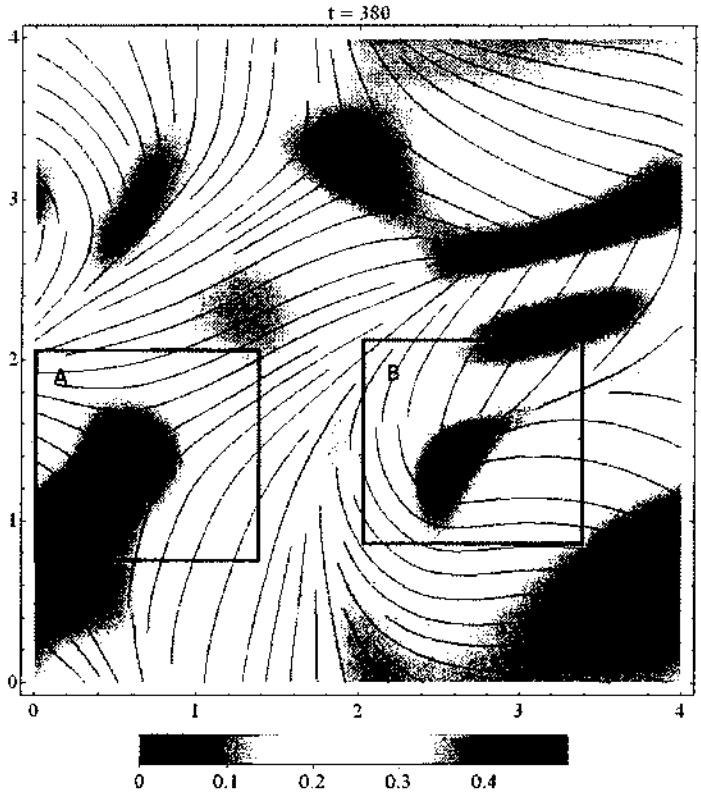

FIGURE 48: Topological defect with $1/2$ (box B) and $-1/2$ (box A) disclinations during the simulation in 4x4 domain.

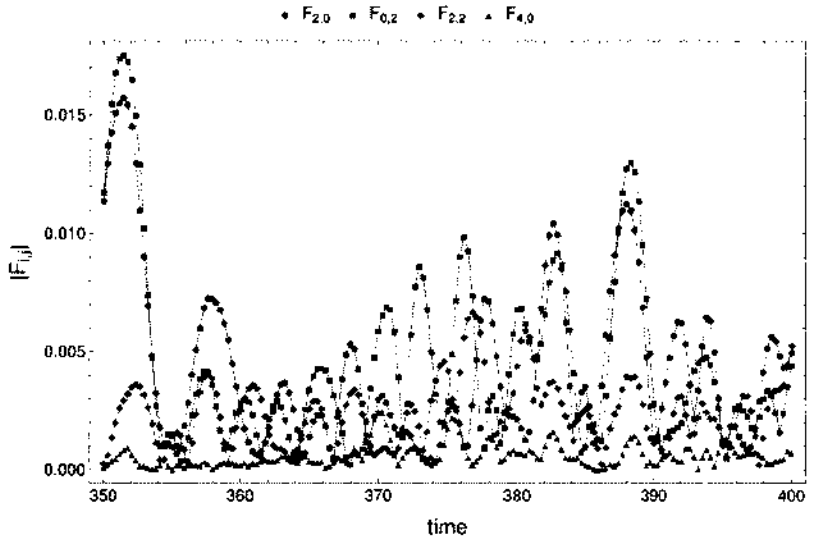

FIGURE 49: Time evolution of the magnitude of various spatial Fourier modes of the local concentration field, $\mathcal{C}$, during the irregular oscillation state of the active suspension.

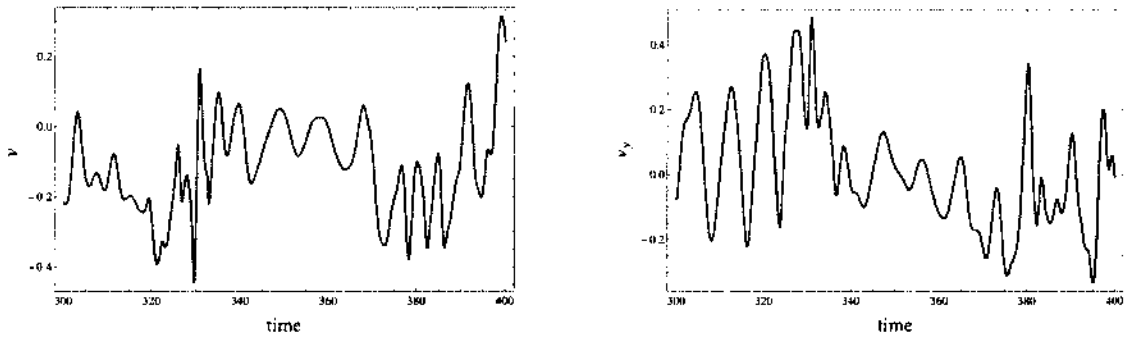

FIGURE 50: The plot of velocity during the irregular oscillation state at the center of simulation domain, $x = y = \frac{1}{2}$. Left: the plot of the horizontal component of the velocity, v_x, as a function of time. Right: the plot of the vertical component of the velocity, v_y, as a function of time.

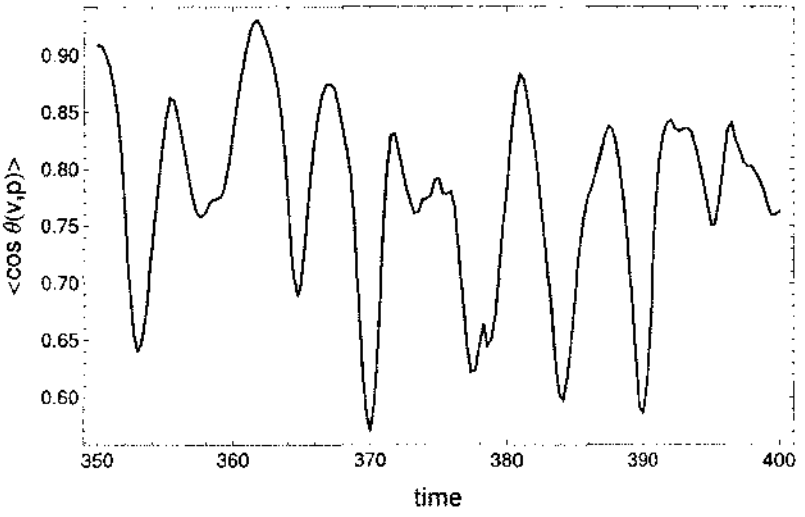

FIGURE 51: Spatially averaged correlation between the velocity , $\mathbf{v}$, and polarization direction, $\mathbf{p}$, during the irregular oscillation state of the active suspension.

Parameter	Value
N	0.5
a	1
De	5
$N1$	3
$U0$	1
D_s^*	0.01
γ	1
c	1
G	1
α_0	1
Re	10
Re_2	10
Re_3	10
ζ_a	-2.5
$\overline{\alpha}$	1

TABLE 10: Parameter values used to obtain flow reversal and 1D banded pattern of active suspension in 4x1 domain.

4.6.2 RECTANGLE DOMAIN

For our simulations in rectangle domains, strongly oscillatory spatio-temporal structures are also observed. However, the formations of the suspensions observed in this case are different from what we discover in the case of square domains as will be shown in the followings.

Periordic state: 1D banded patterns with flow reversal.

We begin presenting our results for the simulation in rectangle domain with a flow reversal and one dimensional banded pattern. All parameters used in simulation are listed in Table 10. Figure 52 shows the snapshots of the flow field, $\mathbf{v}$, superimposed to the density plot of local concentration, C, with the color bar located on the right as its gauge. Here, it is interesting to see from the scale of the color bar that the fluctuations of local concentration is low comparing to previous results from the simulations on square domain. The one dimensional structure of this state consists of two vertical reversible shear layers flowing in opposite directions. The quiescent flow along the x-axis is illustrated more clearly in Figure 53 presenting the velocity as a function of time at the center of simulation domain, $(x, y) = (2, \frac{1}{2})$. The plot

on the left shows that the horizontal component, v_x, of the velocity vanishes at all times while the plot on the right shows the oscillation of vertical component, v_y, of velocity resulting in the flow reversal along y-axis. We also confirm one dimensional structure by considering the time evolution of some spatial Fourier modes shown in Figure 54. We can see from the figure that the magnitude of all y-dependent modes, $F_{1,1}$, $F_{2,1}$, and $F_{0,2}$, are nearly zero whereas the pure x-dependent mode, $F_{2,0}$, saturate to periodic function with the period of 9.8. This approves both 1D structure and periordic behavior of the active suspension.

Figure 55 shows the polarity director field, $\mathbf{p}$, superimposed to the density plot of the polarity magnitudes, $|\mathbf{p}|$. The structures of the polarization direction are very similar to those of the vertical field. We again discover two vertical shear layers with opposite direction and the reversal of the polarity direction occurring during the period of evolution. The polarity magnitudes are in the form of vertical band that fluctuate through time. The switching of the polarization direction during the time period is investigated more in details in Figure 56 presenting the cross-sectional data by the plot, at two different times, of the polarization angle, ϕ, as a function of y with fixed $x = 2$ (left figure), and similar plot for fixed $y = \frac{1}{2}$ (right figure). The dashed and solid line represent the polarity angle at $t = 382.8$ and $t = 292.8$ respectively. From both figures, we clearly observe the 180° shifting of the polarity angle, thus implying the reversal of polarization direction. The correlation between the velocity and the polarization direction is also investigated and shown in Figure 57 which is similar to the results of periodic state in a unit square domain, but with larger period.

Figure 58 shows the snapshots of namatic orientation, ψ, superimposed to the density plot of the degree of alignment, s. We observe banded structures for the degree of alignment just like the case of $|\mathbf{p}|$. Also, it is clear from the figure that the particles appear to shift their alignments from one angle to another. This oscillatory response is investigated more in details in Figure 59 showing the contour plot of the nematic orientation at two different times where the degree of the alignment reach its peak value. We can see that the the suspension can be categorized by two different regimes, i.e $\psi \approx 50°$ and $\psi \approx -50°$. This implies that, in one period, the particles in the band switch their alignments back and forth between these angles. We also discover another the periodic state during simulation in 8x1 domain using parameter listed in Table 11. However we find that the simulation yields the same structures as

Parameter	Value
N	0.25
a	1
De	15
$N1$	3
$U0$	1
D_s^*	0.01
γ	1
c	1
G	1
α_0	1
Re	10
Re_2	10
Re_3	10
ζ_a	-2.5
$\overline{\alpha}$	1

TABLE 11: Parameter values used to obtain flow reversal and 1D banded pattern of active suspension in 8x1 domain.

of 4x1 domain with twice repetitive patterns along the x-direction as seen in Figure 60 showing, from top to bottom, snapshots of velocity, polarity direction, and nematic orientation. Thus, this result will not be discussed here any further.

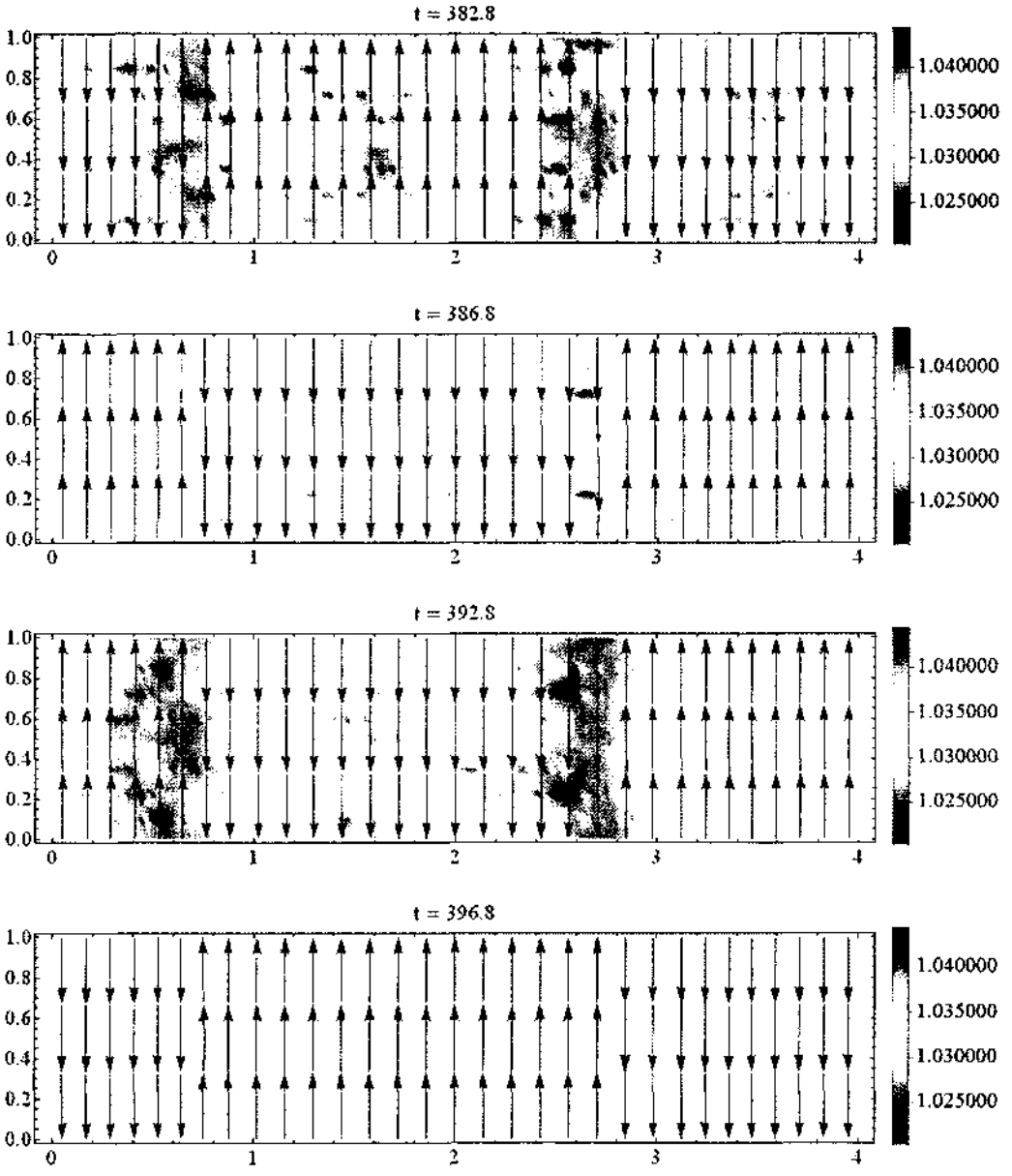

FIGURE 52: Snapshots of long time behavior of fluid velocity , $\mathbf{v}$, superimposed to the density pot of the local concentration, C.

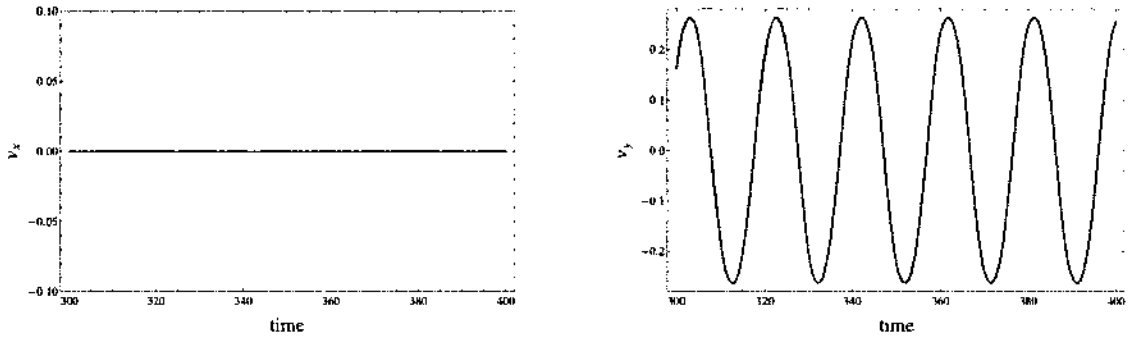

FIGURE 53: The plot of velocity during periodic state at the center of simulation domain, $x = y = \frac{1}{2}$. Left: the plot of the horizontal component of the velocity, v_x, as a function of time. Right: the plot of the vertical component of the velocity, v_y, as a function of time.

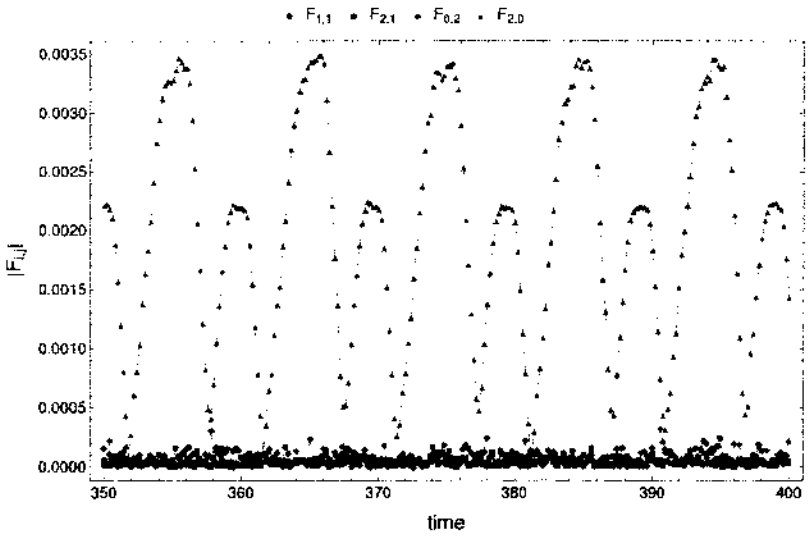

FIGURE 54: Time evolution of the magnitude of various spatial Fourier modes of the local concentration field, C.

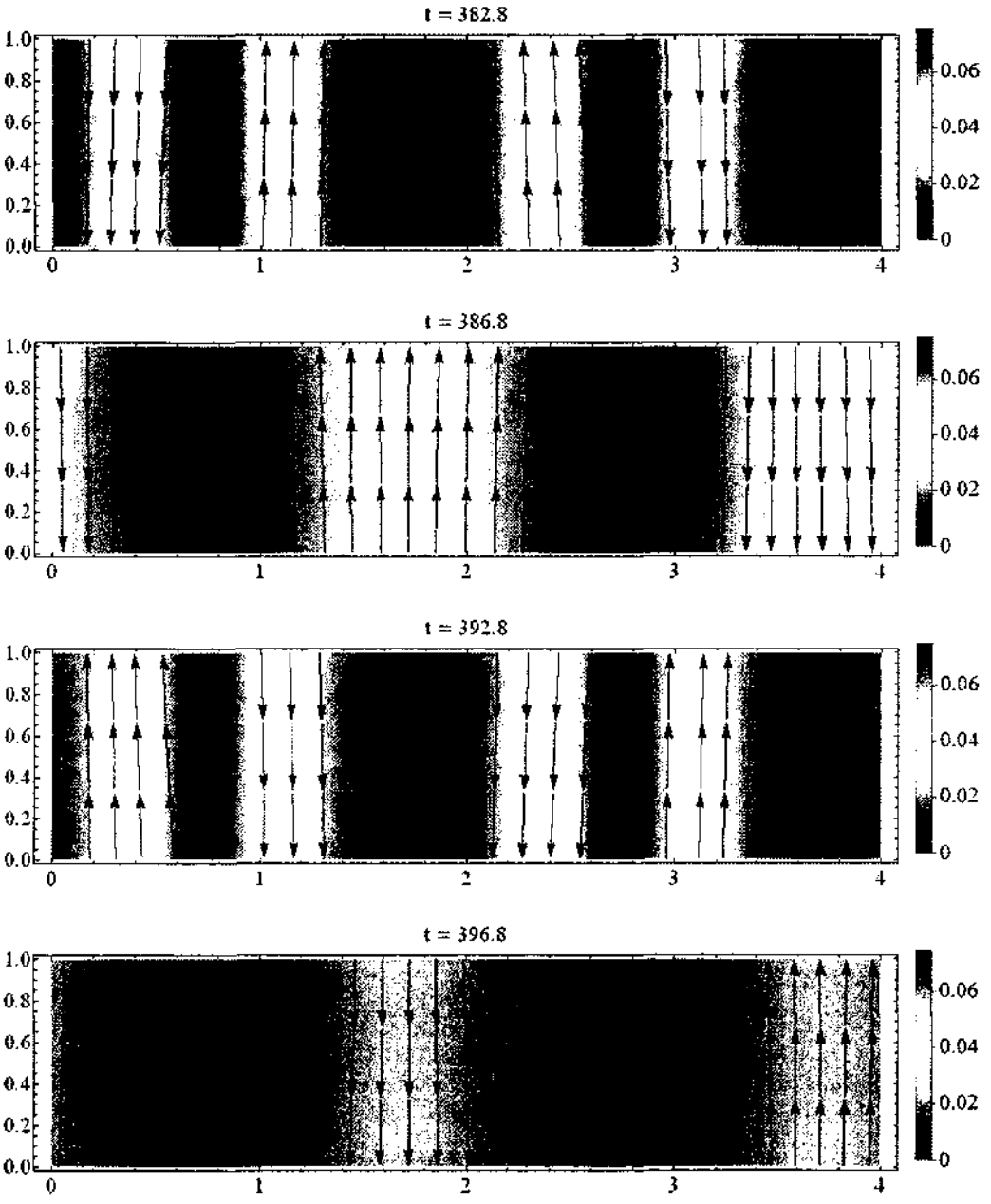

FIGURE 55: Snapshots of long time behavior of polarization direction , $\mathbf{p}$, superimposed to the density plot of $|\mathbf{p}|$.

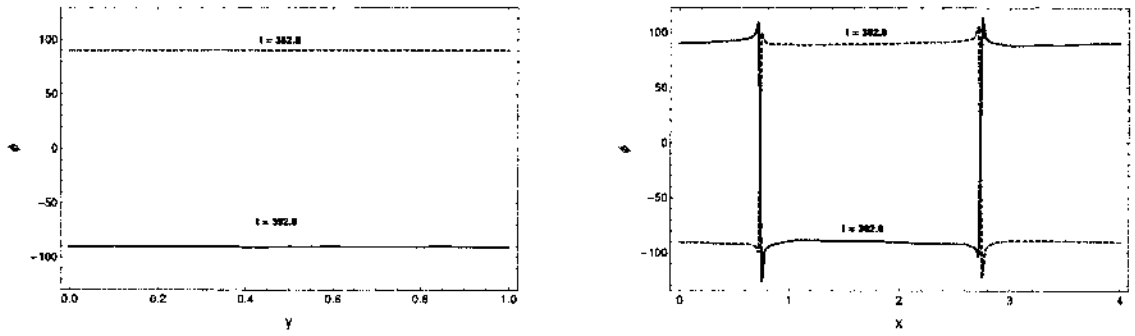

FIGURE 56: The cross-sectional data, at two different times, of the polarization angle, ϕ, as a function of y where $x = 2$ (left), and the cross-sectional data, at two different times, of the polarization angle, ϕ, as a function of x where $y = \frac{1}{2}$ (right). The solid and dashed lines represent two different times in the period.

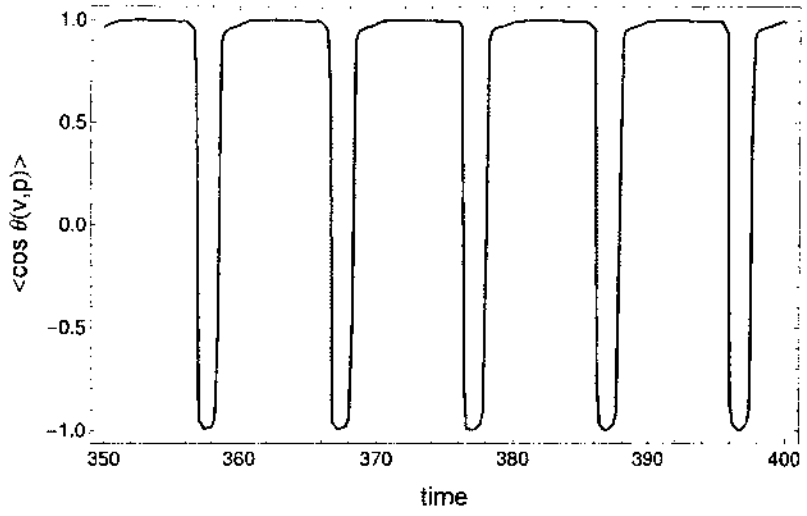

FIGURE 57: Spatially averaged correlation between the velocity , $\mathbf{v}$, and polarization direction, $\mathbf{p}$.

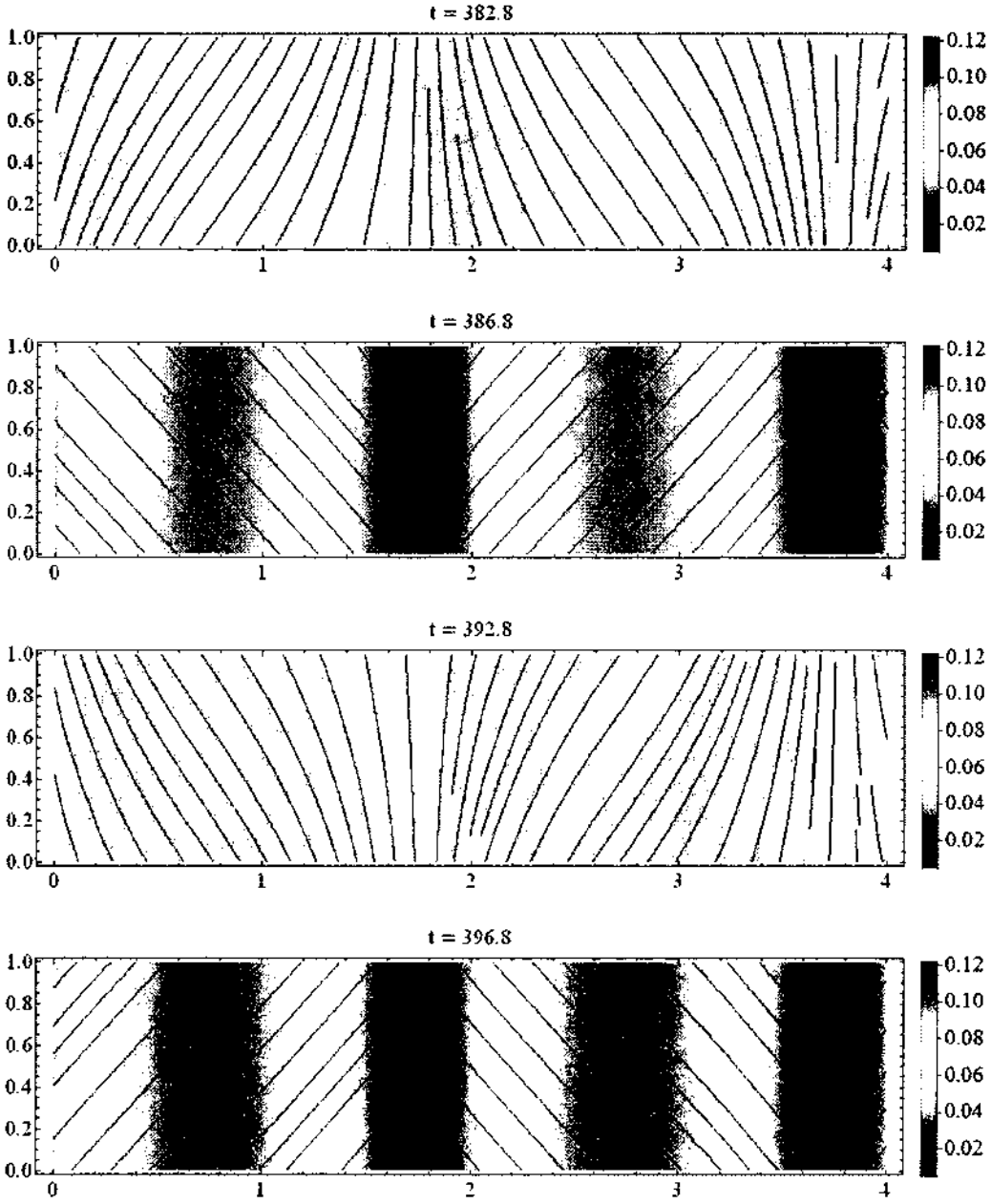

FIGURE 58: Snapshots of long time behavior of nematic orientation , $\mathbf{n}_1$, superimposed to the density plot of the degree of alignment, s.

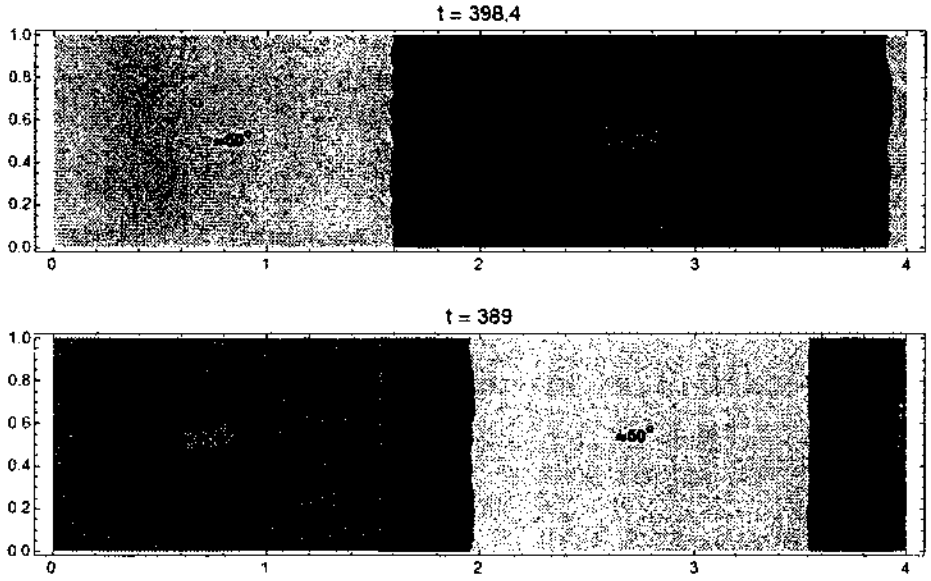

FIGURE 59: The contour plot of nematic orientation angle, ψ, in Figure 58, at two different times in the period.

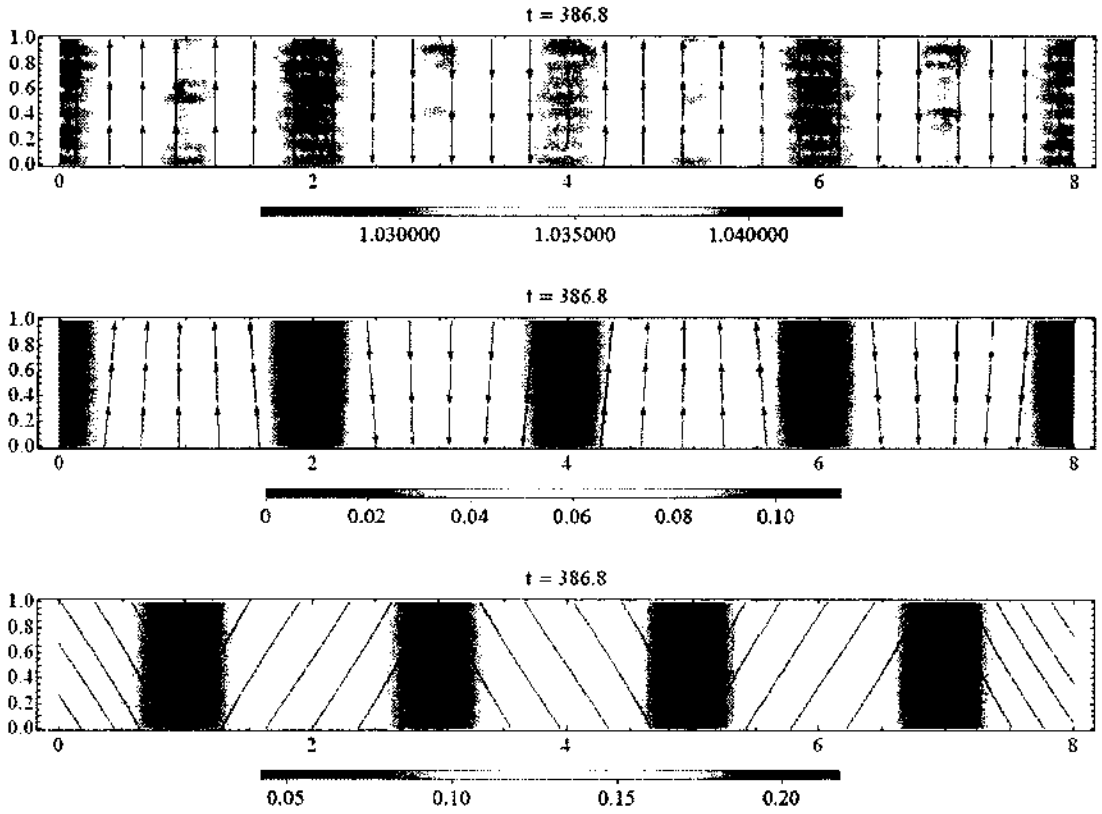

FIGURE 60: Snapshots of long time behavior of the active suspension simulated in 8x1 domain with parameter shown in Table 11. Top: Velocity field, $\mathbf{v}$, painted with local concentration, $\mathcal{C}$. Middle: Polarization direction, $\mathbf{p}$, painted with $|\mathbf{p}|$. Bottom: Nematic orientation $\mathbf{n_1}$, painted with degree of alignment, s.

Parameter	Value
N	0.5
a	1
De	15
$N1$	3
$U0$	1
D_s^*	0.01
γ	1
c	1
G	1
α_0	1
Re	10
Re_2	10
Re_3	10
ζ_a	−3.5
$\overline{\alpha}$	1

TABLE 12: Parameter values used to obtain traveling wave pattern of active suspension in 4x1 domain.

Quasiperiordic state: Traveling waves.

Once we raise the magnitude of active parameter to 3.5 and adjust the nematic strength to 0.5 with all other parameters fixed (see Table 12), the flow switching 1D banded pattern disappears and the traveling wave emerges in the system. As shown in Figure 61, there are two shear layers flowing along y-direction in opposite directions. Here, the dense regions of the local concentration (high C) appear at the boundary between two shear and follow the flow at constant speed, thus forming traveling waves across y-direction. Note that, in this case, the flow reversal occurs only long x-direction. The dynamics of the flow are confirmed by Figure 62 showing the horizontal component, v_y, and vertical component, v_x, of the velocity as a function of time at the center of simulation domain $(x, y) = (2, \frac{1}{2})$. We can see in the figure that both components exhibit quasiperiodicity with v_y oscillates only in the positive region, thus explaining no flow reversal along y-direction. The quasiperiodicity is further investigated in Figure 63 showing the magnitude of Fourier spectrum of time series of v_x (left figure) and v_y (right figure). Since both time series are dominated by high frequency modes, we expect that the configurations of the suspension should exhibit much faster fluctuation than previous case (periodic state).

We also observe two layers pattern for the polarization direction, $\mathbf{p}$, as seen in

Figure 64 showing two regions characterized by the magnitude of polarity, $|\mathbf{p}|$, traveling in opposite directions. This is illustrated more clearly in Figure 65 presenting the cross-sectional data by the plot of polarization angle, ψ, along x-axis with fixed $y = \frac{1}{3}$ (dashed line), $y = \frac{1}{2}$ (solid line), and $y = \frac{2}{3}$ (dotted line). Here, the difference in ϕ between two regions ($x \in (0.37, 2.43)$ and $x \in (2.43, 4)$) is roughly 180°. We again examine the velocity-polarity correlation and find that the velocity and polarization direction are positively correlated at all times as shown in Figure 66.

Interestingly, it appears that the degree of alignment, s, also possesses the traveling waves behavior as seen in Figure 67 showing the dense region (high s) and the defect ($s \approx 0$) traveling up (down) on the left half (right half) of the domain.

In fact, one can notice that the structure at this quasiperiordic state is similar to 1D structure with little flow and polarity reversal along x-direction. This is in agreement with Figure 68, which shows the time evolution of various modes of spatial Fourier decomposition of the local concentration, C. It is clear from the figure that the spectrum is again dominated by pure x- depandent modes, $F_{2,0}$ and $F_{4,0}$ with the period of 1.4.

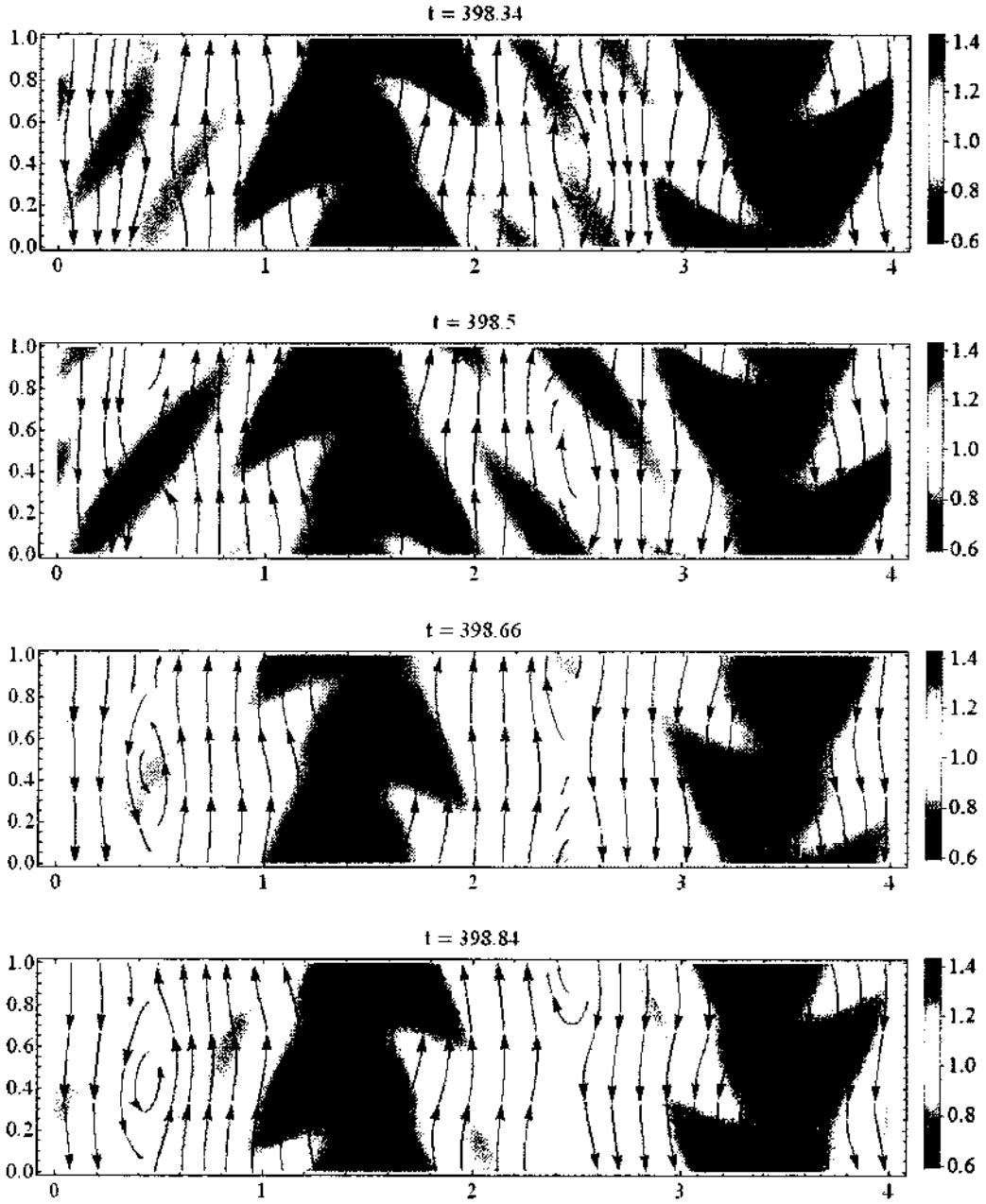

FIGURE 61: Snapshots of long time behavior of fluid velocity , $\mathbf{v}$, superimposed to the density pot of the local concentration, C.

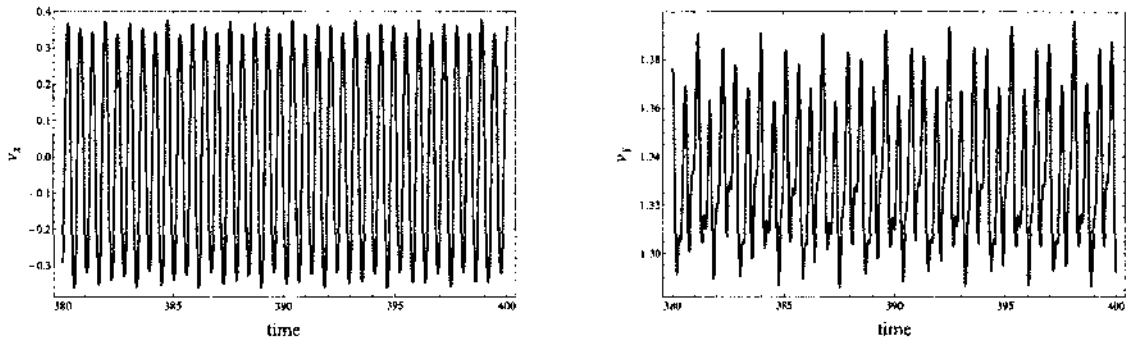

FIGURE 62: The plot of velocity during periodic state at the center of simulation domain, $x = y = \frac{1}{2}$. Left: the plot of the horizontal component of the velocity, v_x, as a function of time. Right: the plot of the vertical component of the velocity, v_y, as a function of time.

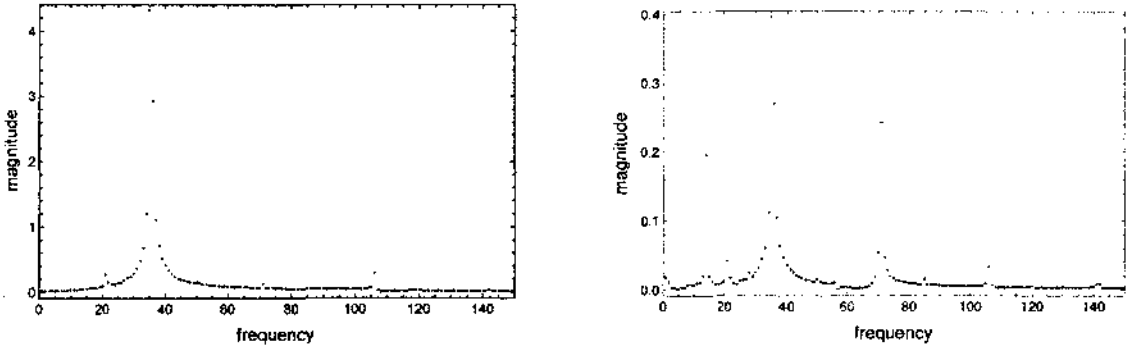

FIGURE 63: The magnitude of discrete Fourier transform spectrum of the time series of the horizontal component, v_x, (left) and the vertical component, v_y, (right) of the velocity at the center of simulation domain $(x, y) = (2, \frac{1}{2})$.

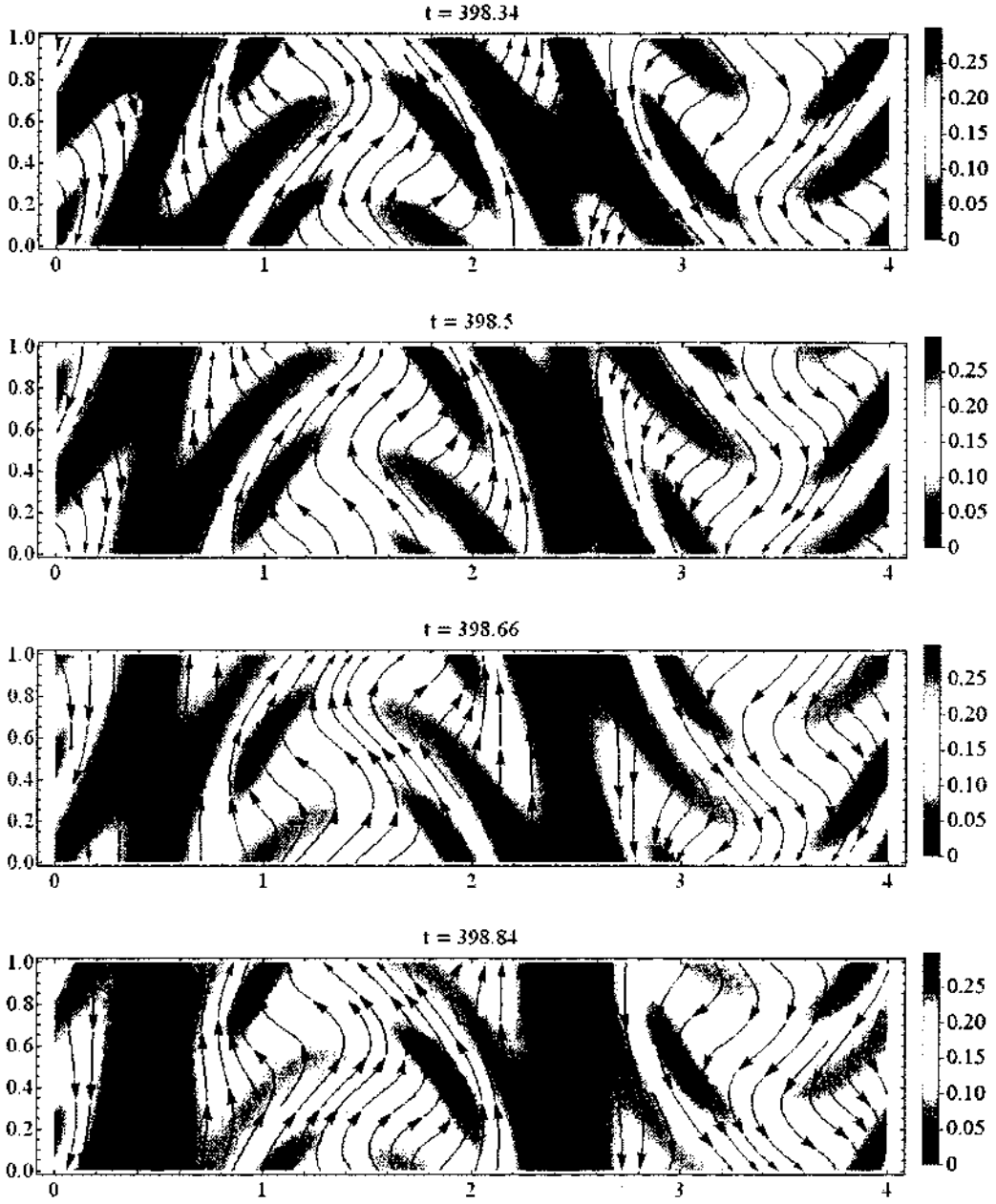

FIGURE 64: Snapshots of long time behavior of polarization direction , $\mathbf{p}$, superimposed to the density plot of $|\mathbf{p}|$.

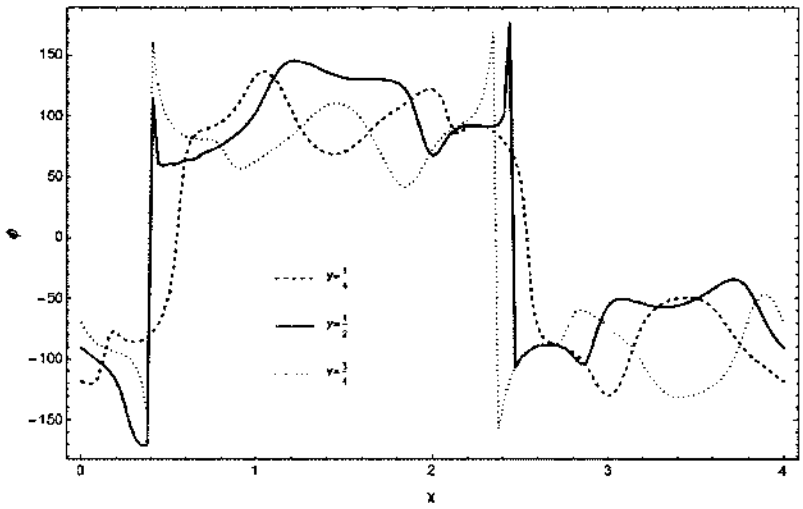

FIGURE 65: The cross-sectional data of the polarization angle, ϕ, as a function of x where $y = \frac{1}{3}$ (dashed line), $y = \frac{1}{2}$ (solid line), and $y = \frac{2}{3}$ (dotted line).

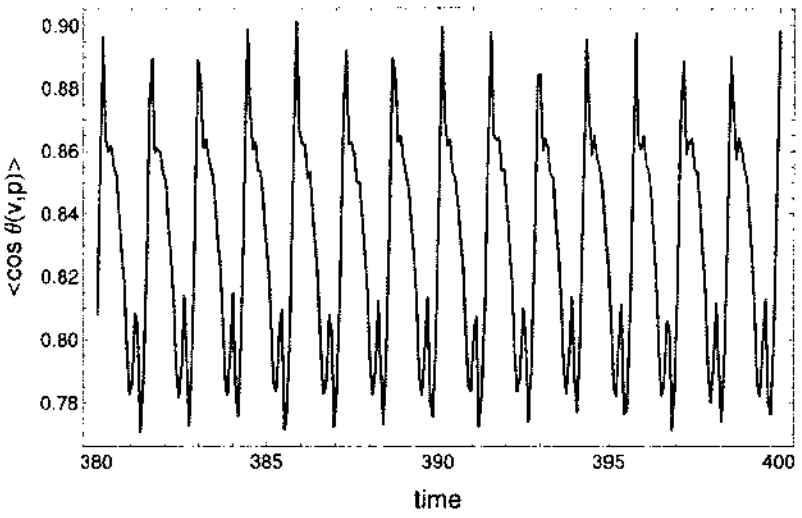

FIGURE 66: Spatially averaged correlation between the velocity , $\mathbf{v}$, and polarization direction, $\mathbf{p}$.

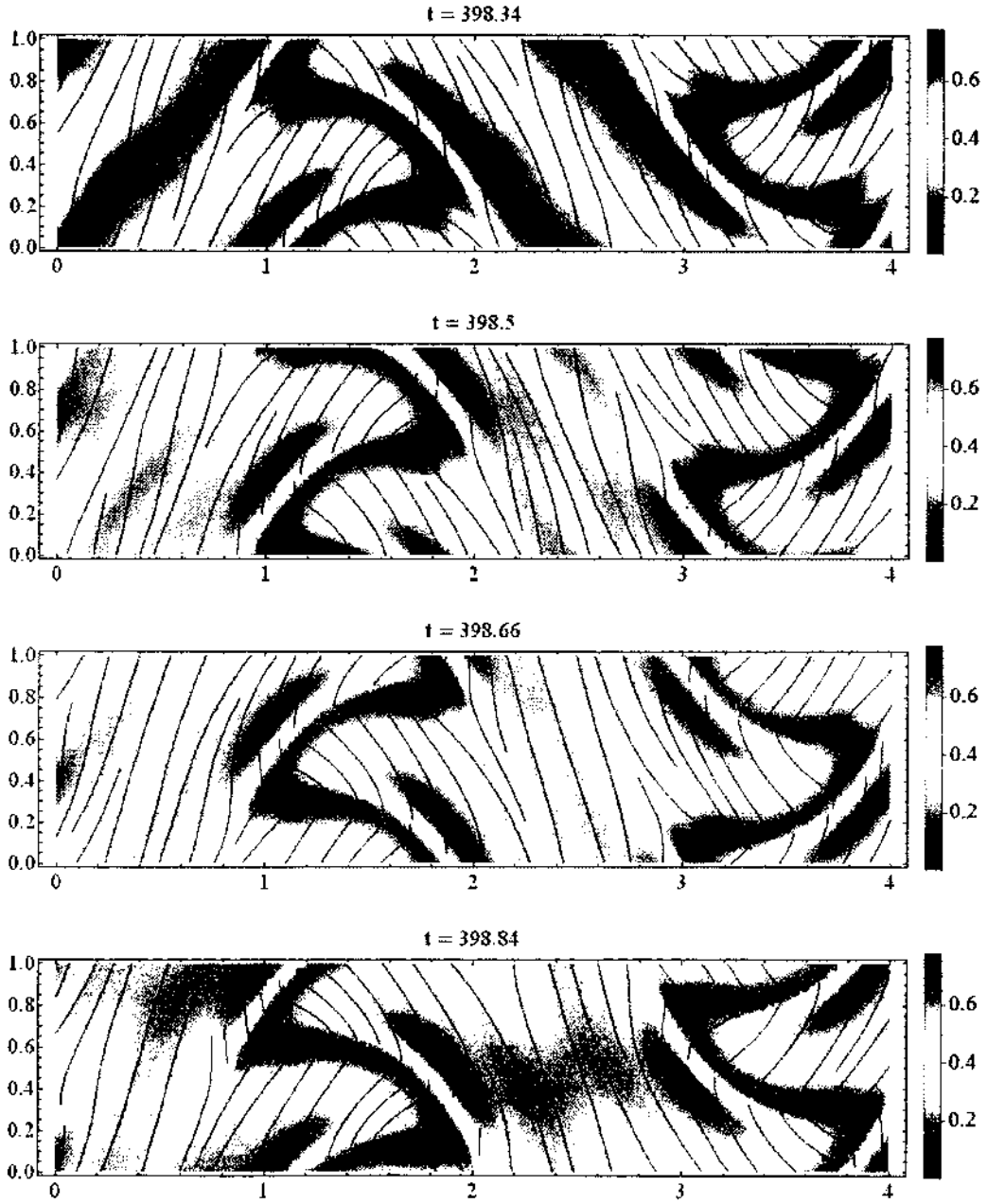

FIGURE 67: Snapshots of long time behavior of nematic orientation , $\mathbf{n_1}$, superimposed to the density plot of the degree of alignment, s.

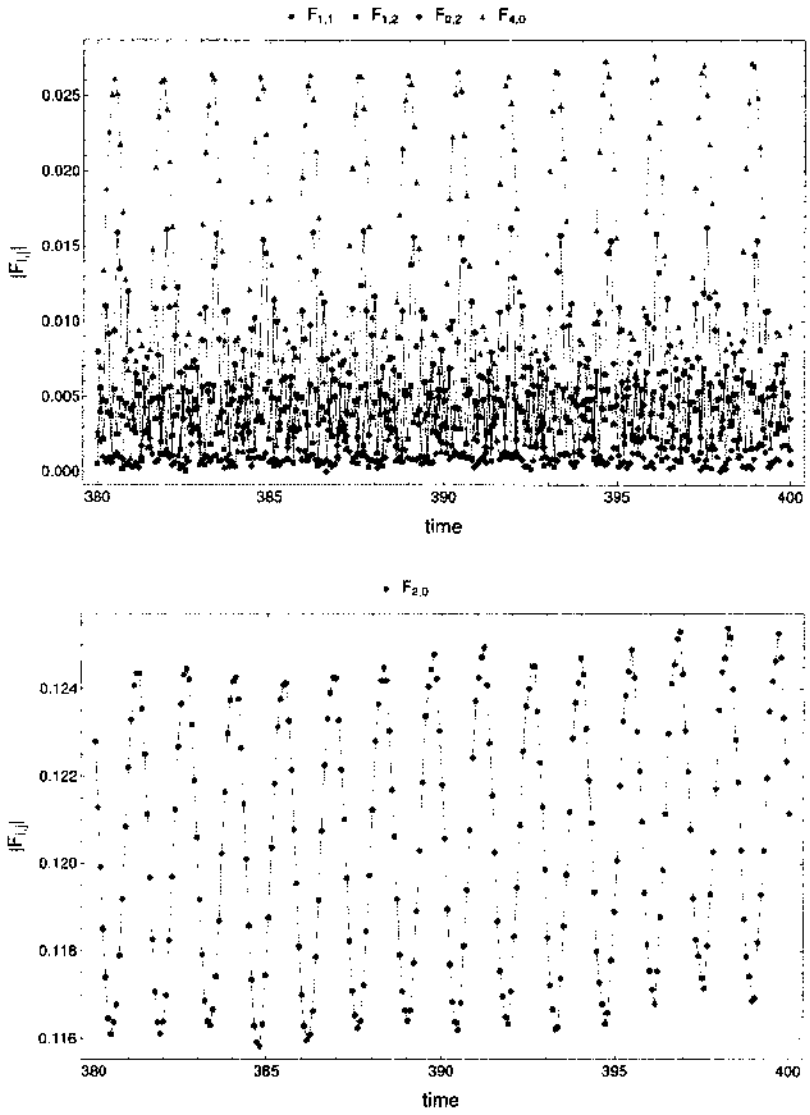

FIGURE 68: Time evolution of the magnitude of various spatial Fourier modes of the local concentration field, $\mathcal{C}$.

CHAPTER 5

CONCLUSIONS

In this research, we investigate a recently proposed kinetic model for dilute suspensions of self-propelled particles [7], which are assumed to be long thin polar rods that move along their axis of symmetry. By using this model and the assumption that there are no particle interactions, we analyze the linear stability of the suspensions about uniform isotropic state without disturbance flow and find that this state is stable only in small ranges of the strength of polarity, $\gamma < 2$, and nematic interaction, $N < 2$. Out of this region, stable nematic state becomes a new attractor which indicates that the particles prefer to align in some directions. We then analyze the weak flow perturbation by imposing simple weak shear to this stable state. From this, it turns out that many explicit formulas for the alignment angle, degree of alignment, and normal and shear stresses can be derived. These closed-form formulas are confirmed by numerical results. Notable outcome is that the particles are steady aligned with the flows, with an alignment angle of 45° in the weak shear limit. We also numerically study the stability and rheological properties of the active suspension when the shear flow is not necessarily weak. We discover at this time that the formula for the angle of alignment is not valid when the strength of nematic interaction is high, $N > 2$. In fact, the numerical results suggest that the particles may exhibit oscillatory response rather than steady alignment even in weak shear limit. However, in any case, the steady flow-alignment will still occur given strong enough flow. Additionally, we find the bistable region where both periodic and flow-aligning states are stable. This phenomenon occurs when the strength of polarity, γ, and nematic interaction, N, are relatively high. The numerical results from the model also infer some important features of active suspension that the pusher causes negative effect to the fluid viscosity and the opposite for the puller.

Lastly, we consider the case when the effects from the interactions between particles are taken into account. We first develop the numerical method by approximating the number density function, f, by truncated Fourier transform. After substitutions, manipulations and simplifications, we end up with a truncated system of 41 partial

differential equations that need to be solved together with the Navier-Stokes equations. We then extensively conduct numerical simulations to investigate long-time behavior and structure of the active suspensions on square and rectangle domains. Many simulations are performed in square and rectangle domains by varying the nematic strength, N, the Deborah number, De, the transnational diffusion, D_s^*, and the active parameter, ζ_a.

We frequently observe time-periodic structures of suspensions when the numerical simulations are performed on a unit square domain. We discuss various features of this periodic pattern, for example, the reversal of velocity and polarization director, the rotations of nematic orientation, and the fluctuations of scalar quantities such as the local concentration, the magnitude of polarity, and the degree of alignment. We find that the spatially averaged correlations between velocity and polarization direction are mostly positive. However, there is the time when the polar director goes against the flow direction. This happens during the flow reversal where the velocity becomes weak. The steady state of the suspension occurs at high activity of active particles ($\zeta_a = -15$). The interesting result in this case is the negative correlation between velocity and polarization direction which indicates that, on average, the particle does not swim with the flow. We also observe the irregular structure where there are different quasiperiodic fluctuations corresponding to different time intervals. In this state, the regions of polarization direction are in the form of vertical and horizontal banded structure while the general structure of velocity field are in the form of position switching between spinning vertices and saddle points. We also obtain an additional irregular/chaos pattern which occurs during the simulation in 4x4 domain. We observe from velocity field and polarization direction that the center of spinning vortices, the saddle points, as well as the dense regions of local concentration appear to travel in random directions. The nematic orientation also continuously shift without specific pattern.

For the rectangle domain, we mostly perform the simulation in 4x1 domain and observe two main patterns. First, we observe the periodic state with 1D vertical banded pattern with flow reversal, in which the horizontal components of both velocity and polarization director vanish. The structures of velocity and polarity are characterized by two shear layers flowing in opposite directions. The flow reversal occurs in every period of time and the nematic orientation switches back and forth

between 50° and −50°. This pattern also appears during the simulation in 8x1 domain but with twice repetitive pattern along the x-direction. The second pattern is more interesting, where two vertical shear layers of velocity and polarity director flowing in opposite directions but with quasiperiodic oscillations along the horizontal direction. However, there is no reversal appearing anywhere along the vertical direction. Also, the dense regions of the local concentration, the magnitude of polarity, and the degree of nematic alignment move along the flow at constant speed. As a result, we observe two vertical traveling waves moving in opposite directions.

REFERENCES

1. A. J. Chorin, *Numerical solution of the Navier-Stokes equations*, Math. Comp. **22** (1968), 745762.

2. R. Courant, K. Friedrichs and H. Lewy, *On the partial difference equations of mathematical physics*, AEC Research and Development Report NYO-7689 (1956).

3. E. Doedel, *AUTO: software for continuation and bifurcation problems in ODEs*, http://indy.cs.concordia.ca/auto, 1996.

4. M. Doi and S. F. Edwards, *The Theory of Polymer Dynamics*, Oxford University Press, 1986.

5. W. M. Durham, J. O. Kessler and R. Stocker, *Disruption of vertical motility by shear triggers formation of thin phytoplankton layers*, Science **323** (2009), 1067-1070.

6. Y. Farhoudi and A. D. Rey, *Shear flows of nematic polymers. I. orienting modes, bifurcations, and steady state rheological predictions*, J. Rheol. **37** (1993), 289.

7. M. G. Forest, Q. Wang and R. Zhou, *Kinetic theory and simulations of active nematic polymers*, Soft Matter **9** (2013), 5207-5222.

8. M. G. Forest, Q. Wang and R. Zhou, *The flow-phase diagram of Doi-Hess theory for sheared nematic polymers II: finite shear rates*, Rheol. Acta **44** (2004), 80-93.

9. M. G. Forest, R. Zhou and Q. Wang, *Scaling behavior of kinetic orientational distributions for dilute nematic polymers in weak shear*, J. Non-Newton. Fluid **116** (2004), 183204.

10. M. G. Forest, R. Zhou and Q. Wang, *Symmetries of the Doi kinetic theory for nematic polymers of arbitrary aspect ratio: at Rest and in linear flows*, Phys. Rev. E. **66** (2002), 031712.

11. L. Giomi, L. Mahadevan, B. Chakraborty and M. F. Hagan, *Excitable patterns in active nematics*, Phys. Rev. Lett. **106** (2011), 218101.

12. L. Giomi and C. Marchetti, *Polar patterns in active fluids*, Soft Matter **8** (2012), 129.

13. L. Giomi, M. C. Marchetti and T. B. Liverpool, *Complex spontaneous flows and concentration banding in active polar flims*, Phys. Rev. Lett. **101** (2008), 198101.

14. M. Griebel, T. Dornsheifer and T. Neunhoeffer, *Numerical Simulation in Fluid Dynamics: A Practical Introduction*, Society for Industrial and Applied Mathematics, 1998.

15. Y. Hatwalne, S. Ramaswamy, M. Rao and R. A. Simha, *Rheology of active-particle suspensions*, Phys. Rev. Lett. **92** (2004), 118101.

16. J. P. Hernndez-Ortiz, C. G. Stoltz and M. D. Graham, *Transport and collective dynamics in suspensions of confined self-propelled particles*, Phys. Rev. Lett. **95** (2005), 204501.

17. C. Hoheneger and M. J. Shelley, *Stability of active suspensions*, Phys. Rev. E. **81** (2010), 046311.

18. C. Hirt, B. Nichols and N. Romero, *A numerical solution algorithm for transient fluid flows*, NASA STI/Recon Technical Report **75** (1975).

19. T. Ishikawa, M. P. Simmonds and T. J. Pedley, *Hydrodynamic interaction of two swimming model micro-organism*, J. Fluid Mech. **568** (2006), 119-160.

20. H. P. Langtangen, *Computational Partial Differential Equations*, Springer, 2003.

21. P. L. Maffettone and S. Crescitelli *Bifurcation analysis of a molecular model for nematic polymers in shear flows*, J. Non-Newton. Fluid **59** (1995), 73-91.

22. M. C. Marchetti, J. F. Joanny, S. Ramaswamy, T. B. Liverpool, J. Prost, M. Rao and R. A. Simha, *Soft active matter* arXiv:1207.2929 [cond-mat.soft] (2012).

23. D. Marenduzzo, E. Orlandini, M. E. Cates and J. M. Yeomans, *Steady state hydrodynamic instabilities of active liquid crystals: hybrid lattice Boltzmann simulations*, Phys. Rev. E. **76** (2007), 031921.

24. M. R. Parsek and P. K. Singh, *Bacterial biofilms: an emerging link to disease pathogenesis*, Annu. Rev. Microbiol. **57** (2003), 677-701.

25. W. F. Paxton, K. C. Kristler, C. C. Olmeda, A. Sen, S. K. St. Angelo, Y. Cao, T. E. Mallouk and P. E. Lambert, *Catalytic nanomotors: autonomous movement of striped nanorods*, J. Am. Chem. Soc. **126** (2004), 1342413431.

26. W. F. Paxton, A. Sen and T. E. Mallouk, *Motility of catalytic nanoparticles through self-generated forces*, Chem. Eur. J. **11** (2005), 6462-6470.

27. S. Rafaï , L. Jibuti and P. Peyla *Effective viscosity of microswimmer suspensions*, Phys. Rev. Lett. **104** (2010), 098102.

28. D. Saintillan, *The dilute rheology of swimming suspensions: a Simple kinetic model*, Exp. Mech. **50** (2010), 1275-1281.

29. D. Saintillan and M. J. Shelley, *Active suspension and their nonlinear models*, C. R. Phys. **14** (2013), 497-517.

30. D. Saintillan and M. J. Shelley, *Instabilities, pattern formation, and mixing in active suspensions*, Phys. Fluids **20** (2008), 123304.

31. D. Saintillan and M. J. Shelley, *Instabilities, pattern formation in active particle suspensions: kinetic theory and continuum simulations*, Phys. Rev. Lett. **100** (2008), 178103.

32. D. Saintillan and M. J. Shelley, *Orientational order and instabilities in suspensions of self-locomoting rod*, Phys. Rev. Lett. **99** (2007), 058102.

33. T. Sanchez, D. N. Chen, S. J. DeCamp, M. Heymann and Z. Dogic, *Spontaneous motion in hierarchically assembled active matter*, Nature **491** (2012), 431-434.

34. J. R. Seymour, Marcos and R. Stocker, *Resource patch formation and exploitation throughout the marine microbial food web*, Am. Nat. **173** (2009), E15-29.

35. A. Sokolov and I. S. Aranson *Reduction of viscosity in suspension of swimming bacteria*, Phys. Rev. Lett. **103** (2009), 148101.

36. J. E. Stephen and R. H. Jonathan, *In pursuit of propulsion at the nanoscale*, Soft Matter **6** (2010), 726-738.

37. P. Swartztrauber, R. Sweet and J. Adams, *FISHPACK: efficient FORTRAN subprograms for the solution of separable elliptic partial differential equations*, 1999.

38. M. Tome and S. McKee, *GENSMAC: a computational marker and cell method for free surface flows in general domains*, J. Comput. Phys. **110** (1994), 171-186.

39. P. T. Underhill, J. P. Hernndez-Ortiz and M. D. Graham, *Divergent diffusivity and long-range correlations in suspensions of swimming particles* Phys. Rev. Lett. **100** (2008), 248101.

40. R. Voituriez, J. F. Joanny and J. Prost, *Spontaneous flow transition in active polar gels*, Europhys. Lett. **70** (2005), 404.

41. P. Wesseling, *Principles of Computational Fluid Dynamics*, Springer, 2001.

42. C. W. Wolgemuth, *Collective swimming and the dynamics of bacterial turbulence*, Biophys. J. **95** (2008), 15641574.

43. X. Zheng, M. G. Forest, R. Zhou and Q. Wang, *Likelihood and expected-time statistics of monodomain attractors in sheared discotic and rod-like nematic polymers*, Rheol. Acta **44** (2005), 219-234.

VITA

Panon Phuworawong
Department of Computational and Applied Mathematics
Old Dominion University
Norfolk, VA 23529

PREVIOUS DEGREES:
B.S. Computer Engineering, February 2006, Kasetsart University.
M.S. Finance, May 2008, Thammasat University.

SCHOLARSHIPS:
The Graduate Teaching Assistantship, Old Dominion University, USA, 2010-2011.
The National Science Foundation support (DMS-0908409), Old Dominion University, USA, 2012-2013.

Typeset using LaTeX.